ESTIMATION OF THE SURFACE CHARGE DISTRIBUTION OF SOLIDS IN LIQUIDS BY USING ATOMIC FORCE MICROSCOPY

A Thesis Submitted to
the Graduate School of Engineering and Sciences of
İzmir Institute of Technology
in Partial Fulfillment of the Requirements for the Degree of

DOCTOR OF PHILOSOPHY

in Chemical Engineering

by
Gülnihal YELKEN ÖZEK

March 2011
İZMİR

We approve the thesis of **Gülnihal YELKEN ÖZEK**

Prof. Dr. Mehmet POLAT
Supervisor

Prof. Dr. Devrim BALKÖSE
Committee Member

Prof. Dr. Mustafa DEMİRCİOĞLU
Committee Member

Assoc. Prof. Dr. Salih OKUR
Committee Member

Assoc. Prof. Dr. Fehime ÖZKAN
Committee Member

03.03.2011

Prof. Dr. Mehmet POLAT
Head of the Chemical Engineering
Department

Prof. Dr. Durmuş Ali Demir
Dean of the Graduate School of
Engineering and Sciences

ACKNOWLEDGMENTS

I would like to express my sincere gratitude to my Ph.D. advisor Prof. Mehmet Polat for his guidance and encouragement. I have benefited greatly from his direction and review of this study. My understanding of surface chemistry is, in no small measure, a result of Prof Polat ability to teach, guide, and challenge his students to become scientists. I was lucky to have the opportunity to learn from Prof Polat.

My appreciation is also given to Prof. Devrim Balköse for her providing me with valuable insight, comments, and suggestions. She was always motivated and encouraged me in my PhD. She was always accessible and willing to help to me and also other students.

I would like to appreciate Prof. Mustafa Demircioğlu for his guidance, his help during all my educational life. In addition, he was always accessible and willing to help his student with their education. Also I would like to thank his valuable advice in discussion and furthermore using his precious times to read this thesis and gave his critical comments about it.

I would like to thank my thesis jury member Assoc. Prof. Salih Okur for his valuable comment during my research. I would like thank Assoc. Prof. Fehime Özkan for her comment and advises. It is a pleasure to thank Prof Hurriyet Polat for her kindness and her advices. I also would like to thank Prof. Muhsin Çiftçioğlu, his advise for powder preparation and he gave me some Alumina powders (Sumitoma and Alcoa), which I used during my experiments.

I would like to thank Assoc. Prof. Cihangir Duran, Gebze Institute of Technology; he gave me a chance to accomplish Zeta Potential Measurements of this thesis. And I also thank Adem Şen for technical support during Zeta Potential Measurements.

I would like to thank Mine Bahçeci for AFM measurements and her friendship during the past few years. I would like to thank Yekta Günay Oğuz, Dane Ruscuklu and Mert Sudağıdan for helping me in my Potentiometric Titration experiment in Biotechnology Center in İYTE. I also would like to thank IYTE-Material Research Center members, Duygu Oğuz Kılıç, Gökhan Erdoğan and Evrim Yakut.

I would like to thank Chemical Engineering Department specialists; they helped me and did my FTIR, BET, Paticle size experiements; Dr. Özlem Duvarcı, Dr. Filiz

Ömürlü, Nesrin Tatlıdil, Nesrin Gafaroğlu, Burcu Alp, Deniz Şimşek and Didem Berkün.

I would like to express my gratitude to several friends, especially Sevdiye Atakul, Filiz Ömürlü, Yelda Akdeniz, Özlem Duvarcı, Berna Üzelyalçın and Bahar Başak Pekşen.

I am very grateful to my mother, who was a Preliminary School teacher and my father M. Zeki Yelken who was also linguistic Prof. in University, they always supported me my carrier at University. I would like to thank my brother, Göksel Yelken for his love and support. I would like to thank my husband, Anıl Özek for his support and patience. I also want to thank my aunt Gülseren Eyice, every time she supports my mother to taking care of my son, she is also second grandmother of my son.

I would like to specially thank my son Bertuğ for his patience and unconditional love, and I would like to apologies to him for the time which we didn't share, during my PhD work.

Especially I would like to thank my mother Nurten Yelken for her unconditional love, support, and encouragement and taking care of my son that have enabled me to successfully complete my PhD studies.

ABSTRACT

ESTIMATION OF THE SURFACE CHARGE DISTRIBUTION OF SOLIDS IN LIQUIDS BY USING ATOMIC FORCE MICROSCOPY

Colloidal systems are widely encountered in minerals, ceramics, environment, biology, pharmaceuticals and cosmetics industries. These systems consist of micron-sized particulates dispersed in a solvent. Homogeneity, dispersibility, stability of colloidal systems determines the economy and success of the final product in these applications. Control and manipulation of these properties depend on detailed analysis of the interactions among the particles. Electrophoretic potential measurements or colloidal titration methods are widely employed to characterize the charging of colloidal systems. However these methods only yield average charging information, not the charge distribution on the surface.

Atomic Force Microscope (AFM) allows topographic surface analysis at nanometer level resolutions. Though it is widely used to obtain derived information AFM directly measures the forces between the tip and the surface atoms. The objective of the present work is to assess the applicability of AFM to surface charge mapping, i.e., the detection of positive or negative charged regions on metal oxide surfaces. Hence, well defined tips were prepared and allowed to interact with well defined oxide surfaces under different pH conditions. The influence of solution ion concentration and pH on the forces measured was also investigated.

These measured force-distance curves were analyzed using a new solution of the one dimensional Poisson-Boltzmann equation to isolate the electrical double layer force, hence the surface charge on each measurement point. The new solution in question provides analytical expressions for all charging conditions which are amenable to such analysis.Repetitive force measurements on a predefined grid on the solid surface ultimately yield the charge distribution of the surface. Such an analysis procedure is new and advances the charge measurements on solids in solution to a new level.

ÖZET

SIVI İÇİNDE KATILARIN YÜZEY YÜK DAĞILIMININ ATOMİK KUVVET MİKROSKOPU KULLANILARAK BELİRLENMESİ

Mineral, seramik, çevre, biyoloji, boya, ilaç, kozmetik vb. endüstrilerde bir sıvı içinde dağılmış mikron boyutlarındaki tanelerden oluşan kolloidal sistemlerin homojenitesi, dağıtılabilirliği (*dispersibility*), kararlılığı (*stability*), reolojisi, akıcılığı ve şekillendirilebilirliği (*plasticity/forming*) bu endüstrilerdeki uygulamaların başarısını belirler. Bu özelliklerin kontrolü, sistemi oluşturan tanelerin karşılıklı etkileşimlerinin kontrol edilebilmesine bağlıdır. Yüzey yüklenmesinin karakterizasyonu için kullanılan elektroforetik potansiyel veya koloidal titrasyon ölçümlerinde ise yüzey yük dağılımı değil, tüm sistemin ortalama yük değeri ölçülebilir.

Atomik Kuvvet Mikroskobu (AFM) nanometre seviyelerinde topografik yüzey analizi yapmak için kullanılır. Yaygın olarak yüzey topoğrafyasının belirlenmesinde kullanılmasına rağmen, AFM yüzey ile kantileverin ucu arasındaki atomik kuvvetleri doğrudan ölçmekte kullanılabilir.

Bu çalışmanın amacı, atomik kuvvet mikroskobunun yüzey yük haritasının çıkarılmasında kullanılabilirliğini açıklamaktır. Alümina, silika ve cam gibi iyi tanımlanmış metal oksit yüzeyleri ile değişik uçlar arasında, farklı çözelti koşullarında, yüzeyin bir çok noktasında bir matriks çerçevesinde AFM kuvvet ölçümleri yapılacaktır. Oksit sistemlerinde, yüzey yüklerinin pH değiştirilerek saptanması sağlanmıştır. Uç ve yüzey arasındaki kuvvetlere, iyon konsantrasyonu ve pH etkisi de incelenmiştir.

Ölçülen Kuvvet-Uzaklık eğrilerinin hesaplanması Poisson-Boltzman denkliğinin yeni geliştirilen analitik çözümü ile hesaplanmıştır. Elde edilen ölçümlerden kuvvetlerin bileşenlerine ayrıştırılması sonucunda, elektriksel çift tabaka kuvvetleri izole edilecektir. Uygun elektriksel çift tabaka teorilerinin kullanılması vasıtasıyla da, elektriksel kuvvet bileşeninden yüzeyin yük dağılımı elde edilecektir. AFM ile ölçülen ve teorik olarak hesaplanan kuvvet-uzaklık eğrileri karşılaştırılmıştır.

Katı yüzey üzerinde tanımlanan kılavuz çizgiler üzerinde yinelenen kuvvet-uzaklık eğrileri, yüzeyin yük dağılımını belirler. Bu analiz prosedürü yenidir ve katı yüzeylerin sıvı içinde yüzey yük dağılımlarının ölçülmesini yeni bir seviyeye taşımaktadır.

I dedicate to my mother Nurten Yelken
and my son Bertuğ Özek

TABLE OF CONTENTS

APPENDICES

LIST OF FIGURES

LIST OF TABLES

LIST OF SYMBOLS

A_{ij}	Hamaker constant for particles i and j
b	Width of the cantilever (m)
c	Speed of light (2.997925×10^{8} m/sec)
c	Contact point in force measurement (m)
C_0	Electrolyte concentration of the solution
D	Vertical piezo movement in force measurement (m)
e	Electronic charge (1.602189×10^{-19} C)
F	Faraday constant (9.64845×10^{4} C/mole)
f_x	Force per unit area
F_{AFM}	Interaction force between a colloidal probe and a flat plate in force measurement ($F_{AFM}=k_n x$; N)
f_e	Electrostatic pressure between plates (N/m^2)
F_e	Dimensionless electrostatic pressure between plates; $F_e=f_e/2RTC_0$.
F_{DLVO}	Net interaction pressure between two flat plates (N/m^2)
Fel	Electrostatic (Maxwell) component of the force acting on the plates (N/m^2)
F_{os}	Osmotic pressure force
F_{vdw}	Van der Waals interaction pressure between two flat plates (N/m^2)
h	Planck’s constant (6.626176×10^{-34} J.sec)
h	Gap length between two surfaces (m)
h	Probe-to-surface separation in force measurement ($h=(D-c)-x$; m)
H	Dimensionless distance between plates; $H=\kappa h$
I	Molar electrolye concentartion (M]
k	Boltzmann constant (1.380662×10^{-23} J/K)
k_n	Spring constant for the cantilever (N/m)
L	Length of the cantilever (m)
M_i	Molecular weight of component i (kg/mole)
m_e	Rest mass of electron (9.10939×10^{-31} kg)
n_i	Refractive index of material i
N_A	Avogadro’s number (1/mol)

Q_f	Quality factor the cantilever oscillations
P_{os}	Osmotic pressure
p	Overall pressure between plates (N/m^2)
P	Overall dimensionless electrostatic pressure between plates; $P=p/2RTC_0$.
R	Particle radius (m)
r	Radial coordinate
R	The gas constant (8.31441 J/mol.K)
Re	Reynolds number
S_1	Dimensionless surface charge density on Plate 1 at separation H; $S_1^2=\sigma_1^2/2\varepsilon\varepsilon_0RTC_0$
S_2	Dimensionless surface charge density on Plate 2 at separation H; $S_2^2=\sigma_2^2/2\varepsilon\varepsilon_0RTC_0$
$S_{1\infty}$	Dimensionless surface charge density on Plate 1 at infinite separation; $S_{1\infty}^2=2\cosh Y_{1\infty}-2$
$S_{2\infty}$	Dimensionless surface charge density on Plate 2 at infinite separation; S2∞2=2coshY2∞ -2
T	Absolute temperature (K)
U(D)	Energy between two boddies of arbitrary shape at distance (D)
U_{DLVO}	Energy per unit area between two planar surface
x	Distance into the solution from Plate 1 located at x=0 (m)
x	Distance between molecules
x	Distance from the surface in the double layer (m)
x	Net cantilever deflection in force measurement ($x=(X-X0)/\chi$; m)
X	Output signal by the photomultiplier for the overall bending of the cantilever in force measurement (mV)
X_0	Output signal by the photomultiplier when two surfaces are not interacting (mV)
X	Dimensionless distance into solution from Plate 1 located at X=0; $X=\kappa x$
$X_{1,2}$	Dimensionless locations X_1 and X_2 in the diffuse layer with potential Y
X_m	The distance of the point where the $Y=Y_m$ from Plate 1

X'_m	The distance of the point where the $Y=Y_m$ from Plate 2
Y	Dimensionless potential in solution at a point X between the plates
Y_1	Dimensionless surface potential on Plate 1 at separation H; $Y_1=zF\psi_1/RT$
Y_2	Dimensionless surface potential on Plate 2 at separation H; $Y_2=zF\psi_2/RT$
$Y_{1\infty}$	Dimensionless surface potential on Plate 1 at infinite separation; $Y_{1\infty}=zF\psi_{1\infty}/RT$
$Y_{2\infty}$	Dimensionless surface potential on Plate 2 at infinite separation; $Y_{2\infty}=zF\psi_{2\infty}/RT$
Y_m	Real or imaginary potential at point X_m where $dY/dX=0$
z	Valence of the electrolyte
$\alpha_{0,i}$	Static polarizability of molecule i ($1.61\text{x}10^{-40}$ C^2m^2/J for water)
$\alpha^*_{0,i}$	Static polarizability volume of molecule i ($1.45\text{x}10^{-30}$ m^3 for water; $\alpha^*_{0,i}=\alpha_{0,i}/4\pi\varepsilon_0$)
β_{ij}	van der Waals parameter for molecules i and j ($J.m^6$)
ε	Relative permittivity (78.5 for water)
ε_0	Permittivity of vacuum ($8.854\text{x}10^{-12}$ $C^2/J.m$)
Γ_i	The imaginary component of the hydrodynamic function
ϕ	Integration constant; varies with plate separation H
ϕ_K	Energy of Keesom (dipole-dipole) interaction between molecules (J)
ϕ_D	Energy of Debye (dipole-induced dipole) interaction between molecules (J)
ϕ_L	Energy of London (induced dipole-induced dipole) interaction between molecules (J)
ϕ_{vdw}	Energy of van der Waals attraction between molecules (J)
κ	Reciprocal thickness of the double layer or Debye-Hückel parameter ($\kappa=\sqrt{2z^2F^2C_0/(\varepsilon\varepsilon_0RT)}$; m^{-1})
$\lambda(a,\phi)$	A function related to a specific length between plates
μ_i	Dipole moment of molecule i ($6.17\text{x}10^{-30}$ C.m for water)
μ_f	Viscosity of fluid in which cantilever vibrates (typically air; $1.79\text{x}10^{-5}$ kg/m.sec)

$\nu_{0,i}$	Frequency of the electron for molecule i (2.1x10^{15} Hz for water)
$\rho(x)$	Charge density in solution at a point x between the plates (C/m^3)
ρ_i	Density of material i (kg/m^3)
ρ_f	Density of fluid in which cantilever vibrates (typically air; 1.23 kg/m^3)
σ_1	Surface charge density on first plate at separation h (C/m^2).
σ_2	Surface charge density on second plate at separation h (C/m^2).
σ_{oi}	Surface charge density of plate i (C/m^2)
$\sigma_{oi,\infty}$	Surface charge density of plate i at infinite separation (C/m^2)
ω_f	Cantilever’s fundamental resonance frequency (hertz)
$\psi(x)$	The value of potential in the double layer at point x between two flat plates (volts)
$\psi(x)$	Potential in solution at a point X between the plates (volts)
ψ_{0i}	Surface potential of plate i (volts)
$\psi_{0i,\infty}$	Surface potential of plate i at infinite separation (volts)
ψ_1	Surface potential on Plate 1 at separation h (volts)
ψ_2	Surface potential on Plate 2 at separation h (volts)
$\psi_{1\infty}$	Surface potential on Plate 1 at infinite separation (volts)
$\psi_{2\infty}$	Surface potential on Plate 2 at infinite separation (volts)

CHAPTER 1

INTRODUCTION

Long-range interactions between colloidal surfaces are important in various physico-chemical systems in mineral processing, powder technology, ceramics, soils, friction and lubrication, paint industry, environmental sciences, biomedical applications and many others. The relative interplay of the surfaces with each other or with the variety of dissolved / dispersed species in the system are determined by these forces. Such interactions decide the outcome of such unit operations as adsorption, flotation, dispersion, coagulation/flocculation, filtering, forming, etc. Therefore, determining the actual magnitudes of the force of interaction in mineral systems is of utmost importance in understanding such unit processes for design and control purposes.

A theoretical tool for predicting the forces acting in colloidal systems are the well-known DLVO theory (Derjaguin and Landau, 1941); (Verwey and Overbeek, 1948). This theory basically states that the net energy of interaction is a sum of van der Waals and electrical double layer forces. Depending on the presence of surface active species, acid/base equilibrium and hydrophobicity of the particles, secondary interactions such as steric, hydration and hydrophobic can also develop, but these are also derivatives of these two forces. The van der Waals component is mainly determined by the bulk of the interacting bodies and the separating medium and is not so much affected by the chemistry of the solution. However, the electrostatic interaction which owes its presence to the electrical double layer which spontaneously develops when a solid particle is placed in solution due to different chemical activities of ions in solution and in bulk is a strong function of the solution chemistry. This force is usually the manipulated component to reach desired rheology or stability in a given system. In the case of metal oxide-water systems, protons are the main species which adsorb to or desorb from the surface and alter the charging characteristics and the magnitude of the electrostatic interaction force. This makes the pH the main parameter determining the charging behavior of the metal oxide systems. For other solid chemistries different ions may play specific roles based on the surface structure and the solvation behavior of the particles.

The DLVO theory has been tested with positive results to represent the actual behavior in colloidal systems well over the years. Nevertheless, its direct comparison using actual inter-particle forces measurements has been possible relatively recently following the introduction of the Surface Force Apparatus (SFA) (Tabor and Winterton, 1969; Israealachvili and Tabor, 1972; Isrealachvili, 1987; Horn et al., 1987; Horn et al., 1988). Since SFA relies on observation of the interference fringes to determine the vertical distance between two cylinders of desired material, it can only be used with transparent substrates such as mica, glass or quartz. Also, SFA lacks the capability to provide lateral information about the surface has a high vertical resolution (Arai and Fujihira, 1994).

Just as SFA the Atomic Force Microscope, AFM, can also be be used to measure the interaction force between various surfaces just as SFA. AFM is not hampered by the limitations of the SFA and has been increasingly used for measuring the long-range interaction forces in a variety of colloidal systems. Such force measurements, however, had to be coupled to an in-depth knowledge of the relevant theories in order to make quantitative sense. Recent research has shown that the theory agrees well with experimental force measurements done by AFM rather nicely.

Atomic Force Microscope (AFM) allows topographic surface analysis at nanometer level resolutions. In this microscope, a sharp tip placed on the free end of a very tiny and flexible cantilever is scanned over the surface to be studied. Atomic interactions which develop between the tip and the surface, cause bending of the cantilever. The magnitude of the bending can be accurately determined by a laser light reflected over the cantilever. Since the bending amount is a strong function of the tip-surface distance it can be converted to high resolution topographical information.

In this study, we take the AFM force measurements a step further and propose to map the surface charge distribution of oxide surface by careful AFM force measurements carried out with well defined tips. The approach will employ the DLVO theory under the conditions it is applicable to isolate and determine the magnitude of the electrostatic component of the interparticle force measured. The proposed method will attempt to determine the surface charge at that point on the surface from the electrostatic component with the final surface charge map of the surface being probed. Then a surface charge distribution can be obtained by repeating the force measurement on a predetermined grid on the surface. The surface charge distribution so obtained will be tested against more traditional charge measurement methods which provide an average (or potential) value for the complete surface.

CHAPTER 2

INTERPARTICLE INTERACTIONS

2.1. Theory of Particle-Particle Interactions in Colloidal Systems

A quantitative knowledge of long-range interactions between colloidal surfaces important for understanding the phenomena underlying numerous physico-chemical systems in such diverse areas as mineral processing, powder technology, ceramics, environmental sciences, soils friction and lubrication and adhesives. Several models which quantitatively predict particle-surface interaction energies (or forces) exist, the most successful one being the Derjaguin-Landau-Verwey-Overbeek (DLVO) theory. The DLVO theory for colloid surface forces accounts for the long-range electrostatic interactions that arise from the existence of overlapping diffuse double layers of counter ions near charged surfaces in solution and van der Waals forces caused by the specific alignment and coupling interactions of molecular dipoles. While useful in many situations where surfaces may be assumed uniform and relatively ideal, the DLVO theory does not account for several types of interaction forces thought to be relevant to particle attachment, including hydrophobic, hydration, and steric (electrosteric) forces. Therefore it is important that the theory be used with proper understanding and for those conditions under which it is applicable.

2.1.1. van der Waals Interactions

The van der Waals attraction is the cause of such macroscopic phenomena as condensation, wetting, coagulation, etc and originates from permanent, instantaneous and induced dipoles created by atoms and molecules. Hence the electromagnetic force is the source of the van der Waals forces. Forces between macroscopic objects result from a complex interplay of the interaction between molecules in the two objects and the medium separating them. When the two dipoles are allowed to rotate freely, they interact and a balance is established between preferential orientation of the dipoles and the thermal motion which acts to disturbed this balance (Myers, 1999). This thermally averaged dipole–dipole free energy (ϕ_K) is often referred to as the Keesom energy:

$$\phi_K = -\frac{\mu_1^2 \mu_2^2}{3\,kT\,(4\pi\varepsilon_0)^2 D^6} \tag{2.1}$$

where μ_1 and μ_2 are dipole moments, D is the distance between particles. Also, when a charge approaches a molecule without a static dipole moment, an attractive force arises from a charge shift in the nonpolar molecule induced by the charge. In analogy, a molecule with a static dipole moment will interact with a polarizable molecule by inducing a dipole moment in the polarizable molecule. If the dipoles can freely rotate, the energy of interaction between a permanent dipole and an induced dipole has been shown to be given as;

$$\phi_D = -\frac{(\alpha_2 \mu_1^2 + \alpha_1 \mu_2^2)}{(4\pi\varepsilon_0)^2 D^6} \tag{2.2}$$

This interaction is called the Debye interaction. It will also arise between two identical polarizable molecules that have a permanent dipole moment. Both the Keesom and Debye interactions which have their rolls in classical physics fail to explain the attraction between two nonpolar molecules. Such an attraction is evidently exists because non-polar gases also condense at low enough temperatures. Responsible for this attraction is the so-called London or dispersion force. To calculate the dispersion force, quantum mechanical perturbation theory is required. An impression about the origin of dispersion forces can be obtained by considering an atom with its positively charged nucleus around which electrons circulate with a typically high frequency of 1015–1016 Hz. At every instant, the atom is therefore polar, the direction of the polarity changing periodically with this high frequency. When two such oscillators approach, they start to influence each other, attractive orientations having a higher probability than the repulsive ones, leading to an attractive force on the average. The free energy between two molecules with ionization energies $h\upsilon_1$and $h\upsilon_2$ was approximated by London as;

$$\phi_L = -\frac{3h v_1 v_2 \alpha_1^* \alpha_2^*}{2(v_1 + v_2)(4\pi\varepsilon_0)^2 D^6} \tag{2.3}$$

Where

$$\alpha_i^* = \frac{3M_i}{4\pi\rho_i N_A}\frac{(n^2-1)}{(n^2+2)} \; ; \; \alpha_i^* = \frac{\alpha_i}{4\pi\varepsilon_0} \tag{2.4}$$

and

$$v_i = \frac{1}{2\pi}\sqrt{\frac{e^2}{\alpha_i m_e}} \tag{2.5}$$

The van der Waals force is the sum of Keesom, Debye and London dispersion interactions such that (Hunter, 2001):

$$\phi_{vdW} = -\beta_{12} D^{-6} \tag{2.6}$$

The term β_{12} is called the vdW parameter and is equal to:

$$\beta_{12} = -\frac{2}{3}\frac{\mu_1^2\mu_2^2}{kT(4\pi\varepsilon_0)^2} - \frac{\alpha_2\mu_1^2 + \alpha_1\mu_2^2}{(4\pi\varepsilon_0)^2} - \frac{3}{2}h(\frac{v_1 v_2}{v_1+v_2})\frac{\alpha_1\alpha_2}{(4\pi\varepsilon_0)^2} \tag{2.7}$$

It can be seen that contribution of ϕ_K, ϕ_D and ϕ_L interactions to ϕ_{vdW} would be different for different substances. For polar molecules such as water the Keesom interaction is dominant whereas for apolar hydrocarbons the overall interaction energy is almost completely made up of the London contribution. This is the reason why water is an excellent solvent while aliphatic compounds have no solvation power over ionic compounds (Butt and Kappl, 2010).

In calculating the van der Waals interaction between two colloidal particles, a pairwise addition of the individual interactions (Equation 2.6) between every molecule of each body is carried out by volume integration. This approach is called Microscopic or Hamaker Method who first carried out the integration (Polat and Polat, 2000-a).

The van der Waals interaction pressure (force per unit area) for two interacting plates is given as:

$$F_{vdW}(h) = \frac{A_{12}}{6\pi h^3} \tag{2.8}$$

The Hamaker' constant A_{12} comes out as

$$A_{12} = \pi^2 (\frac{\rho_1 N_A}{M_2})(\frac{\rho_2 N_A}{M_2})\beta_{12} \tag{2.9}$$

from the integration process, but in practice it must be determined experimentally. Methods used in determining the Hamaker's constant and a compilation for a large list of materials interacting in vacuum or in other solvents is also presented in, (Bergström, 1997) and (Polat and Polat, 2000-a).

Hamaker constants were calculated for all the symmetric systems two surfaces of material 1 interacting across a medium 3, using full Lifshitz calculations, across vacuum and water. Hamaker constants were also estimated using two different approximations, for the Hamaker constant in vacuum (Tabor-Winterton equation including the static contribution (TWS)), and together with the static term (Horn-Israelachvili (HIS) equation) for the Hamaker constant across water. The calculated values are collected in Appendix A. The Hamaker constants in vacuum, A_{1v1}, vary between 2.96 10^{-19} J for diamond down to 40.5 10^{-21} J for NaF. Most of the halides have relatively low Hamaker constants while the more covalently bonded oxides, carbides and nitrides have significantly higher values. The TWS approximation gave a surprisingly good correspondence to the full Lifshitz calculations. The main difference between the TWS approximation and the full Lifshitz calculation is that the TWS approximation only considers the contribution from the UV-Vis region, hence ignoring the IR contribution. The good agreement between the full Lifshitz and the TWS approximation supports the previous statement that the IR contribution to the Hamaker constant is negligible for most ceramic materials in vacuum or air (Bergström, 1997).

It is clear from Table A.1 (in Appendix A) that the Hamaker constants, hence the magnitude of the vdW interaction energy, changes significantly depending on whether the gap separating the macroscopic bodies is simply vacuum or contain another phase such as water. Therefore, an effective Hamaker constant A_{132} must be utilized for the bodies 1 and 2 separated by a gap containing medium 3. The most commonly used method to determine A_{132} is to assume that two particles interact through a pseudo-chemical reaction where the two particle-medium pairs (1-3 and 2-3) produces one particle-particle (1-2) and one medium-medium (3-3) pairs (Polat and Polat, 2000-a).

The change in the potential energy for such a process is:

$$\Delta\phi = \phi_{12} + \phi_{33} - \phi_{13} - \phi_{23} \tag{2.10}$$

Since the energy of interaction between two colloidal particles is a direct function of the Hamaker constant for a given distance, the change in the potential energy can be written in terms of the Hamaker constants such that

$$A_{132} = A_{12} + A_{33} - A_{13} - A_{23} \tag{2.11}$$

The value A_{132} is called the effective Hamaker constant. The interaction between two materials i and j can be given by the geometric mean of the interaction between i-i and j-j pairs to a good approximation as:

$$A_{ij} = \sqrt{A_{ii}A_{ij}} \tag{2.12}$$

its shown that this relationship holds within 95% accuracy. Then, combining equations 2.11 and 2.12 gives

$$A_{132} = \left(\sqrt{A_{22}} - \sqrt{A_{33}}\right)\left(\sqrt{A_{11}} - \sqrt{A_{33}}\right) \tag{2.13}$$

In addition, the van der Waals interaction has to be corrected for the magnitude of the separating gap. If the size of the gap is larger than, say 100 nm, the time it takes for the electromagnetic signal to travel from one surface to another is long enough that the position of the charges on the second body has shifted, hence, decreasing the magnitude of the interaction. The correction for what is called this “retardation effect” has been presented in Polat and Polat (2000-a). However, the retardation effect is negligible distances less than 20 nm and will be ignored here.

2.1.2. Electrical Double Layer Interactions

Presence of charged sites on the solid's surface attracts the oppositely charged ions in the solution and leads to development of an electrical double layer at the solid-water interface; the charged surface on the solid side and a diffuse layer containing the counteracting ions on the solution side. This creates a potential gradient between the surface and every point in solution. For solid surfaces immersed in aqueous systems, double layers tend to form spontaneously. Insight into the properties of double layers is mandatory, in describing for instance electrosorption, ion exchange, electrokinetics, charged monolayers, colloid stability, polyelectrolytes and proteins, and micelle formation of ionic surfactants.

The potential difference between the solid side and the solution side is equal to the surface potential ψ_0 at the solid's surface and exponentially diminishes to zero in the diffuse layer according to a function ψ(x) (Figure 2.1). The relationship which gives how the potential profile ψ(x) changes in the diffuse layer as a function of distance x from the solids's surface is called Poisson-Boltzmann equation. The so called one dimensional Poisson-Boltzman equation can be readily derived by combining the Poisson Equation which describes the relationship between the charge distribution inspace as a function of the electric potential as a function of distance;

$$\rho(x) = -\varepsilon\varepsilon_0 \frac{d^2\varphi}{dx^2} \tag{2.14}$$

and the Boltzmann distribution of the ions with in the double layer

$$\rho(x) = \sum_i z_i F C_{oi} e^{-\frac{z_i F \varphi(x)}{RT}} \tag{2.15}$$

such that the outcome is in the form:

$$\frac{d^2\psi(x)}{dx^2} = \frac{\kappa^2 RT}{zF} \sinh\left[\frac{zF\psi(x)}{RT}\right] \tag{2.16}$$

for a 1:1 symmetrical electrolyte.

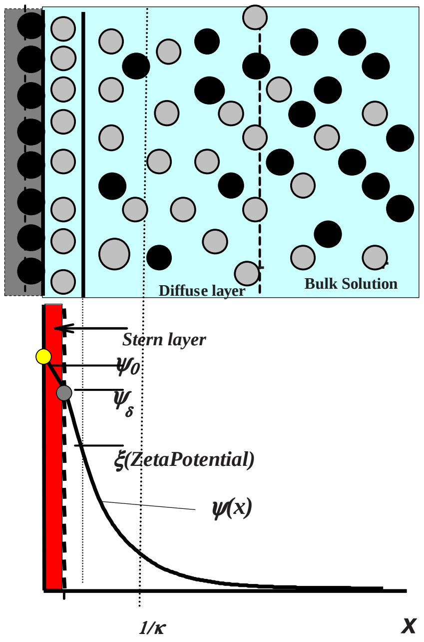

Figure 2.1. Schematic illustration of the Stern model of the electrical double layer which accounts for counterion size at the surface of a particle (●positive charges, ○ negative charges).

The equation can be normalized using dimensionless quantities $Y = zF\psi(x)/RT$ and $X = \kappa x$ such that:

$$\frac{d^2Y}{dX^2} = \sinh Y \tag{2.17}$$

where κ is given by the equality:

$$\kappa = \frac{2z^2F^2C_0}{\varepsilon\varepsilon_0 RT} \tag{2.18}$$

The slope of the potential profile at each point is equal to the charge density at that point such that $d\psi(x)/dx = \sigma(x)$. By the same token, the surface charge density (surface charge per unit area of the surface) is equal to the slope of the potential profile at the vicinity of the surfaces such that $d\psi(x)/dx\big|_{x=0} = \sigma_0$. A detailed review of the mathematical derivation of the potential profile $\psi(x)$ and how it changes under different conditions are presented in a review by Polat (1999).

In the case of two surfaces infinitely apart in solution, they will have surface potentials $\psi_{1,\infty}$ and $\psi_{2,\infty}$ each with its potential profile $\psi_i(x)$ extending into solution uninterrupted (Figure 2.2-a). This effectively means that the two surfaces do not feel the presence of each other. In practice, surface potentials at infinite separation ($\psi_{i,\infty}$) are estimated from electrophoretic measurements whereas surface charge densities ($\sigma_{i,\infty}$) can be measured using potentiometric titration methods. These two quantities are also related to each other through equality:

$$\sigma_{i,\infty}^2 = 4\varepsilon\varepsilon_0 RTC_0[\cosh(\frac{zF\psi_{i,\infty}}{RT}) - 1] \tag{2.19}$$

However, as the two surfaces come closer, the potential profiles begin to interact, yielding a composite potential profile $\psi(x)$ between the two surfaces (Figure 2.2-b). For two interacting surfaces located at x=0 and x=h, it is apparent that

$\left.\frac{d\varphi}{dx}\right|_{x=h} = \sigma_1$ and $\left.\frac{d\varphi}{dx}\right|_{x=h} = \sigma_2$. At a given separation h, surface potentials ψ_1 and ψ_2 and surface charge densities σ_1 and σ_2 are related by the relationship:

$$\frac{\sigma_1{}^2}{2\varepsilon\varepsilon_0 RTC_0} - 2\cosh(\frac{zF\psi_1}{RT}) = \frac{\sigma_2{}^2}{2\varepsilon\varepsilon_0 RTC_0} - 2\cosh(\frac{zF\psi_2}{RT}) \tag{2.20}$$

or in the terms of dimensionless quantities

$$S_1^2 - 2\mathrm{Cosh}Y_1 = S_2^2 - 2\cosh Y_2 \tag{2.21}$$

Though this equation holds for all separations, the values of S_1, S_2, Y_1 and Y_2 will be different at each h. Then the plates are at infinite separation (no interaction) the correlation between surface charges and surface potential is in the forms:

$$S_{1\infty}^2 = 2\cosh Y_{1\infty} - 2 \quad \text{and} \quad S_{2\infty}^2 = 2\cosh\ Y_{1\infty} - 2 \tag{2.22}$$

Knowing the value of S_1, S_2, Y_1 and Y_2 at a given h, that is pairing the surface charge densities and the surface potential to the separation between plates, is one of the most important aspects of colloidal chemistry.

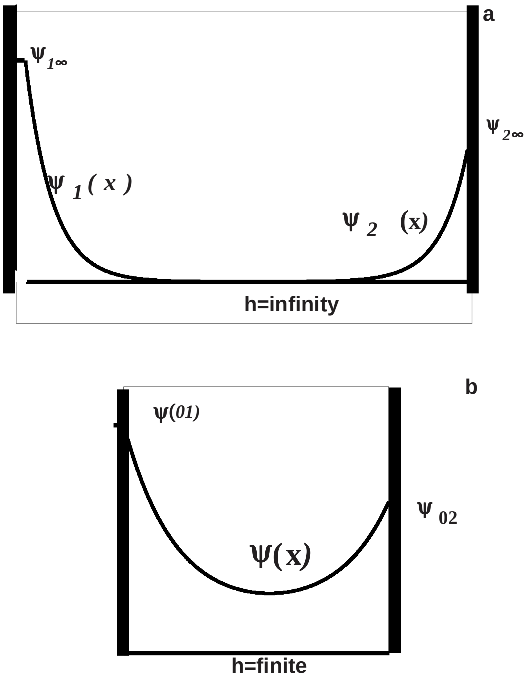

Figure 2.2. Potential profiles developed between two surfaces when they are infinitely apart (a) and interacting through a small gap h (b).

As the surfaces approach progressively, they tend to retain either constant surface potentials or constant surface charge densities depending on their charging mechanism. For those surfaces where charge equilibrium with solution is established very quickly compared to the speed of the approach, the surface charge density can adjust quite freely with changing h. For such surfaces the surface potential remains effectively constant during approach. These surfaces are called constant-potential surfaces. However, if the charges on the surfaces are relatively stationary, the surface charge densities remain constant during the approach of the surfaces. These surfaces are called constant-charge surfaces. In this case the surface potentials must vary according to Equation 2.20 to accommodate the increasing charge density in smaller volume of solution between the surfaces. The real surfaces usually may experience both effects. For such surfaces usually another equation elating surface charge and potential is required (charge related surfaces). However constant potential and constant charge surface cases essentially define the two boundaries for possible charging conditions.

In summary, the shape of the potential profile ψ(x) between the two surfaces determines the magnitude of the electrostatic interaction. Therefore, solution of the Poisson-Boltzmann (PB) equation to determine the potential profile ψ(x) at a given h is required to calculate the magnitude of the electrostatic interaction. However, analytical solution of PB equation for two interacting surfaces has been only possible for linearized cases such as surfaces with low potentials (< 25 mV). Calculations of the potential profile and the electrostatic interaction force between two surfaces with low potentials have been reviewed in a paper by Polat and Polat (2000-b).

For such special cases, the solution of the Poisson-Boltzmann equation between two interacting plates with surface potential ψ_1 and ψ_2 gives an expression for the potential profile as:

$$\psi(x) = \psi_1 \cosh(\kappa x) + \left[\frac{\psi_2 - \psi_1 \cosh(\kappa h)}{\sin(\kappa h)}\right] \sinh(\kappa x) \tag{2.23}$$

In terms of dimensionless quantities it becomes:

$$\mathrm{Y(x)} = \mathrm{Y}_1 \cosh X \left[\frac{Y_2 - Y_1}{\sin H}\right] \sinh X \tag{2.24}$$

Though Equation 2.14 is easy to use, it leads to large errors for highly charged systems which are frequently observed in real cases. Under such conditions, numerical evaluation of the Poisson-Boltzmann Equation is required to calculate ψ(x) at each h. One such numerical solution method is the “shooting” procedure where one starts from a known surface potential on one surface and numerically solves the PB equation using different initial surface charges until the solution converges with the surface potential on the other surface. A good and workable example of a shooting procedure has been provided by Polat and Polat (2010) very recently.

Charging of the surfaces leads to a pressure force experienced by the interacting plates as they approach each other. The analysis of this force has been done by Werwey aNd Overbeek and was shown to be due to osmotic and electrostatic effects (1948). The osmotic pressure force acting on a volume element of liquid (per unit volume) along the x-axis can be given as:

$$F_{os} = -\frac{dp_{os}}{dx} \tag{2.25}$$

If the volume element is within a potential field, it will also experience an electrostatic force called the Maxwell stress. The x-component of this force is equal to:

$$F_{el} = -\rho(x)(\frac{d\psi}{dx}) \tag{2.26}$$

At equilibrium, overall force balance on the volume element along the x-direction will require that:

$$\frac{dp_{os}}{dx} + \rho(x)(\frac{d\psi}{dx}) = 0 \tag{2.27}$$

Substituting ρ(x) from Equation 2.27 gives:

$$dp_{os} - \varepsilon\varepsilon_0(\frac{d^2\psi(x)}{dx^2})(\frac{d\psi}{dx}) = 0 \tag{2.28}$$

Recognizing that $(\frac{d^2\psi}{dx^2})(\frac{d\psi}{dx}) = \frac{1}{2}\frac{1}{dx}(\frac{d\psi}{dx})^2$ yields:

$$\frac{dp_{os}}{dx} - \frac{\varepsilon\varepsilon_0}{2}\frac{1}{dx}\left(\frac{d\psi}{dx}\right)^2 = 0 \tag{2.29}$$

which gives

$$p_{os} - \frac{\varepsilon\varepsilon_0}{2}(\frac{d\psi}{dx})^2 = \text{constant} = \text{p} \tag{2.30}$$

It can be seen from Equation 2.30 that the difference between osmotic pressure and the Maxwell Stress is always equal to a constant pressure at a given separation of the plates.

The osmotic pressure component can be evaluated further by re-writing Equation 2.25 such that:

$$dp_{os} + \rho(x)d\psi = 0 \tag{2.31}$$

If ρ(x) is substituted using $f(x) = \sum z_i FC_o e^{-\frac{zF\varphi(x)}{RT}}$ for a z:z electrolyte, the resulting expression is in the form:

$$dp_{os} = -z_i FC_0 \,(e^{-\frac{zF\psi(x)}{RT}} - e^{\frac{zF\psi(x)}{RT}})d\psi \tag{2.32}$$

$$dp_{os} = 2z_i FC_0 \,\sinh(\frac{zF\psi(x)}{RT})d\psi \tag{2.33}$$

The excess osmotic pressure between the plates can be found by setting the osmotic pressure in the bulk liquid (where there are no electrostatic effects; ψ=0) to zero and integrating Equation 2.33 between a point in bulk and any point between the plates with pressure p_{os} and potential ψ(x):

$$p_{os} = 2RTC_0 \left[\cosh(\frac{zF\psi(x)}{RT}) - 1\right] \tag{2.34}$$

Combining Equations 2.30 and 2.34 gives:

$$p = 2RTC_0 \left[\cosh(\frac{zF\psi(x)}{RT}) - 1\right] - \frac{\varepsilon\varepsilon_0}{2}\left(\frac{d\psi(x)}{dx}\right)^2 \tag{2.35}$$

In terms of dimensionless quantities, it becomes:

$$P = \frac{p}{2RTC_0} = [\cosh\, Y - 1] - 0.5(\frac{dY}{dX})^2 \tag{2.36}$$

Equation 2.36 gives the net pressure force between the two plates as a function distance from each plate. Since the two pressures must balance each other, the net pressure between the two plates must always be equal to a constant value, P for a given plate separation H.

Since the pressure will be constant at any point within the liquid separating the plates (see Equation 2.30) its evaluation at one of the plates is sufficient. Doing so for Plate 2 and expressing in terms of dimensionless quantities gives the magnitude of the double layer pressure at a given separation of the plates:

$$P = [\cosh Y_2 - 1] - \frac{S_2^2}{2} \tag{2.37}$$

It should be noted that the pressure value obtained from Equation 2.37 is meaningful only if it is paired to the distance H between the two plates as related above.

For surface with low charging conditions, one can easily determine surface potentials Y_1 and Y_2 for a given h using Equation 2.24. Surface charge densities S_1 and S_2 can also be determined for h using the equality 2.21. Hence, Equation 2.37 can easily be solved for that h since Y_2 and S_2 are known for how charging conditions.

For highly charged surfaces, the surface potentials and surface charge densities obtained from numerically computed potential profiles should be inserted in Equation 2.37 for each h.

In obtaining the forces for constant-potential surfaces, the surface potentials at infinite separation ($\psi_{01,\infty}$ and $\psi_{02,\infty}$) are kept constant at all separations while the corresponding surface charge densities (σ_{01} and σ_{02}) are determined from the potential profiles obtained for each h. In the case of constant-charge surfaces, the surface charge densities at infinite separation ($\sigma_{01,\infty}$ and $\sigma_{02,\infty}$) are kept unvaried while the surface potentials ψ_{01} and ψ_{02} are calculated at each separation h. These values are used in Equation 2.37 to determine the electrostatic force as a function of separation h.

It can be seen that similar to both the potential profiles, the electrostatic force of interaction calculations also can give quite erroneous results for high potentials. On the other hand, it must be noted that use of numerical analysis is quite tedious due to strong non-linearity of the PB Equation.

Polat and Polat (2010) recently developed an analytical solution for interacting parallel plates which carry arbitrary potentials. These equations were shown to be perfectly valid for all surface charging conditions, low or high. According to this work, one can relate the gap between the interacting plates to the surface charges and surface potentials developing on both plates at that separation. The analytical expression is in the form:

$$H = X_m + X_m' \tag{2.38}$$

where

$$X_m = \int_0^1 \frac{S_1}{\sqrt{u(S_1^{\,2}u - \phi)^2 - 4u}}\,du = \lambda(S_1, \phi) \tag{2.39}$$

and

$$X_m' = \int_0^1 \frac{S_2}{\sqrt{u(S_2^{\,2}u - \phi)^2 - 4u}}\,du = \lambda(S_2, \phi) \tag{2.40}$$

such that $\phi = S_1^2 - 2\cosh(Y_1) = S_2^2 - 2\cosh(Y_2)$.

The analytical equation for the potential change in the diffuse layer with X at the calculated H is given by:

$$X_{1,2} = X_m \pm \lambda(\varphi, \phi) \tag{2.41}$$

where

$$\lambda(\varphi, \phi) = \int_0^1 \frac{\varphi}{\sqrt{u(\varphi^2 u - \phi)^2 - 4u}}\,du \tag{2.42}$$

such that

$$\varphi = \sqrt{2\cosh(Y) + \phi} \tag{2.43}$$

A comparison of the potential profiles between interacting two plates for several highly charged surface conditions are presented in Figure 2.3 using Equation 2.41 and numerical shooting procedure. It can be seen that Equation 2.41 gives identical results to those obtained from numerical analysis.

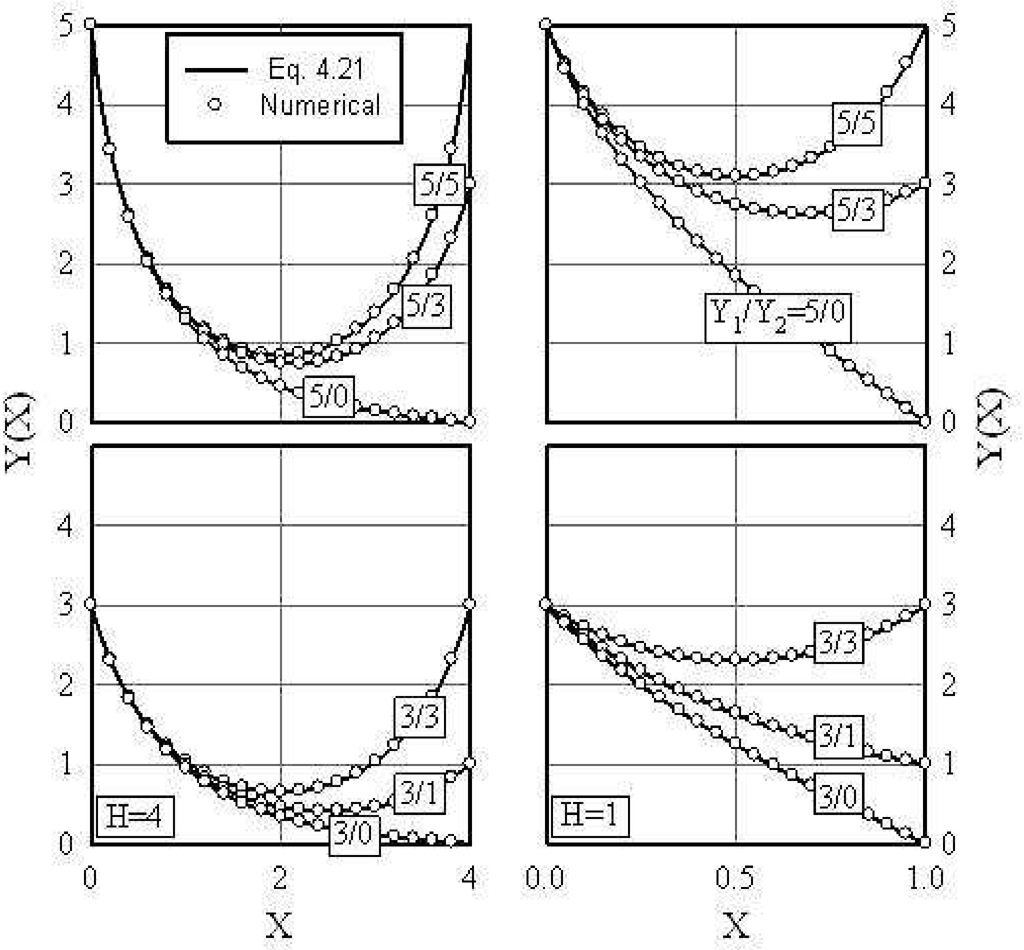

Figure 2.3. Potential profiles for H=4 and H=1 for surface potentials of Y_1 / Y_2 =5/5, 5/3, 5/0, 3/3, 3/1and 3/0. The lines are calculated from Equation 2.41 whereas the open circles are computed numerically using the Shooting Procedure for 20 points for each data set from (Polat and Polat, 2010).

The function $\lambda(\varphi,\phi)$ corresponds to some characteristic length between the interacting plates. It is a summation only for the parameter u within real limits $0 \leq u \leq 1$ and can be evaluated easily as a built-in function. All the commercial mathematical software in the market (such as MathCad, Matlab, Mathematica, etc.) or even general scientific calculators with numerical integration capability can handle the integral in Equation 2.42 easily. Since it represents physical distance, $\lambda(\varphi,\phi)$ should be treated as a real number, omitting the imaginary parts of any complex numbers which may arise due to the presence of square root term.

It should be emphasized that X_m and X'_m depend only on (S_1, Y_1) and (S_2, Y_2), respectively, since $\phi = S_1^2 - 2\cosh Y_1 = S_2^2 - 2\cosh Y_2$. Hence, Equation 2.38 is extremely important since it explicitly relates the surface potentials and surface charge densities on both plates to the plate separation H in an easily calculable way without any need for linearization or cumbersome computational procedures. As explained above, Y_1 and Y_2 will always be constant and equal to $Y_{1\infty}$ and $Y_{2\infty}$ for all H for constant-potentials surfaces. Expressing S_1 in terms of S_2 as $S_1^2 = S_2^2 - 2\cosh Y_{2_\infty} + 2\cosh Y_{1_\infty}$ leaves only S_2 and H as unknowns in Equation 2.38. Then, for any physically meaningful value of S_2, the equation will yield a corresponding H value. The S_2 values should be between the surface charge density at infinite separation and an arbitrary large negative surface charge density which would develop on Plate 2 at very close distances.

Similarly, for constant charge surfaces, the $S_{1\infty}$ and $S_{2\infty}$ values will remain constant for all H. The surface charge densities at infinite separation can be obtained from the surface potentials at that separation. Also, Y_1 can be expressed in terms of Y_2 such that $Y_1 = \cosh^{-1}(\frac{S_{1\infty}^2 - S_{2\infty}^2 + 2\cosh Y_2}{2})$. This leaves only Y_2 and H as unknowns in Equation 2.38. Again, for any meaningful Y_2 value entered, a corresponding H value will result. In this case, the Y_2 values should be selected between the surface potential at infinite separation ($Y_{2\infty}$) and an arbitrary large positive surface potential which would develop at very close distances.

2.1.3. Total Force of Interaction and the Derjaguin Approximation

The vdW interactions are mainly determined by the bulk of the interacting bodies and therefore are not affected significantly by solution chemistry. The electrostatic interactions, on the other hand, are strongly influenced by the chemistry of the solution and therefore are usually manipulated to obtain desired rheology or stability in a given system. The sum of the van der Waals (Equation 2.8) and electrical double layer pressures (Equation 2.37) gives a theoretical net force of interaction F_{DLVO} per unit area of the plates.

The force between two surfaces depends on both the material properties and the geometry of the surfaces. Derjaguin approximated the influence of arbitrary geometry on the interaction potential U(D) by reducing it to the simple geometry of two flat surfaces. The Derjaguin approximation relates the energy per unit area between two planar surfaces U_{DLVO} which are separated by a gap of width x to the energy between two bodies of arbitrary shape U which are at a distance D:

$$U(D) = \int U_{DLVO}(x)\, dA \tag{2.44}$$

Here, dA is the variation of the cross-sectional area of the two real surfaces with increasing separation distance as shown in Figure 2.4. The integration runs over the whole cross-sectional area. For forces the analogous expression is

$$F(D) = \int f_x\, dA \tag{2.45}$$

where F is the force between two bodies of arbitrary shape and f is the force per unit area between two flat surfaces.

In colloidal particle and planar surface the geometry is a sphere approaching a flat planar surface. Colloidal particle is spherical with a radius of curvature R. Then dA = 2πr dr and the radial coordinate r and the height D are related by

$$x = D + R - \sqrt{R^2 - r^2}\ , \qquad rdr = dx\sqrt{R^2 - r^2} \tag{2.46}$$

If the range of the interaction is much smaller than R we only need to consider contributions with r much smaller than R and r dr = R dx. This is precisely valid if the tip has a parabolic shape with radius of curvature R. A parabolic tip shape is described by $x = D + r^2/2R$. Inserting leads to

$$F_D = 2\pi R \int_x^{\infty} U_{DLVO}(x)\, dx \tag{2.47}$$

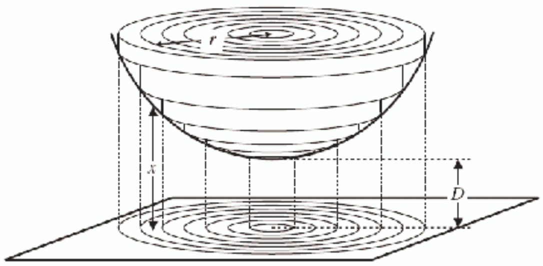

Figure 2.4. Schematic illustration of Derjaguin’s approximation for a rotational symmetric body interacting with a planar surface (Source:Butt and Kappl, 2010).

CHAPTER 3

ATOMIC FORCE MICROSCOPY

Developments in the microscopy field, as in control, manipulation and measurement devices on a nanoscopic scale, led to the invention of the Scanning Tunneling Microscope (STM) by Binnig and Rohrer in 1982. Shortly afterwards, in 1986, Binnig, Quate and Gerber invented the Atomic Force Microscope (AFM) (Binnig et al., 1986). STM relies on measurement of exponentially decaying tunneling current between a metal tip and a conducting substrate. Since its invention and the recognition for its inventors of the Nobel Prize in 1986, STM has found a wide use in studies of inorganic materials, organic material and dynamic processes, including reactions. Not being restricted to conductive materials, AFM is a much more versatile instrument than STM and more adopted in studies applied to colloidal systems and soft matter. The number of publications related to AFM has increased constantly since its invention, and the instrument is now a fundamental tool in most research laboratories of the world. The Atomic Force Microscope probably earned its initial popularity in virtue of its capability of providing images of samples with atomic resolution in vacuum, air or liquid environment. The materials being investigated are almost endless: thin and thick film coatings, ceramics, composites, synthetic and biological membranes, biological macromolecules, metals, polymers, and semiconductors. The AFM is being applied in several fields of research, such as materials science and engineering, biochemistry and biology, in studies of the most varied phenomena, such as colloidal stability, characterization of nanostructures and molecules, adhesion, surface elasticity, corrosion, etching, friction and lubrication.

3.1. Surface Force Measurement Techniques; SFA and AFM

The atomic force microscope (AFM) is designed to provide high-resolution (in the ideal case, atomic) topographical analysis, applicable to both conducting and nonconducting surfaces (Morita et al., 2002) (Birdi, 2003). The basic imaging principle is very simple: a sample attached to a piezoelectric positioner is rastered beneath a sharp tip attached to a sensitive cantilever spring. Undulations in the surface lead to deflection of the spring, which is monitored optically. Usually, a feedback loop is employed which holds the spring deflection constant, and the corresponding movement of the piezoelectric positioner thus generates the image. A schematic representation of the technique is shown in Figure 3.1. From this, it can be seen that the scanning AFM has all the attributes necessary for the determination of surface and adhesion forces; a sensitive spring to determine the *force*, a piezoelectric crystal to *alter* the separation of the tip and surface, which if sufficiently well-calibrated also allows the *relative separation* of the tip and surface to be calculated. It is customary to disable the in-plane (*x*,*y*) motion of the sample and focus solely on sample motion normal to the sample surface (*z*), although for *frictional* force measurements this is not the case. An example of the raw data obtained for a force measurement is reproduced in Figure 3.2.

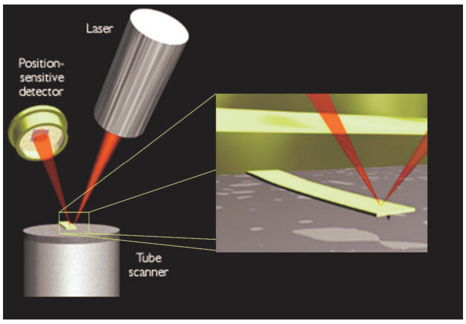

Figure 3.1. Schematic diagram of an AFM.
(Source:http://www.sci.sdsu.edu/~smaloy/Research/AtomicForceMicroscopy.htm)

The speed of the piezoscanner can typically be varied over at least a three-orders-of-magnitude range. One can routinely quantify both the net surface force (and its separation dependence) as the probe *approaches* the sample and any adhesion (pull-off) force on *retraction*. In this respect, there are some obvious parallels to be drawn with the surface force apparatus (SFA) (Israelachvili and Adams, 1978). Measurements with atomically smooth mica with the SFA have resulted in the confirmation of interaction and adhesion theories and have also led to the elucidation of a number of additional forces of varying range, magnitude, and sign that affect the fundamental interaction between surfaces in liquid media (Israelachvili, 1991). This technique is unparalleled for high-resolution force measurement and has the advantage that the absolute separation of two surfaces can be directly measured. However, since it uses the interference patterns to measure the distance between the surfaces, it requires materials which transmit light. Therefore it can only be used for limited materials. Also, the SFA technique cannot scan a surface, but can only be used for point measurements of force.

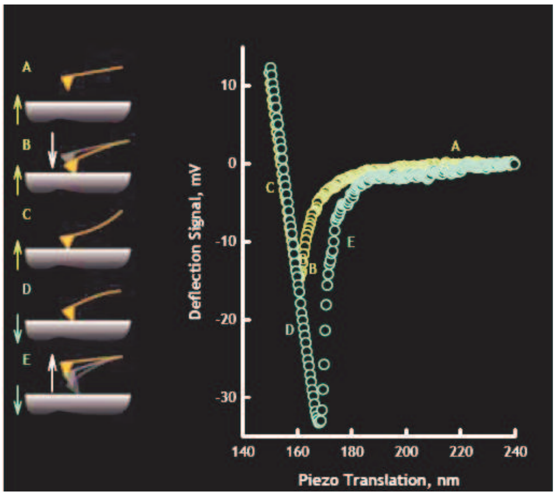

Figure 3.2. The principle of obtaining a force curve from an AFM**.** The X-axis gives the actual movement of the piezo in z-direction whereas the Y-axis is the signal related to cantilever deflection (Source: Polat et al., 2006)

AFM, on the other hand, is not hampered by these limitations and can be used with almost all materials. If the interest is the interactions between the surfaces, a particle of almost any material can be attached to the end of the cantilever and its interaction with any other surface can be studied. This important method was pioneered by Ducker et al. (1991) and is referred to as *colloid probe microscopy*. The colloidal particle is used in this application are typically in the range 1–20 μm .

Scanning probe microscopy can also be used to map the surface of materials for specific purposes. For example, if the tip is made to interact with the surface magnetically, the scan will result in magnetic interactions between the tip and the surface. If the tip is covered by a specific chemical, then the scan will give a map of the chemical interactions between the tip and the surface.

3.2. Types of AFM Cantilever, Probes and Tips

The first direct measurements of forces with the AFM both in air and in water (Burnham and Colton, 1989), (Senden and Drummond, 1995), (Hutter and Bechhoefer, 1994), (Eastman and Zhu, 1996), (Weisenhorn et al., 1992) were performed using a sharp pyramidal tip as a probe. In these cases, the tip geometry was either complicated or totally unknown, which made comparison of the experimental data with theories very difficult. Then diamond shards glued to the end of cantilevers (Butt, 1991). Nowadays microfabricated tips, or particles attached to the end of a cantilever are used. Commercially available microfabricated tips are made from silicon nitride or silicon as shown in Figure 3.3. Both materials are oxidized under ambient conditions. To tune their properties they are often modified. Cantilever types also will be select depend on the study which were given in Figure 3.4, triangular and rectangular shape cantilever are commercially available.

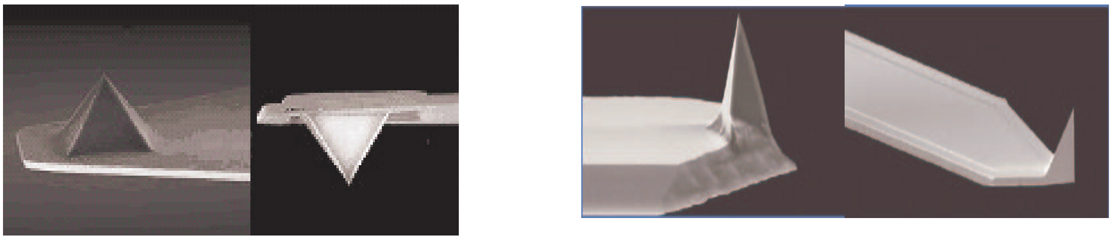

a b

Figure 3.3. Typical pyramidal AFM probe a) silicon nitride, b) silicon (Source: Veeco Probe Catalog).

a b

Figure 3.4. Types of cantilever used in AFM, a) Triangular cantilever, b) Rectangular cantilever (Source: Veeco Probe Catalog).

3.2.1. Colloidal Probe (Particle Attachment Technique)

Colloidal Probe Atomic Force Microscopy requires a tip of known shape to be mounted cleanly on a consistently reproducible cantilever. These probes are known as “Colloidal Probes” and are used to study colloidal interactions between two surfaces and to quantify the interactive properties. The tip is formed using a spherical, colloidal particle that is attached to a tipless cantilever. Particles are typically attached to the end of AFM cantilevers by micromanipulators under an optical microscope. They are glued, with either a chemically inert thermotropic resin, or polymerizable glues (either UV or chemically cured) using a fiber of appropriate size and material properties. Smooth, spherical colloids are preferable for quantitative measurements.

Particles of less well-defined geometry may also be used, but a greater degree of scatter in the measured force data can be expected. In early work, the lower limit to the size of the colloid probes was dictated by the height of the AFM tip (4 μm), but the availability of "tipless" cantilevers removed this particular size restriction and the particle size now depends solely on the resolution of the microscope.

A micromanipulator is used to control the spatial positioning of a fiber with respect to the cantilever, which is placed under a microscope objective lens (Ducker et al., 1992), (Toikka et al., 1996). An example of manipulator is shown in Figure 3.5.

First colloidal probe was built by Ducker et al., 1992 which was given in Figure 3.6. The silica sphere was attached to microfibricated AFM cantilever. After this application many researchers were made their AFM probes by using same method.

Polat et al. (2006-b) used a manipulator equipped with two independent XYZ arms and independent XY stage, all of which capable of 0.1 μm translation resolution, to prepare colloidal probes. Some example pictures of alumina particles being manipulated and of colloidal probe glued on tippless cantilever are given in Figure 3.7. A representative picture of the particles attached cantilever is shown in Figure 3.8.

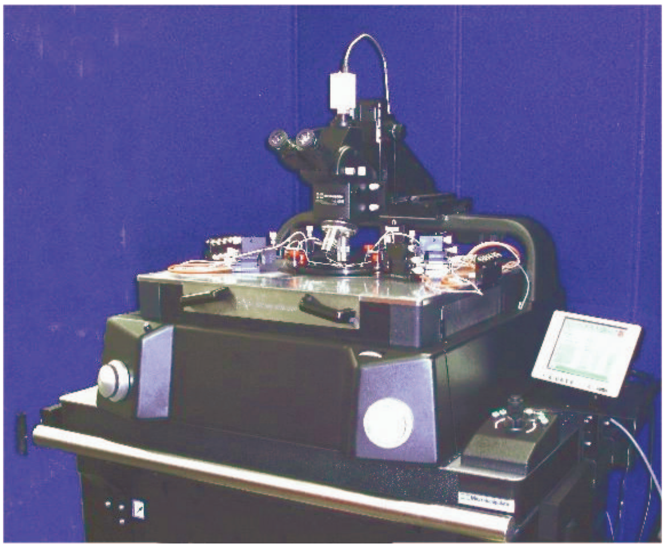

Figure 3.5. Apparatus used to glue particles to the end of AFM cantilevers (Source: http://www.micromanipulator.com/products/product.php?item=360&cat=10#).

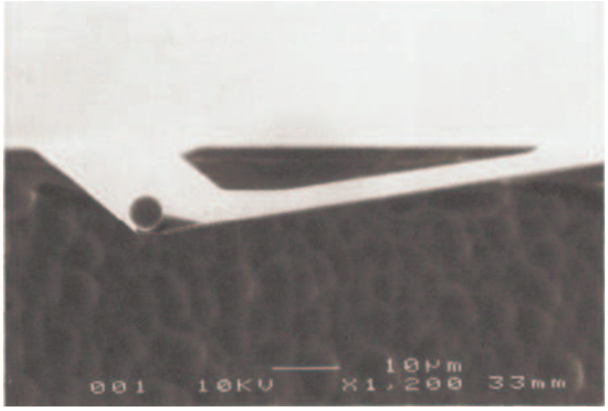

Figure 3.6. First colloidal probe

(Source: Ducker et al. 1992).

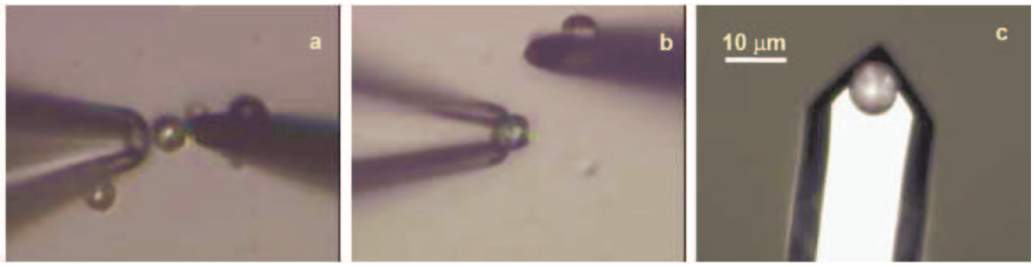

Figure 3.7. Manipulation of the colloid probes and placement on a triangular cantilever using micromanipulator system (the scale in 5-c applies to 5-a and 5-b also) (Source: Polat, et al. 2006).

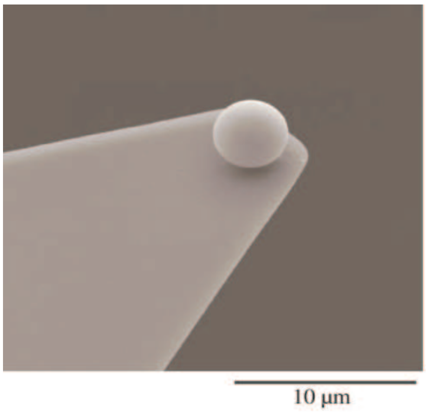

Figure 3.8. Scanning electron micrograph of silanized silica microsphere glued to the end of a tipples atomic force microscope cantilever (Source: Kappl and Butt, 2002).

3.3. Calibration of Cantilever Spring Constant

Quantitative force measurements require an accurate value of the cantilever spring constant, which has a Hookean response over the range of deflections encountered in force measurements. In early work, nominal (unmeasured) values supplied by the manufacturers were used (Ducker, 1991). However, these values are seldom better than a rough guide and there is sufficient variation even between cantilevers from the same batch to necessitate their individual calibration. This is because the techniques used to fabricate the probes can result in substantially different cantilever dimensions, especially thickness, from wafer to wafer and smaller variations within a single wafer. In principle, the spring constant can be calculated from knowledge of the cantilever's geometrical and material properties (Neumeister and Ducker, 1994), (Sader et al., 1995). Many techniques have since been proposed to characterize cantilever spring constants. These can generally be grouped into three categories: "Dimensional models" where fully theoretical analysis or semi-empirical formulas are used to calculate the cantilever spring constants based on their dimensions and material properties, "Static deflection measurements" where the spring constant is determined by loading the cantilever with a known static force, and "Dynamic deflection measurements" where the resonance behavior of the cantilever is related back to its spring constant.

Various methods to measure the cantilever spring constant have been proposed and, for historical reasons, are briefly catalogued here. Butt (1991) placed a small pendulum against a vertically mounted cantilever and by slightly tilting the set-up applied an adjustable force to the cantilever. Senden and Ducker, (1994) proposed a simple static deflection method which employs the attachment of a tungsten sphere (10–50 μm in diameter) of known mass to the end of the cantilever. The spring constant can also be estimated from a power spectral density analysis of the thermal vibration of the free cantilever, i.e., not interacting with a surface (Hutter and Bechhoefer, 1993). However, among these the recent reviews by Sader (2002) and Sader et al., (2004), Cook et al. (2006), Hutter and Bechhoefer, (1993), and Butt et al. (2005) are very good and are highly recommended reading.

The most preferable method for determination of the spring constant involves measurement of the shift in the resonant frequency of the cantilever when loaded with particles of known mass and is often referred to as the Cleveland Method (Cleveland, 1993).

Sader et al. (1999, 2004) have performed a finite element analysis of the static deflection of rectangular cantilevers and presented exact numerical results for the spring constant for a variety of cantilever dimensions. Once again, the thickness and modulus were needed to be known. Experience proves that such calculated values do not necessarily agree well with accurate experimental ones, thus, direct measurement of the *k* is preferred.

The results of the analysis of spring constant calculation methods are shown in Table 3.1, which lists the estimated uncertainty for each method due to measurement errors along with the particular measurements that dominate the overall uncertainty (Ohler, 2007).

The other surprisingly large error is that for the added mass method. Here even modest 5% uncertainty in the particle diameter contributes almost 15% uncertainty to the spring constant. In order to reduce the error it would be important to use larger particles where the relative uncertainty in diameter is lower.

Table 3.1. Overall uncertainty in spring constants.
(Source: Ohler, 2007)

Method	Uncertainty	Main source of error
Simple beam	~16%	Cantilever thickness
PBA	~26%	Elastic modulus of SiN
Freq. Scaling	~9 %	Si density
Reference cantilever	~9 %	Deflection sensitivity
Added mass (Clevaland Method)	15-30 %	Particle Diameter
Sader	~4 %	Cantilever width
Thermal tune	~ 8 %	Deflection sensitivity

The Sader method assumes a perfect rectangular cantilever, which is often only an approximation of reality. The added mass method is actually based on simple beam theory and is only extended to v-shaped levers by the basic parallel beam approximation. While difficult to quantify the uncertainty that they contribute, it is best to understand these various limitations.

Based on available information, the most reliable method for determination of the spring constant is the Sader method (Table 3.1). Details of this method in Chapter 6, Section 6.4.2.

CHAPTER 4

FORCE MEASUREMENT BY ATOMIC FORCE MICROSCOPY

The atomic force microscopy (AFM) is not only a tool to get topography of surfaces but also to measure force-distance curves. Such curves briefly called force curves provide valuable information about properties of materials such as, elasticity, hardness, Hamaker constant, adhesion, surface charges and charge densities. For this reason the measurement of force curves has became essential in different fields like surface science, material science and biotechnology. Force measurements by Atomic Force microscopy have been intensively investigated by many researchers. They were used various substrates and tips to measure forces between them in air, N_2 or aqueous solutions because of capability of AFM. In this chapter, principal of force measurement and examples of surface force measurements by AFM were explained in detail.

4.1. Principle of Force Measurement

A force measurement is made by ramping the probe and substrate together and monitoring cantilever deflection as a function of displacement. In some devices, the cantilever is mounted on the piezo and it is the probe that is moved, in other devices, it is the substrate that is ramped. An example of the latter case is depicted in Figure 4.1.

The types of forces that may act between the surfaces and their characteristic distance dependences are fully documented elsewhere (Israelachvili, 1991; Claesson et al., 1996; Hodges, 2002;Polat; 2006-b). These forces acting between the surfaces cause the cantilever to deflect prior to their physical contact. The vertical axis of Figure 4.1 shows the output of the photodiode, whilst the horizontal axis shows the position of the piezo. The curve A-B-C shows the interaction on approach and the other (in this case with a deep adhesive minimum) corresponds to the interaction upon retraction. At large distance (A), no force acts on the particle. At shorter separations (B), a surface force may be experienced either as an attraction (as in Figure 4.1) or repulsion. When the particle and flat surface come into physical contact, the probe movement complies with the movement of the piezo. It is this linear region that is used to calibrate the deflection voltage in terms of distance units (C). This part of the curve is often called the *constant compliance region*. The piezo movement is then reversed. If the contact is adhesive (almost always the case in air, for example), then the surfaces remain in contact until the restoring force in the spring overwhelms the adhesive force (D, E) and the cantilever will snap off the surface into its equilibrium position (F).

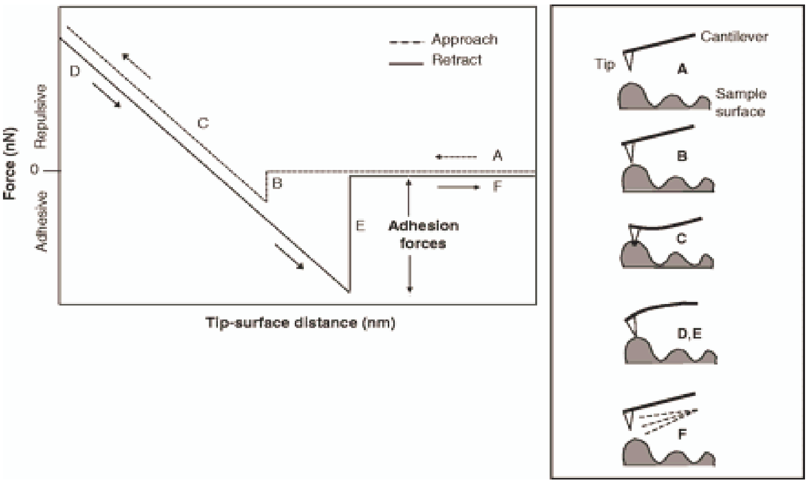

Figure 4.1. Idealized force-distance curve describing a single approach-retract cycle of the AFM tip, which is continuously repeated during surface scanning (Source: http://jcs.biologists.org/cgi/content-nw/full/118/13/2881/FIG1).

4.2. Surface Force Measurements by AFM

The well-known DLVO theory provides a theoretical tool for predicting the forces acting in colloidal systems. This theory states that the net energy of interaction is a sum of electrical double layer and van der Waals forces as discussed in Chapter 2. The DLVO theory predicts relatively good predictions for aqueous solution by AFM for different materials. Main parameter of measuring forces between tip and surface is how charges arise on the tip and the surface.

With the AFM DLVO forces were measured between several materials which are of special interest in colloidal science, e.g. glass, silica, and silicon nitride (Butt, 1991), (Larson et al., 1997), (Freitas and Sharma, 2001), (Lee and Sigmund, 2001 and 2002), (Dreleich and Long, 2006); gold (Ducker et al, 1992), (Biggs et al., 1994), (Larson et al., 1997); zinc sulphide (Toikka et al. 1998); titanium oxide (Larson et al., 1993 and 1995); zirconia (Biggs, 1995), (Hook et al., 1999), (Pedersen and Bergstrom, 2000); iron oxide (Toikka et al., 1996); magnesium oxide (Kauppi, et al. 2005); and alumina (Karaman and Pashley, 1997), (Meagher et al., 1999), (Franks and Meagher, 2003), (Nowostawska et al., 2005), (Gan and Franks, 2006), (Polat et al., 2006).

DLVO theory states that the net energy of interaction is a sum of van der Waals forces and electrical double layer. The capability of AFM in probing van der Walls forces with high distance and resolution had already demonstrated by many researchers. (Li et al., 1993), (Larson et al., 1993), (Arai and Fujihara, 1994), (Biggs et al., 1994), (Drummond and Senden, 1994), (Senden et al., 1994), (Eastman and Zhu, 1996), (Toikka et al., 1996). Some of the experiments have been performed in air or dry nitrogen which was tabulated in Table 4.1. Even if measured quantities have a large uncertainty, they often show a valid trend with surface energies.

Table 4.1. Measured attractive force F_{attr}, adhesion force F_{ad}, and surface energy γ_s for experiments in air or in dry nitrogen: (a) The tips are colloidal particles, the data in the parenthesis are calculated data.

Ref.	Tip Radius (nm)	Tip material /medium/sample	Measured		
			F_{attr} (nN)	γ_s (mJ/m^2)	F_{ad} (nN)
Li et al., 1993	100-200	Tungsten/Dry N_2/Gold Tungsten/DryN_2/ Graphite	≅ 750 ≅ 140	270-540	≅ 750 ≅ 250
Arai and Fujihara, 1994	27.5	Tungsten/Air/Graphite		15-40, 60-80	**≅ 24**
Eastman and Zhu, 1996	100	Si_3N_4/Air/Mica Gold/Air/Mica Paraffin/Air/Mica			192(184) 51(48) 17(16)
Toikka et al., 1996	5000$^{(a)}$	Iron oxide/Air/Silica		3(163)	

Some of the researchers also were measured attractive force and adhesion force between tip and surface in water. Larson et al., (1993) was measured TiO_2 tip with radius 9 μm and TiO2 substrate and they were measured Hamaker constant 6 10^{-20} J by AFM. Attraction forces between Gold particle and gold substrate was investigated Biggs, et al.,(1994). Drummond and Senden (1994) measured Hamaker constant between Si_3N_4-Si_3N_4 and Si_3N_4-Mica. Iron oxide tip radius 5 μm and silica substrate was measured adhesion force by Toikka et al. (1996).

Force-displacement curve on silicon nitride in water at pH 6 with a silicon nitrate tip were seen in Figure 4.2. Both attractive and adhesion forces become nearly 10 times smaller than in air and the van der Waals force makes the greatest contribution to adhesion since the meniscus has been removed. Also the pull-off distance is reduced by a factor of 10 (Senden et al.,1994).

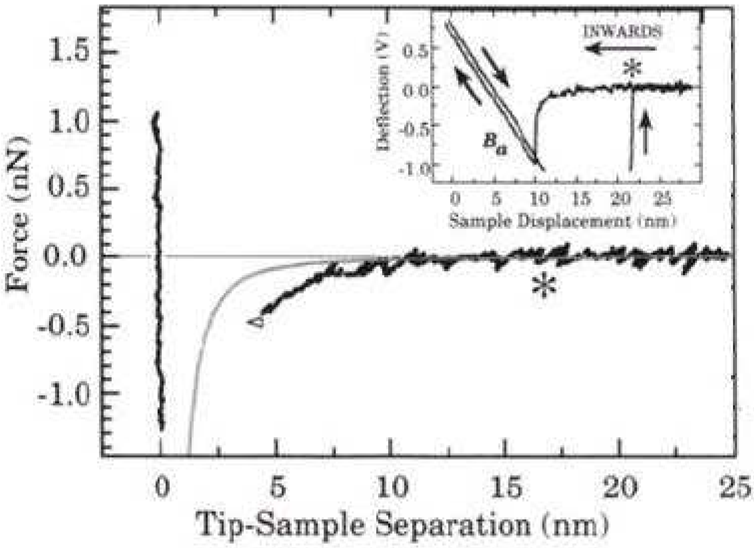

Figure 4.2. Force-displacement curve on silicon nitride in water (pH 6) with a silicon nitride tip (R between 50 and 100 nm). Note the inverse path effect on the contact lines (Source:Senden et al., 1994).

Electrostatic force by AFM measurement was investigated many researches which their experimental results were given below. Butt (1991) measured the forces between silicon nitride tip and the substrate mica. The electrolyte is KCl and the Debye length is varied by varying the KCl concentration at constant pH. The force-displacement curves at different concentrations are depicted in Figure 4.3.a. Increasing the concentration up to 100 mM, three changes occur: the repulsive force becomes smaller and smaller; its decay length diminishes; the van der Waals force appears.

At 100 mM KCl concentration, the force-displacement curve resembles the one in deionized water. Since deionized water is a weak electrolyte (10^{-7} M in both H_3O^+ and OH^-), it should show the highest double-layer force. However, this long range force is acting on distances well beyond the range of the AFM tip motion. Therefore, it is not possible to detect the actual zero line and to define the zero force reference.

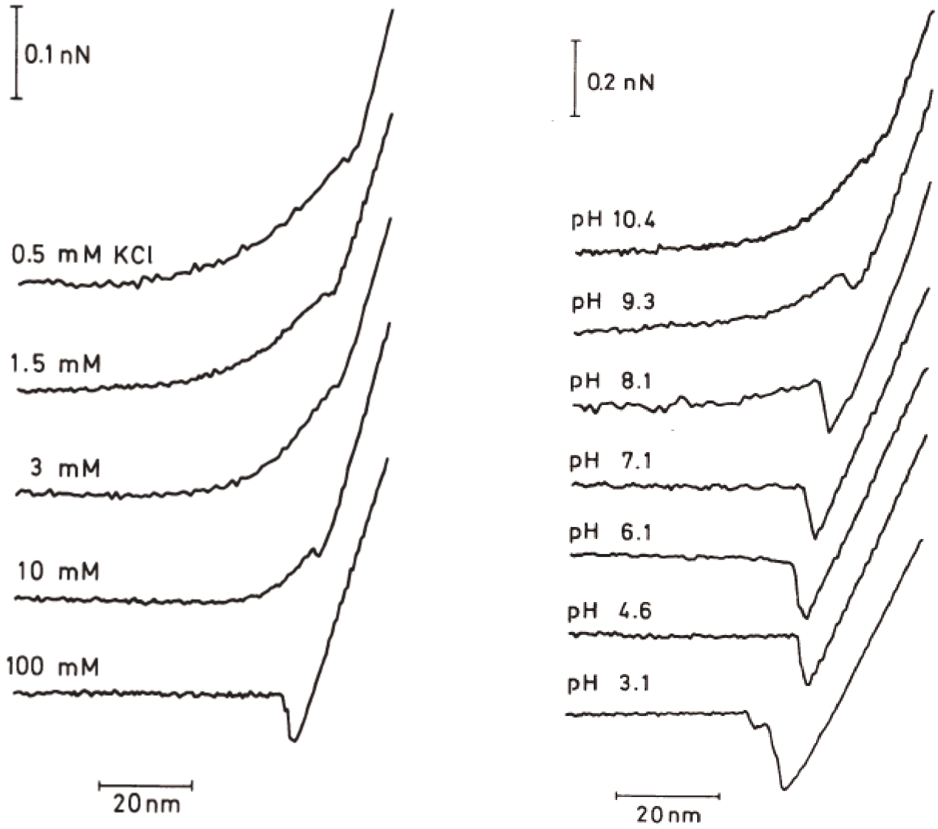

a

b

Figure 4.3. Force versus distance curves measured a) at different KCl concentrations with a silicon nitride tip on mica, b) at different pH values with an alumina tip on mica (Source: Butt, 1991).

Similar series of curves can be obtained in other electrolyte solutions, e.g., $MgCl_2$ (Butt, 1991), $CaCl_2$ (Karaman and Pashley, 1997). Using a 2:1 salt, the Debye length decreases, and the double-layer force vanishes at a 30 mM concentration. In order to measure the dependence of double-layer force on tip and/or sample surface charge, a sample whose surface charge density depends on pH has to be employed. Butt (1991) has shown the transition from double-layer force to van der Waals force for an alumina tip on mica. Mica is negatively charged at any pH value, whereas alumina is positively (negatively) charged below (above) pH 8.1. The forces are repulsive above pH 8.1 and attractive below pH 8.1 as shown in Figure 4.3.b.

As another example of the force-versus-distance in 0.1 mM KNO3 solution between a silica particle and a titania flat is shown in Figure 4.4. Force curves were recorded at different pH values ranging from pH 8.8 for the top curve to pH 3.0 for the bottom curve. The surface charges of both materials are mainly determined by the pH. Silica has an isoelectric point around pH 3.0, while the isoelectric point of titania is pH 5.6. As a consequence at high pH, where both materials are negatively charged, an electrostatic repulsion is observed. The repulsion decreases as the pH decreases, and at pH 3.0, i.e. below the isoelectric point of titania, there is an electrostatic attraction as well as a van der Waals force resulting in an overall attraction between the two surfaces (Larson et al., 1995).

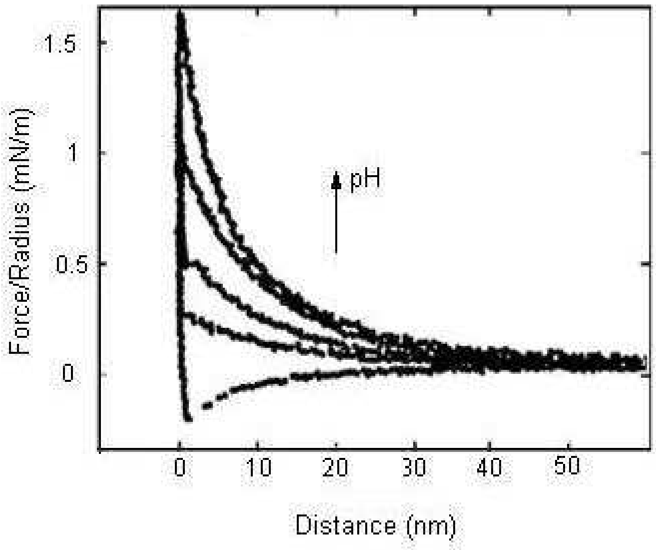

Figure 4.4. Examples of force, scaled by the radius of the colloid probe, versus separation curves for the silica- titania system. The curves correspond to pH values, from top to bottom, of 8.8, 7.2, 6.3, 5.3, and 3.0. The iep of silica is around pH 3, while the iep of titania is around pH 5.6. The degree of electrostatic repulsion decreases as the pH decreases, and at pH 3.0, below the iep of titania, there is an electrostatic attraction as well as the van der Waals attraction resulting in an overall attraction between the two surfaces (Source: Larson et al., 1995)

The direct force measurements with AFM have shown that oxide-solution interface displays an unusual behavior which cannot be accounted for by the DLVO theory, especially at short distances of separations (Velamakanni and Chang, 1990; Karaman and Pashley, 1997; Meagher et al., 1999). One of the explanations of such behavior was to invoke an additional repulsive ‘hydration force’ at separations shorter than 5 nm. Karaman and Pashley (1997) using AFM and colloid probe method observed that plasma-oxidized alumina-sapphire surfaces always demonstrated repulsive forces within pH range 3-6.5. Though the forces were accurately represented by the DLVO theory at separations larger than 3-5 nm, they were not able to see a distinctive energy barrier and a primary minimum in any of the cases they studied. It was surprising that at pH 6.5 where the sapphire and α-alumina surfaces were supposed to be oppositely charged (Franks and Meagher, 2003) persistently repelled each other. They attributed this behavior to the development of a thick repulsive hydrated layer up to 15 nm thick at basic pH values due to the swelling of the alumina surface. However, no force curves were provided for the basic pH values. They also stated that there was no evidence of a 'thick' gel formation and suggested a 'thin' gel at lower pH values which to a degree conflict with the always-repulsive interaction energy observed at pH 3. Polat et al. (2006) have been produced alpha and gamma alumina spherical tips and investigated pH and hydration effect on the normal and lateral interaction forces between alumina surfaces.For an α-alumina–sapphire system at acidic pH, the force curve exhibited a well-defined repulsive barrier and an attractive minimum. At basic pH, the interactive force was repulsive at all separations with no primary minimum. Lateral force measurements under the same conditions showed that frictional forces were nearly an order of magnitude smaller at basic pH than those observed at acidic pH. This behavior was attributed to the hydration of the alumina surface. According to normal and lateral force measurements of ρ-alumina, surfaces of ρ-alumina were strongly hydrated.

Several studies have been dedicated to the double-layer force on oxide-like materials. Raiteri et al. (1996) have studied the pH dependence of forces for Si_3N_4 tips on Si_3N_4, Al_2O_3, and mica, demonstrating the capability of AFM in determining the Point Zero Charge (PZC) of such materials. For Si_3N_4 on Si_3N_4, forces are always repulsive with the exception of a range around pH 6-7. This means that the tip and sample always bear a charge of the same sign and that the PZC is around pH 6.5. For Si_3N_4 on mica the total tip-sample force changes from attractive (for $pH \leq 6$) to repulsive ($pH \approx 8$). This is consistent with the fact that mica is negatively charged and the PZC of silicon nitride tip is around pH=6.5. For Si_3N_4 tips on Al_2O_3 the forces are always repulsive, with a repulsion minimum at pH=4.3. Hence the PZC is between pH=4 and pH=5.

Similar results have been obtained by Karaman and Pashley (1997) for an Al_2O_3 substrate with aluminum or Si_3N_4 tips, and by Senden and Drummond (1995) for mica with a silicon nitride tip. In this work, the pH dependence of double-layer force with and without background electrolyte is investigated, and measurements at constant pH with different electrolyte concentrations have been performed. The curves are fitted taking into account both the Van der Waals force and double-layer force.

Arai et al. (1996) have measured the PZC of Al_2O_3, SnO_2, and SiO_2 with a Si_3N_4 tip in buffer. The PZC are measured by monitoring the amplitude of the repulsive or attractive forces at different pH (2-12) at a distance corresponding to $(½)\kappa^{-1}$, where κ^{-1} is Debye length, i.e., 15 nm, in order to make van der Waals force negligible. For Al_2O_3 the results agree with those of Raiteri et al. (1996).

Lin et al. (1993) have once more studied the isoelectric point (IEP) for a silicon nitride tip on SiO_2 with two different methods. The IEP due to silicon nitride is 6.2 ± 0.2 and 5.8 ± 0.4.

Larson et al. (1993) have compared the determination of the potentials by means of the AFM with the electrophoretic determination. The system employed was a TiO_2 colloidal sphere on TiO_2. A good agreement between these two methods is found. In later works, the same comparison is established for a silica colloidal sphere on TiO_2 and on silica (Larson et al., 1995). Once again there is a good agreement between the two methods.

Drummond and Senden (1994) have demonstrated that the double-layer force between a silicon nitride tip and mica in hexadecyltrimethylammonium bromide (CTAB) is intermediate between the theoretical constant surface charge fit and the theoretical constant potential fit. The double-layer force between a silicon nitride tip and various surfaces also investigated by many researchers. (Toikka et al., 1996, Rutland and Senden, 1993, Larson et al., 1995, Atkins and Ninham, 1997, Drummond et al., 1997).

Biggs et al. (1993) have measured force-distance curves between a gold colloidal sphere and a gold flat substrate in different solutions. They verified the increasing of the strength and decay length of double-layer force with decreasing ion concentrations (NaCl, trisodium citrate or gold chloride). By fitting the experimental data both with the constant charge force and the constant potential force, the authors were able to establish that the charge, and hence the adsorbed ions concentration, is constant. Also the dependence of double-layer force on pH was studied. Kane and

Mulvaney (1998) have investigated double-layer interactions between self-assembled monolayers of ω -mercaptoundecanoic acid on gold surfaces.

Drummond and Senden (1994) have exploited the double-layer force in order to determine the effective radius R_{eff} of a pyramidal tip. The method is based on comparing the forces measured with the colloidal probe and the forces measured with the pyramidal tip at a certain reference distance from the sample surface, thus obtaining a scaling factor that can be used to normalize the force measured at all other distances. The reference distance is chosen in order that the contribution of the van der Waals force and of other forces is negligible (typically it is 15 or 20 nm) and the entire force is due solely to the double layer. Furthermore, at such distances, also the difference between the two boundary conditions, i.e., constant charge and constant potential, is negligible.

The study of the double-layer force has perhaps given the best results in AFM studies of forces. The capability of the instrument in characterizing this force with high resolution in any kind of liquid solution and with any kind of surfaces is fully demonstrated. The dependence of the force on the pH of the solution or on the salt concentration has been extensively studied for several kinds of systems. The AFM is routinely used to measure the Debye length of solutions, to determine the PZC of materials, and to calculate the surface charge density of substrates. The forces at a liquid/liquid interface, the dependence of forces on applied potentials and the study of ions adsorption at interfaces are now the most intriguing issues.

Toikka et al. (1996) have showed that, because of microasperities, the liquid is not completely squeezed out at contact and a thin layer of liquid stays between the tip and the sample, thus exerting a double layer force that decreases the adhesion force. Therefore, the apparent adhesion force depends on pH. The authors found an evidence of this phenomenon measuring adhesion forces at different pH between an iron oxide colloidal probe and silica. The silica surface is negatively charged at $pH > 2$, while the iron oxide surface is negatively charged at $pH > 6$. Thus, for $pH > 6$, there is a repulsive double-layer force. If the liquid was completely squeezed out at contact, adhesion force would not depend on pH. But this is not the case, experimentally, as the adhesion decreases with increasing pH for $pH < 6$ and is zero for $pH > 6$.

Freitas and Sharma (2001) have measured the hydrophilic–hydrophilic, hydrophilic–hydrophobic and the hydrophobic–hydrophobic adhesion in water, KCl solution and ethanol, obtaining a good qualitative agreement with the values predicted by the acid–base theory. In water the higher adhesion is obtained for the hydrophobic–hydrophobic system, followed by the hydrophilic–hydrophobic and by the hydrophilic–hydrophilic system.

Polat and Polat (2010) recently developed an analytical solution for interacting parallel plates which carry arbitrary potentials. Those equations were shown to be perfectly valid for all surface charging conditions, low or high. According to this work, one can relate the gap between the interacting plates to the surface charges and surface potentials developing on both plates at that separation. Comparison with the numerical shooting procedure and new analytical solution of the potential profiles between interacting two plates for several highly charged surface conditions examined, it can be seen that identical results obtained from both methods.

CHAPTER 5

SURFACE CHARGING OF METAL OXIDES

Aqueous dispersions of metal oxide particles are of great practical interest due to their wide-ranging industrial applications and everyday uses under the conditions required. The latter involves the broad variability of pH and dissolved materials among them electrolytes which have definite role in charge neutralization in the vicinity of particle surface. The pH-dependent surface charging of metal oxides due to the specific adsorption of H^+/OH^- in the presence of indifferent and specific ions, and other simultaneous processes at solid/water interface such as hydration of surface, dissociation of surface sites, dissolution of solid matrix, then hydrolysis of dissolved ions are important in these systems. There are excellent reviews and books about surface chemistry of oxides by Dzombak and Morel (1990), Stumm and Morgan (1996), Conley (1996), Kosmulski (2001) and Kosmulski (2009).

5.1. Determination of Surface Charge of Metal Oxides by Electrophoretic Measurement

When an electric field is applied across an electrolyte, charged particles suspended in the electrolyte are attracted towards the electrode of opposite charge. Viscous forces acting on the particles tend to oppose this movement. When equilibrium is reached between these two opposing forces, the particles move with constant velocity. The velocity of the particle is dependent on the following factors: Strength of electric field or voltage gradient, the Dielectric constant of the medium, the Viscosity of the medium, the Zeta potential. The velocity of a particle in an electric field is commonly referred to as its Electrophoretic mobility. Figure 5.1 shows that many suspended and colloidal solids encountered in waters soils have a surface charge. This charge may be strongly affected by pH. There are excellent books and reviews about surface chemistry by Kosmulski (2001), Kosmulski (2009) and Kosmulski (2011). Kosmulski (2009) gave Tables about pH-dependent surface charging and points of zero charge of dozens of publications reporting pzc of oxide materials. Kosmulski (2011) gave table which was tabulated extra literature work about pH-dependent surface charging and points of zero charge of dozens of publications reporting pzc of oxide materials between the years 2009-2011.

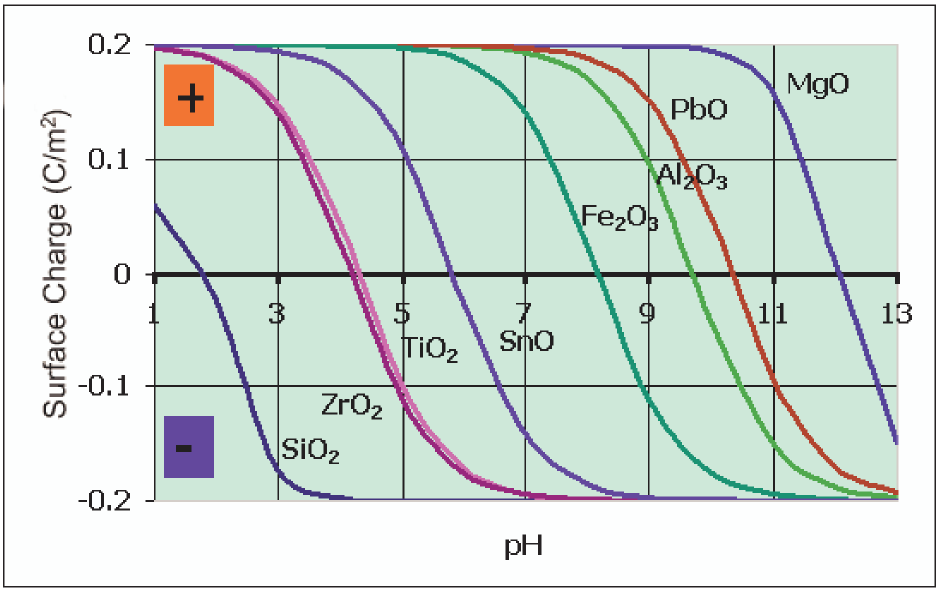

Figure 5.1. Surface charge of metal oxides (Stumm and Morgan, 1996).

5.2. Determination of Surface Charge of Metal Oxides by Potentiometric Titration

In aqueous solutions, dissolution of electrolytes results in formation of ionic species, and formation of solid-water interface involves hydration and charging of surface. The ionic species accumulate at interface, which is in fact a chemically controlled distribution of charged species governed by the in situ developed electrified interfaces. Chemical contribution of components cannot be neglected in general; simultaneous equilibria exist both in aqueous phase and at surface which mutually influence each other.

In the case of oxides, under coordinated metal ions (e.g., Si^{4+}, Al^{3+}, Fe^{3+}) occurring on the top layer of oxide surfaces react with water molecules to form surface OH groups in an attempt to complete their coordination sphere. In the presence of water the surface of oxides, e.g., SiO_2, Fe_2O_3, Al_2O_3, TiO_2, are generally covered with surface hydroxyl groups (S-OH sites). For most of the oxides dissociative chemisorption of water molecules seems energetically favored (Stumm and Morgan, 1996).

Potentiometric titration is a method, where a colloidal system is titrated with a specific titrant to estimate the surface charge of solid by comparing the titration of solution with solid against titration of the same solution without solid. The difference of titrant quantity between respective points characterized by the same pH value allows to estimate the influence of solid on the equilibrium. The difference depends on the system, whether such differences may explained by an electric charge created on solid surface (e.g. silica, alumina or other oxides) or dissolution of solid or both phenomena. Another possibility is e.g. presence of some impurities remaining after synthesis. With the potentiometric titration were measured between several materials which are of special interest in colloidal science, e.g. glass and silica, Jorgensen, (1967), House (1992), Mullet et al., (1997), Duc et al., (2006) ; silicon nitride, Whitman and Feke (1988), Bergström and Pugh (1989); alumina, Conley and Althoff (1971), Conley (1996), Halter, (1999), Jodin et al., (2005), Morel et al., (2006) ;titanium oxide, Kallay and Babic (1986); iron oxides, Hayes et al., (1991), Preoanin and Kallay, (1998); clay, Tournassat et al., (2004) iron and silica mixe oxides, Mustafa et al., (2002) .

In titration methodology, the uptake of acid or base by a suspension is measured and compared with the uptake of acid or base by a reference solution of liquid volume equivalent to that in the suspension. The difference between the amounts of titrant necessary to produce the same pH value in the suspension and the reference solution is attributed to adsorption or desorption of protons onto the solid surface. In the course of the titration, the amount of this relative adsorption by the solid is obtained as a function of the dispersion pH. By titrating the suspension at various ionic strengths of background electrolyte, one can establish the role of that electrolyte in surface–charge development. If there is a single pH value at which the amount of proton adsorption or desorption is the same for all ionic strengths of the background electrolyte, then it is likely that the electrolyte used is indifferent (i.e., does not participant in the interfacial chemistry of the solid). At this particular pH value, since the concentration of background electrolyte has no influence on the relative adsorption, the net proton adsorption must be zero. Accordingly, this pH value is known as the point of zero charge (pzc).

For each titration experiment, the relative adsorption of proton or hydroxyl ions (reported as the negative adsorption of protons in the figures to follow) by the solid can be determined as a function of the dispersion pH. If the relative ion-adsorption curves for different concentrations of background electrolyte are plotted, the pzc can be found by identifying a common intersection point (cip) in the adsorption curves. Absolute surface charge for the solids can be determined by offsetting the relative ion–adsorption data by the magnitude of the relative adsorption at the cip (thereby specifying the known absolute adsorption at the cip to be zero) and multiplying the result by the elementary charge per ion. In conjunction with knowledge of the total surface area of solids present in the suspension, surface–charge density can readily be determined as a function of dispersion pH.

For an oxide-water system, protons adsorbing to or desorbing from the surface impart charges on the surface through such reactions as (Dzombak and Morel, 1990):

$$S-O^{-}+H^{+}\rightarrow S-OH^{0} \qquad K_1 \qquad (5.1)$$

$$S-OH^{0}+H^{+}\rightarrow S-OH_2^{+} \qquad K_2 \qquad (5.2)$$

K_1 and K_2, are equilibrium acidity constants. As reactions indicate, addition of acid to oxide suspension procedures an excess of protons at the surface (positive charge) and addition of base causes a proton deficit (negative charge).

$$K_1 = \frac{\{SO^{-}\}[H^{+}]}{\{SOH\}} \qquad (5.3)$$

$$K_2 = \frac{\{SOH\}[H^{+}]}{\{SOH_2^{+}\}} \qquad (5.4)$$

where {} denotes the concentration of surface species in moles per kilogram of absorbing solid and [] denotes the concentrations of solutes as moles (M). Surface charge density and surface potential values for the oxides powders are determined by the well known method potentiometric titrations. For the oxides

$$C_A - C_B + [OH^{-}] - [H^{+}] = [SOH_2^{+}] - [SO^{-}] \qquad (5.5)$$

C_A and C_B are the concentrations of acid and base, respectively, added per liter. The pH-added acid base concentration diagram is given in Figure 5.2.a. This data are taken from potentiometric titration experiments.

The mean surface charge (Q) (i.e., the portion of the charge due to OH$^-$ or H^+) can be calculated as a function of pH from the difference between total added base or acid and the equilibrium OH$^-$ or H^+ ion concentration for a given quantity a (kg/ liter) of oxide used, as shown in Figure 5.2.b:

$$\frac{C_A - C_B + [OH^-] - [H^+]}{a} = \{SOH_2^+\} - \{SO^-\} = Q \qquad (5.6)$$

If the specific surface area S (m^2/kg) of oxide used is known, the surface charge can be calculated, as shown in Figure 5.2:

$$\sigma = QF / S \qquad (5.7)$$

where F is the Faraday constant (96485 C/mol).

Surface charge density(σ) is related to the potential at the surface(ψ).

$$\sigma = (8RT\varepsilon\varepsilon_0 I)^{1/2} \sinh(\frac{zF\psi}{2RT}) \qquad (5.8)$$

where R molar gas constant (8.314 J /(mol.K)), T the absolute temperature (K), ε the dielectric constant of water (ε = 78.5 unit at 25° C), ε_0 the permittivity of free space (8.854 x 10^{-12} C/ V. m or 8.854 x 10^{-12} C^2/ J. m), I molar electrolyte concentration [M].

Evaluation of surface charge of a hydrous oxide (α-FeOOH) from an experimental data was shown in Figure 5.2, which were calculated by Stumm and Morgan (1996). In titrating a suspension of α-FeOOH (6 g/l, 120 m^2/g, 2 10^{-4} mol/g), surface functional group (≡FeOHTOT), in an inert electrolyte 10^{-1} M NaClO4 with NaOH or HCl ; CB and CA is the concentration of base and acid respectively added per liter.For any point of titration curve equation 5.9 can be written

$$C_A - C_B + [OH^-] - [H^+] = [FeOH_2^+] - [FeO^-] \qquad (5.9)$$

and also mean surface charge (Q) can be calculated by equation 5.10.

$$\frac{C_A - C_B + [OH^-] - [H^+]}{a} = \{FeOH_2^+\} - \{FeO^-\} = Q \qquad (5.10)$$

pH versus Q graph was shown in Figure 5.2-b.

If specific surface area (m^2/g) of the iron oxide used is known, surface charge density (σ) were easily calculated by Equation 5.7. Surface charge density versus pH graph was given in Figure 5.3.

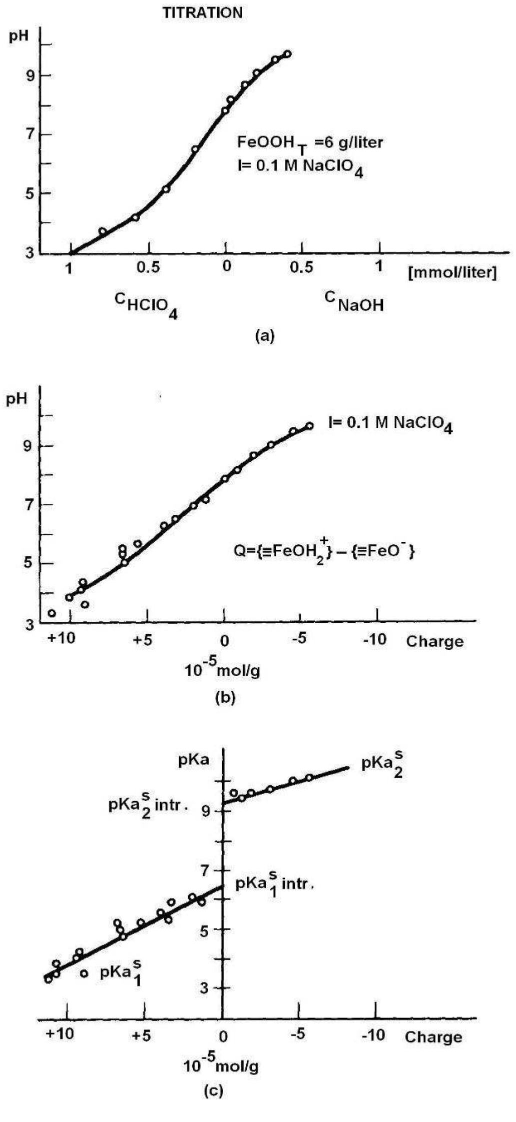

Figure 5.2. Titration of a suspension of a-FeOOH (goethite) in absence of specifically adsorbable ions. a) Acidimetric-alkalimetric titration in the presence of an inert electrolyte b) Charge calculated from the titration curve (charge balance) c) Microscopic acidity constants calculated from a) and b) Extrapolation to charge zero gives intrinsic pK_1 and pK_2 (Source: Stumm and Morgan, 1996)

Surface acidity equilibrium constants are also calculated, as shown in Figure 5.2.c.;

$$K_1 = \frac{(\{total\ SOH\} - Q)[H^+]}{Q}; \qquad K_2 = \frac{(Q)\,[H^+]}{(\{total\ SOH\} - Q)} \tag{5.11}$$

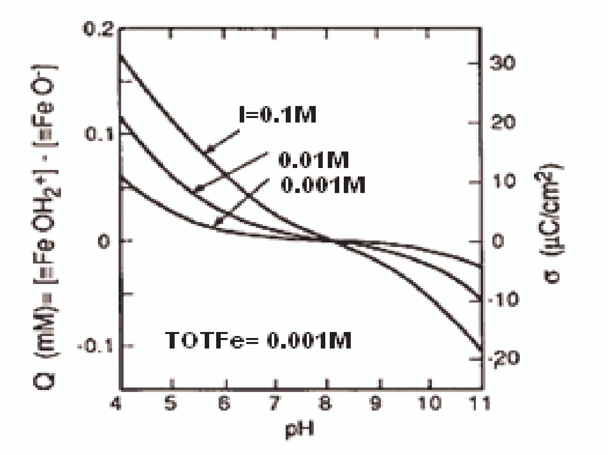

Figure 5.3. Surface charge as a function of pH and ionic strength (1:1 electrolyte) for a 90-mg/L (TOTFe = 10^{-3} M) suspension of hydrous ferric oxide.

If surface acidity equilibrium constants are known, the surface complexation of the system can be calculated according to main species of oxide system. Modeling of surface potential distribution for hydrated iron oxide was investigated by Polat et al. (2007) (Figure 5.4).

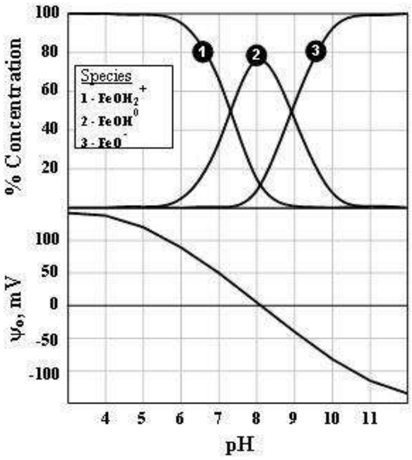

Figure 5.4. Distribution of surface species as a function of pH on hydrous iron oxide top graph with the resulting surface potential (bottom graphs) (Total surface $Fe(OH)_{3(s)}$ concentration is 2×10^{-4} M; Specific surface area of $Fe(OH)_{3(s)}$ is 600 m^2/g;Electrical double layer model employed is Diffuse EDL) (Source: Polat et al., 2007).

CHAPTER 6

EXPERIMENTAL AND COMPUTATIONAL METHODS

The objective of the present work is to assess the applicability of atomic force microscopy (AFM) to surface charge mapping, i.e., the detection of different charged regions on oxide surfaces. For this purpose, the interaction force between silica or alumina surfaces and the chemically inert tip will be measured at several pre-determined locations on the surface as a function of tip-surface distance. From such force curves, we will attempt to isolate the electrostatic component of the overall interaction force using relevant theories under well-defined experimental, material and solution conditions. Experimental conditions refer to best approach speed, optimal distance for the force analysis, etc, material conditions refer to the type of surface used, solution conditions refer to the pH, electrolyte strength, temperature etc.

Silica and alumina surfaces were used as the model systems since they have rather well-known charging characteristics and their surface charge can simply be controlled by regulating pH. The tip employed for probing these surfaces in this work was a commercial Si_3N_4 tip. However, as part of an on-going TUBITAK project the work will be extended to custom-made, specially-tailored tips (such as a tips conditioned with adsorbed layers of known charges, tips made up of a well-defined spherical solids or tips from well-defined crystals, etc.).

Different characterization methods were applied to the material used in the experimental study in order to be able to correlate the results obtained from this work with those determined from more classical and well-known methods. An example is determining the overall surface charge (not the distribution of charge) on oxide surfaces by colloidal titration using powders of these oxides. Zeta potential measurements are another one of such characterization routes. In addition, the XRD patterns of the surfaces to determine the crystal size and crystal structure of the solids were obtained along with the SEM analyses to determine the morphology of the surfaces. For the identification of the chemical species constituting the first atomic layer as well as the chemical state of the surface atoms Fourier transform infrared (FTIR) spectrometry was used. In order to assist these characterization procedures, some secondary characterization work had to be carried out to determine the surface areas of the powder using N_2 adsorption (Brunauer-Emmett-Teller; BET surface area) and their particle size distributions employing Sedigraph and Zetasizer.

6.1. Experimental

6.1.1. Materials (Powders, Substrates and Tips Employed)

The purpose of this study was to measure the interactive forces between silica (quartz surface) and alumina (sapphire surface) substrates and silicon nitride (Si_3N_4) tips. However prior to obtaining the interaction forces, a detailed characterization study was carried out with various silica and alumina powders and also with powdered glass using such techniques as XRD, SEM, BET, FTIR, Zeta Potential and potentiometric titration. Following powder characterization both the actual substrate (silica and alumina) and the silicon nitride tip were characterized using XRF, SEM and AFM.

The powders used in the characterization work were tabulated in Table 6.1.

Table 6.1. The powders used in the characterization work

Powders	**Code**	**Supplier**
Silica Powders	SO-01	Sigma-Aldrich 83.340
	SO-02	Natural quartz which was come from Dokuz Eylül University, Department of Mining Engineering
	SO-03	Admatech -Admafine SO-E6
Silica Nitride	SN	Sigma-Aldrich 24862-2
Alumina Powders	AO-01	Sumitoma Co. AKP 50
	AO-02	Alcoa company CT 3000 SG
	AO-03	Admatech -Admafine AO-802
Glass		Powder glass, grained glass substrate to get powder form

The substrates used in the characterization work which subsequently employed in the force measurement were,

i) Silica substrate: A planar quartz (0001) (1x1 cm) from MTI, CA, USA
ii) Sapphire substrate: A planar α-Al_2O_3 (0001) (1x1 cm) from MTI,CA, USA
iii) Glass substrate: A glass coverslip (1x1mm)

The tip used in the force measurements was Si3N4 tip from Veeco probes (Veeco, ORC series) consisting of rectangular silicon nitrite cantilevers with integrated pyramidal tips.

Three types of silica (two of them quartz form) and alumina, and also one silicon nitride powders were used in this study. One of the quartz powder used in this study, commercially labeled 83340 were supplied by Sigma-Aldrich. The quartz powder are prum ($\geq$ 95) and according to manufacturer have a particle size > 230 mesh with average density 2.6 g/mL at 25 ºC. This quartz powder labeled SO-01 for our experiment. The other quartz powder (SO-02) was taken from Dokuz Eylül University, Department of Mining Engineering. SO-02 was grained form of quartz rock. Before experiment, SO-02 powder was also grained. The spherical silica particles (SO-03) were used in this study. The spherical silica is commercially names SO-E6 was supplied Admataech, Japan. The silica particles are high purity (min 99.8%) and according to manufacturer have median size, d_{50}.2.2 μm with average density 2.2 g/cm^3 and surface area of 1.7 m^2/g.

Silicon nitride powder is a product of Sigma-Aldrich, commercial code is 248622. This powder is predominantly β-phase and particle size is around 325 mesh with average density 3.44 g/ml at 25 ºC.

High purity α-alumina powder (99.995%) is AKP 50, the product of Sumitomo Chemical Company Ltd., Japan. Alumina powders mean size between 0.1 and 0.3 μm. The specific surface area is 10.9 m^2/g and the density 3.9 g/cm^3. This powder labeled AO-01 for our experiment. The alumina powder was grade CT 3000 SG (Alcoa Chemie GmbH, Ludwigshafen, Germany) being a fine pure α-alumina with average particle size (d_{50}) of 0.5 μm and BET specific area of 6–8 m^2/g , density 3.9 g/cm^3. The spherical alumina particles(AO-03) used in this study, commercially named AO-802, were purchased from Admatech Japan. The α-phase alumina nanoparticle are of high purity (99.9%) and according to the manufacturer have a median size, d_{50}, of 0.6 μm, with an average density of 3.65 g cm^{-3} and surface area of 6.4 m^2 g^{-1}.

However, it became apparent that the as-received materials had interfacial chemistries that varied between samples, presumably because of uncontrolled surface contamination during storage, handling or manufacturing. This variability problem was alleviated by adsorption of a standard pretreatment procedure: samples of the as-received powders were stirred 1 hour with 0.1M HCl, then washed with ultra pure water then stirred 1 hour again with 0.1M HCl then washed with HCl and washed 3 times with ultra pure water, then put powder into the ultra pure water, left one night, then washed again, this washing treatment followed by repeated cycles of centrifugation and redispersion of the wet cake a in the acidified electrolyte and dried in oven at 40°C.

A glass coverslip (1mmx1mmx0.5 mm) were used as substrate for AFM. Some of the glass coverslip was grained and made ready as powder form to use some measurements. Silicon nitride probes, which is the product of Veeco (NPS series, consisting of triangular silicon nitride cantilevers), were used for AFM experiments.

6.1.2. Characterization of Powders and Substrates

Various well known characterization techniques which were not directly related to force and charge determination was employed to characterize the powders substrates and tips employed in this works. These are; XRD, BET Surfaca Area, SEM, FTIR, AFM, Particle Size Distribution.

6.1.2.1. X-ray Diffraction (XRD)

X-ray diffraction techniques are a family of non-destructive analytical techniques which reveal information about the crystallographic structure, chemical composition, and physical properties of materials and thin films. These techniques are based on observing the scattered intensity of an X-ray beam hitting a sample as a function of incident and scattered angle, polarization, and wavelength or energy. X-ray diffraction patterns of the powders were investigated by *XRD Phlips X'Pert Pro.*

6.1.2.2. BET Surface Area

The surface area of the given oxides was determined by N_2 adsorption, according to the BET method. BET theory is a rule for the physical adsorption of gas molecules on a solid surface and serves as the basis for an important analysis technique for the measurement of the specific surface area of a material. In 1938, Stephen Brunauer, Paul Hugh Emmett, and Edward Teller published an article about the BET theory in a journal for the first time; “BET” consists of the first initials of their family names. The surface area of the particles were measured by *Micromeritics Gemini V.*

6.1.2.3. Particle Size Distribution

The particle size distribution (PSD) of a powder, or granular material, or particles dispersed in fluid, is a list of values or a mathematical function that defines the relative amounts of particles present, sorted according to size. There are many techniques to measure particle size distribution. In our experiments we have used two types of measurement techniques one of them Sedimentation techniques the other is Laser diffraction methods.

Sedimentation techniques are based upon study of the terminal velocity acquired by particles suspended in a viscous liquid typical apparatus disperses the sample in liquid, and then measures the optical density of successive layers using visible light or X-rays.

Laser diffraction methods depend upon analysis of the "halo" of diffracted light produced when a laser beam passes through a dispersion of particles in air or in a liquid. The angle of diffraction increases as particle size decreases. Particle size analysis was investigated by Sedigraph 5100 Particle size analyzer and Malvern Mastersizer.

6.1.2.4 SEM Micrograph

The scanning electron microscope (SEM) is a type of electron microscope that images the sample surface by scanning it with a high-energy beam of electrons in a raster scan pattern. The electrons interact with the atoms that make up the sample producing signals that contain information about the sample's surface topography. SEM Micrograph has been taken by Philips XL 30 SFEG.

6.1.2.5. FTIR Analysis

Fourier transform infrared (FTIR) spectroscopy is a measurement technique for collecting infrared spectra. Instead of recording the amount of energy absorbed when the frequency of the infra-red light is varied (monochromator), the IR light is guided through an interferometer. After passing through the sample, the measured signal is the interferogram. Performing a Fourier transform on this signal data results in a spectrum identical to that from conventional (dispersive) infrared spectroscopy.

The FTIR spectra of the powders were obtained by Shimadzu FTIR spectrophotometer (8400S). KBr was used in the sample preparation for the analysis. The powders were kept at 40 °C, in vacuum oven overnight. The pellets for samples were prepared by following procedure; Firstly powder was mixed with KBr in certain amounts (3mg samples in 150 mg KBr), then ground in an agate mortar and pressed.

Since α -alumina and silica have hydrated strongly, FTIR-DRIFT (Digilab Excalibur FTIR). DRIFT studies were carried out with the AO-03, SO-03 and SN samples. In these tests, 5 g α-alumina powder was dispersed in 100 ml of a solution of 10^{-3} M KCl at three different pH values, 2, 6 and 10. The dispersion was kept in a shaker for 24 h, than vaporized water under oven at 40 °C to The DRIFT spectra of all powders were recorded at ambient air and $5.3x10^{-3}$ Pa of pressure using a vacuum chamber with a vacuum system equipped with a turbo molecular pump and sorption pump. The samples were also heated in situ in glass windows under vacuum condition up to 40 °C.

6.1.2.6. Surface Topography by AFM

Surface topography and force measurements were performed with multimode AFM, Digital Instrument, MMSPM-NanoScope IV, Santa Barbara.

6.1.2.7. XRF Measurement

X-ray fluorescence (XRF) is the emission of characteristic "secondary" (or fluorescent) X-rays from a material that has been excited by bombarding with high-energy X-rays or gamma rays. The phenomenon is widely used for elemental analysis and chemical analysis, particularly in the investigation of metals, glass, ceramics and building materials, and for research in geochemistry, forensic science and archaeology. Glass substrate was investigated by using XRF (METEC-Spektro IQ II).

6.1.3. Characterization of Powders and Substrates Relevant to Charge and Force Measurements

In this part, powders were characterized using electrophoretic and potentiometric titration methods in order to obtain information on the charging behavior of the materials employed in this work.

6.1.3.1. Electrokinetic Potential Measurements

Zeta potential is measured by applying an electric field across the dispersion. Particles within the dispersion with a zeta potential will migrate toward the electrode of opposite charge with a velocity proportional to the magnitude of the zeta potential. This velocity is measured using the technique of laser Doppler anemometry. The frequency shift or phase shift of an incident laser beam caused by these moving particles is measured as the particle mobility, and this mobility is converted to the zeta potential by inputting the dispersant viscosity, and the application of the Smoluchowski or Huckel theories. These theories are approximations useful for most applications. Electrokinetic potential measurements were investigated by Malvern Zetasizer Nano-Zs in de-ionized water or in electrolyte solutions (Gebze Institute of Technology).

Zeta potential measurement with powdered glass was obtained in 10^{-3} M KCl solutions at a solid/liquid ratio of 0.1 g/L. For this experiment we have measured zeta potential by Zeta-Meter 3.0+.

6.1.3.2. Potentiometric Titration Experiments

Potentiometric titration is a technique similar to direct titration of a redox reaction. No indicator is used; instead the voltage across analyze, typically an electrolyte solution is measured. To do this, two electrodes are used, a neutral electrode and a standard reference electrode. The voltage is recorded at intervals as titrant is added. A graph of voltage against volume added can be drawn and the end point of the reaction is half way between the jumps in voltage. Potentiometric titration experiments have been performed by *KEM Automatic Potentiometric Titrator AT-510.*

Titration experiments were performed by first dispersing the pretreated powders in a pH 2 solution with 0.001M background electrolytes. These dispersions were titrated with base to pH 11. Both 0.1M HCl and 0.1M KOH were used as titrant.

6.1.4. Force Measurements

The method of measuring the interaction force acting between a Si_3N_4 tip and a smooth surface seems deceptively simple since the Atomic Force Microscope simply spits out an approach and retract curve for any measurement comprising of a voltage signal on the y-axis related to the cantilever bending (due to interaction force between the tip and the surface) and the relative distance between the tip and the surface. Carrying out such a force experiment and then determining the surface charge distribution of the surface from it have numerous severe pitfalls to be aware of and sidestepped for the procedure to be meaningful

- Cleaning/conditioning and preparing the tips and surfaces for the measurement (no surface contamination, irregularities and residues can be allowed on the interacting surfaces. The cleaning procedure used prior to each test consisted of several steps),
- achieving equilibrium conditions before and during the experiment (no changes can be allowed in solution composition, pH, temperature)
- properly carrying out the measurement (using the best approach speed not to create gradients close to the surfaces and not to develop a dynamic pressure force due to the amount of water to be displaced between the surfaces, “feeling” which curve is superfluous and which is real)
- converting the signal-relative distance curve to the actual force-actual distance curve (determining before hand the cantilever spring constant for each cantilever separately, establishing an effective and well-understood algorithm for the conversion process)
- determining the theory to be used and establishing the tools to use the theory (being aware of secondary effects such as steric, hydration, hydrophobic forces, a good understanding of the electrostatic theory of dispersed phases, knowing whether the surface are constant-charge, constant-potential or charge-regulated surfaces, developing a method for solving the Poisson-Boltzmann Equation for such analysis)

- comparing the force curve with the proper theory and isolating the surface charge distribution (knowing the Hamaker constant of the samples, running the test under solution conditions where the surfaces are clean of adsorbed layers or precipitates, determine the optimum distance for the force value which is close enough for a good signal but far enough not to be disturbed by surface irregularities)

are the main points to be considered. The details of how these points were addressed in this work will be outlined in the following sections.

6.1.4.1. Treatment of Surfaces

The properties of colloids can be dramatically influenced by the presence of quite small amounts of certain substances, especially surfactants, multivalent ions and polymeric material. In colloidal systems where the particle concentration is small (and in the extreme case of a single colloid probe) the available surface is very small, so even a little amount of a contaminant may be sufficient to coat the entire surface and completely alter the properties of the system. Surface cleanliness is a major issue when performing direct measurements of surface forces, and is also important when imaging. Exposure of any surface, but especially high energy surfaces like gold, mica, to atmospheric air can result in contamination from aliphatic compounds, water, dust, and debris. Lo et al. [1999] showed that even the packaging used for AFM cantilevers leaves traces of silicon contamination on the cantilevers. Surface conditions are of fundamental importance for the reproducibility of the measurement both in force and imaging experiments. It is therefore very important to perform thorough cleaning procedures before each experiment.

Substrate surfaces were cleaned for the AFM surface roughness and force measurements. The cleaning procedure was as follows:

- Ethanol rinse 3 times
- DI water rinse 3 times
- UV light exposure; 15 min
- The probe and the liquid cell were all subjected to UV Treatment for 10 min.

Before each test, they were washed with ethanol, water and experimental solution used copiously. The substrate and probe were placed in liquid cell 10 minutes before measurements.

6.1.4.2. Cantilever Calibration and Determinations of Spring Constant

For the conversion of the force signal from AFM to actual force data, the spring constant of the cantilever must be known. By far, the most reliable method for determination of the spring constant has been referred Sader method.

The Sader's method for calibrating the normal spring constant of rectangular AFM cantilevers involves measurement of the unloaded radial resonance frequency (ω_f) and quality factor(Q_f) of the fundamental flexural resonance peak for a cantilever beam immersed in fluid, typically air [Sader, 1998, Sader et al., 1999, Sader, 2002]. Provided the quality factor is much greater than unity, which is typically satisfied if the cantilever is immersed in air, the normal spring constant at the end-tip of the cantilever is given by:

$$k_n = 0.196\rho_f b^2 L Q_f \omega_f^2 \Gamma_i^f(\omega_f) \qquad (6.1)$$

where ρ_f is the density of the air, b and L are the width and length of the cantilever, respectively, and Γ_i^f is the imaginary component of the hydrodynamic function which is a function of Re number where:

$$Re = \frac{\rho_f \omega_f b^2}{4\mu_f} \qquad (6.2)$$

The change in the hydrodynamic function is given in Figure 6.1 in graphical format for quick reference. A more accurate analytical definition is provided in Sader et al., [1999].

$$k_n = 7.5246\rho_f\, b^2\, L\, Q_f\, \omega_f{}^2\, \Gamma_i^f \qquad (6.3)$$

In order to minimize error in force calculations, the cantilevers were singly tested for their dimensions, natural resonant frequency, ω_f,=61 kHz and the quality factor, Q_f =97, at room temperature (25 ^{o}C). The width and lengths of probes are measured as 55 µm (b) , 110 µm (L), respectively for the short probe which were used in force measurements. The density and viscosity of the air are taken ρ_f =1.18 kg/m^3, μ_f=1.86 10^{-5} kg/m.s. Thus, the Reynolds' number is calculated and the spring constant is calculated as 0.734 according to equation 6.3.

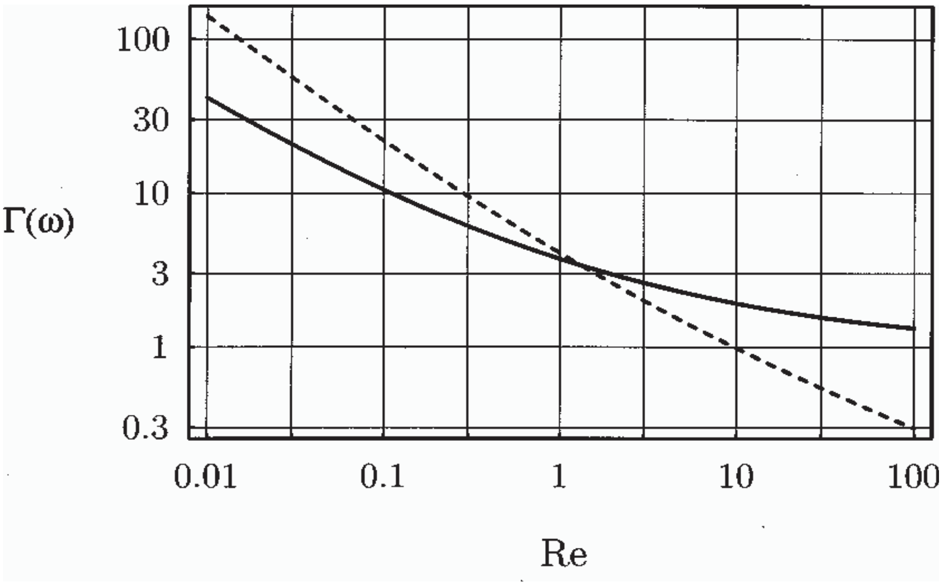

Figure 6.1. Hydrodynamic function $\Gamma(\omega)$ for a rectangular cantilever beam as a function of the Reynolds number. The dashed line is the real component Γ_r^f while the solid line is the imaginary component Γ_i^f [Sader et al., 1999].

6.1.4.3. Raw Force Measurements and Conversion of the deflection Signal-Piezo Translation Data to Interaction Force-Distance Curves

The interaction force between a silicon nitride cantilever tip and a silica, alumina or glass surface will be measured by a Nanoscope III atomic force microscope (Digital Instruments, Santa Barbara, CA) equipped with a fluid cell.

The force-distance measurements will perform to study attractive and repulsive forces on a tip as it approaches and retracts from the sample surface.

The force measurements were carried out at nine different points on a 1x1 μm section of glass surface. The same procedure was repeated on several different sections on the glass surface to check reproducibility. In the normal force measurements, the glass surface was approached and retracts 575 nm/s in all cases.

At the beginning of this study we have measured surface forces of oxides under ambient condition by AFM for obtaining the force-distance curves. Then oxides surface have been investigated under various electrolyte with standard Si_3N_4 tip by using AFM fluid cell. After these experiment results we can decide what kind of colloidal probe we can use in our systems, then we will make colloidal probe, then characterize and apply the surface force measurement of oxide surfaces under various electrolyte solutions.

An AFM force-distance curve is a plot of tip-sample interaction forces vs. tip-sample distance. In order to obtain such a plot, the sample (or the tip) is ramped along the vertical axis (Z axis) and the cantilever deflection **x** is acquired. The tip-sample force is given by Hooke's law: **F=k.x.**

The distance controlled during the measurement is not the actual tip-sample distance **h**, but the distance **D** between sample surface and the rest position of the cantilever. These two distances differ because of cantilever deflection **x** and because of the sample deformation **c** these four quantities are related as follows:

$$h = D - (x+c) \qquad (6.4)$$

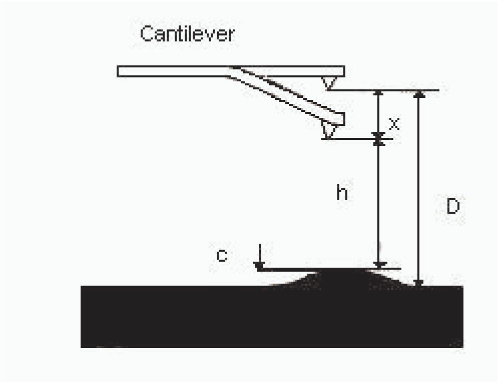

Figure 6.2. The tip-sample system. h is the actual tip-sample distance, whereas D is the distance between the sample and the cantilever rest position.

Since one does not know in advance the cantilever deflections and the sample deformations, the only distance that one can control is the distance D, i.e., the displacement of the piezo. Therefore, the raw curve obtained by AFM should be called "force-displacement curve" rather than "force-distance curve". This latter term should be employed only for curves in which the force is plotted versus the true tip-sample distance that has been previously calculated from raw data.

An AFM force-displacement curve does not reproduce tip-sample interactions, but is the result of two contributions: the tip-sample interaction F(D*)* and the elastic force of the cantilever. Such a result can be intuitively understood by means of the graphical construction shown in Fig. 6.3.

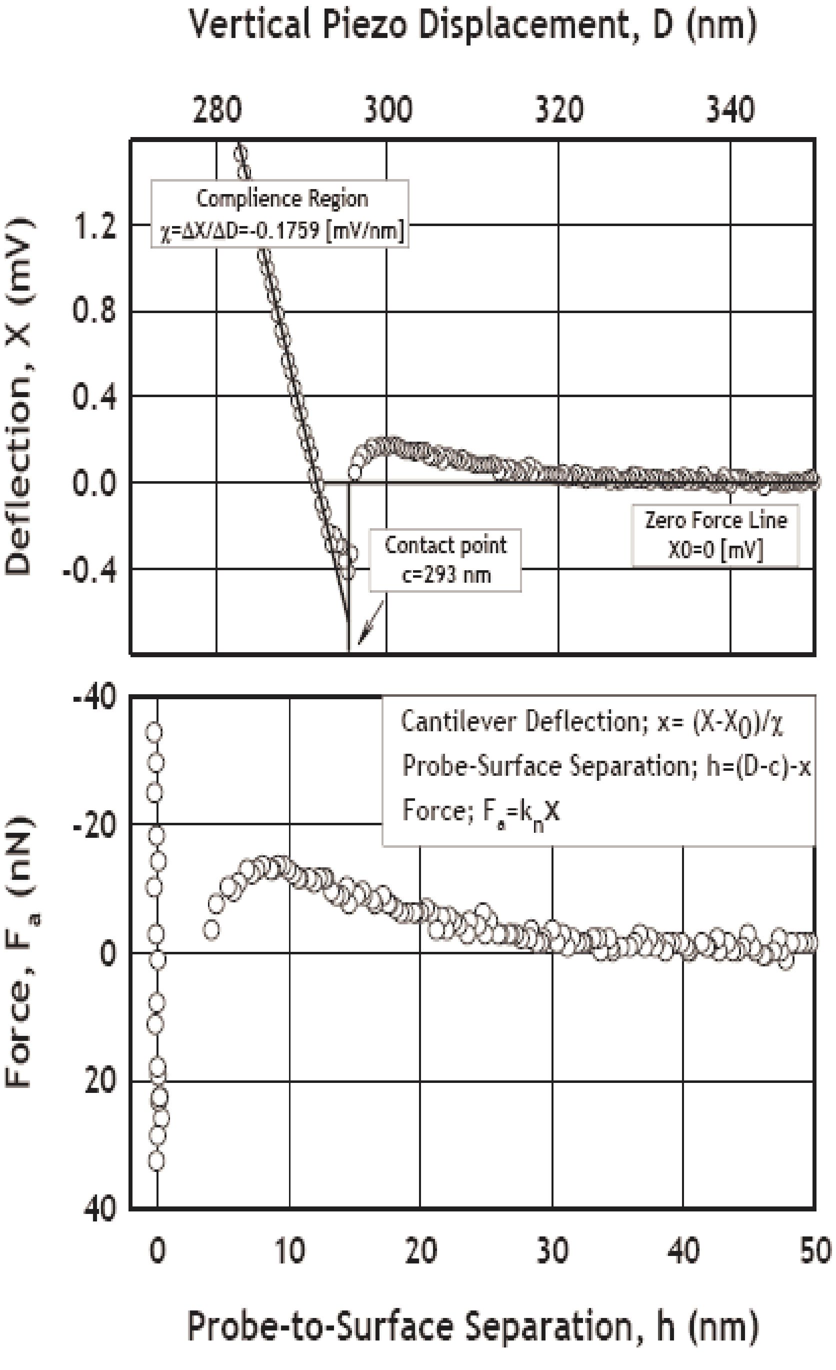

Figure. 6.3. An example raw force curve data

(Source: Polat et al., 2006)

6.2. Computational Method (Calculation of Theoretical Electrostatic Force Curve for Constant Potential and Constant Charged Surfaces of Arbitrary Charging)

Accurate Theoretical calculations of force curves for constant potential and constant charge surfaces are important in determining the surface charge or surface potential from the measured AFM force data. If one can accurately calculate the theoretical force curve for electrostatic interaction only them one can equate it to the measured force curve to estimate the surface charge at that point on the surface.

The theoretical force calculations were carried out based on the DLVO theory, assuming that the net force of interaction (Fnet) per unit area of the interacting plates was a sum of van der Waals and double-layer forces. van der Walls equation was obtained as explained in Chapter 2.1.1, Equation 2.8. The Hamaker constant for alumina-silicon nitride surfaces interacting in water was taken as $A_{Al\text{-}SN} = 2.817\times10^{-20}$ J, silica-silicon nitride surface was taken $A_{Si\text{-}SN}$=6.127 10-21 J, the calculated values reported in Polat and Polat [2000-a].

For calculating the electrostatic pressure force (F_{el}), a full analytical solution of the Poisson–Boltzmann equation was obtained as explained in Chapter 2.1.2 (see equations 2.29 and 2.30). The method of calculation the electrostatic pressure force is outlined in Table 6.2. Examples of MathCad sheet for this calculation for silicon nitride tip and silica and alumina substrate are presented Appendix B. This algorithm was applied to both constant surface potential and constant surface charge system for both alumina silicon nitride and silica silicon nitride surfaces. Detailed theory behind the computer program was given in Chapter 2. It can be seen that for given surface charges for both the probe and true surface, a theoretical electrostatic force curve can be obtained.

The computer programs which were written in Matcad were performed silicon nitride probe-silica/alumina substrate for constant surface potential/constant charge systems were given in Appendix B.

Table 6.2. Illustration of the use of analytical equations for an example double layer system assuming initial and constant surface potentials of $\psi_{1\infty} = 60\ mV$ and $\psi_{2\infty} = 10\ mV$.

a) Calculation of interplate distance *H* and electrostatic pressure *F*

i) Enter an arbitrary surface potential for Plate 1 and 2:

$\boldsymbol{\psi_{1\infty} = 60\ mV}$ and $\boldsymbol{\psi_{2\infty} = 10\ mV}$

ii) Calculate Y_{1i} and Y_{2i}

$\boldsymbol{Y_{1i} = 2.376\ ,\ Y_{2i} = 0.396}$

iii) Calculate S_{1i} and S_{2i} from Equation 5-a and 5-b

$\boldsymbol{S_{1i} = 2.976\ S_{2i} = 0.399}$

iv) Calculate ϕ from $\phi(S_2) = S_2^2 - 2\cosh Y_{2\infty}$

iv) Calculate *H* from $H = X_m + X_m^{'}$

$$X_m = \int_0^1 \frac{S_1}{\sqrt{u(S_1^2 u - \phi)^2 - 4u}}\,du \ \ ;\ X_m^{'} = \int_0^1 \frac{S_2}{\sqrt{u\,(S_2^2 u - \phi)^2 - 4u}}\,du$$

vi) Calculate F_e on *Plate 2* at *H*

$$F_e = cosh\ Y_{2\infty} - 1 - \frac{{S_2}^2}{2}$$

vii) Repeat steps ***i-vi*** for a range of S_2 values to obtain S_1, S_2 *and* F_e as a function of *H*.

viii) Insert Hamaker constant for material then calculated van der Walls Forces (F_{vdw}) for each H.

ix) Calculated electrostatic force for each H

x) Calculate F_{DLVO}

xi) Change force to Derjaguin approximation

After analytical solution of PB equation was performed, F_{DLVO} could easily be calculated by summation of van der Walls and electrostatic forces.

Since the real system is a flat surface (quartz or sapphire) interacting with a spherical particle (silicon nitride colloid probe). Hence the force measured has units of nanoNewtons. Since the above solution give the force per unit area for two plates, a transformation between the two is required. Derjaguin’s approach which was described in Section 2.1.3 can safely be employed to normalize the force calculations, moreover elaborate techniques are available [Bhattacharjee and Elimelech, 1997], [Bhattacharjee et al., 2000]. Separation distances shorter than 100 nm and colloid probe diameters of about 10 μm correspond to an h/2R value smaller than 0.01. This value is well within the range of Derjaguin’s approximation [Bhattacharjee and Elimelech, 1997]. Then, based on Derjaguin’s approximation, the actual force of interaction in units of newtons (Fa) is equal to Fnet.

CHAPTER 7

RESULTS AND DISCUSSION

The results of this study will be reported in three main sections: in the first results pertaining characterization of powders will be presented. Second section deals with measurements of surface charges on powders utilized. In the third section, the measured and theoretically calculated force–distance curves are compared and discussed. Finally, resulting calculations for obtaining the surface charge distribution maps on oxide is going to present.

7.1 Characterization of Powders

The characterization of powder form of metal oxides and silicon nitride is of great importance to understand the properties of the materials used in this work. Characterization work with these materials consisted of XRD, BET surface area, particle size distribution, SEM, FTIR, AFM and XRF measurements.

7.1.1 X–ray Diffraction of Powders

X–ray diffraction techniques belong to a family of non–destructive analytical techniques which reveal information about the crystallographic structure, and crystal size.

The X–ray diffraction patterns of SO-01 and SO-02 samples (the code was given in Table 6.1) are given in Figure 7.1 and Figure 7.2 respectively. The XRD pattern of quartz showed its typical peaks for its crystalline form. The pattern was similar to the standard XRD diffraction pattern of quartz as published by JCPDS– 11–697. The main peaks are located Quartz 26.6, 20.8, 70.1, 79.9. No other peaks were obtained.

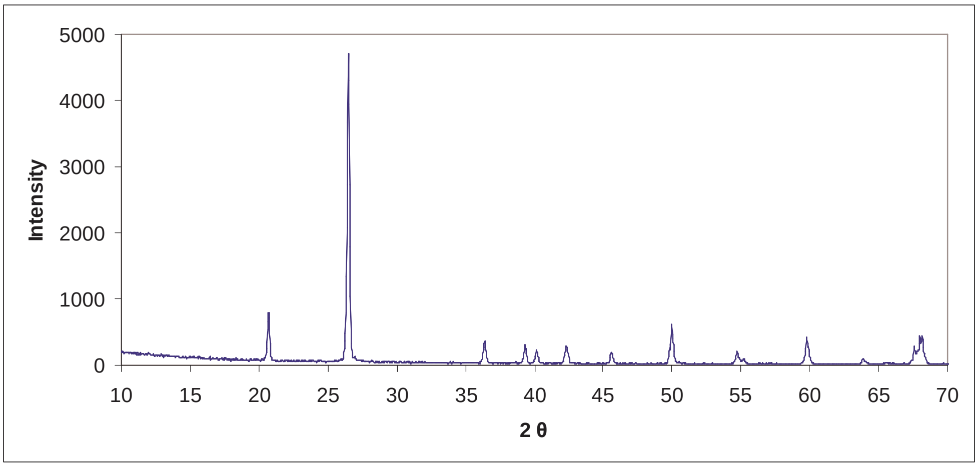

Figure 7.1. XRD patterns of SO-01 silica powder.

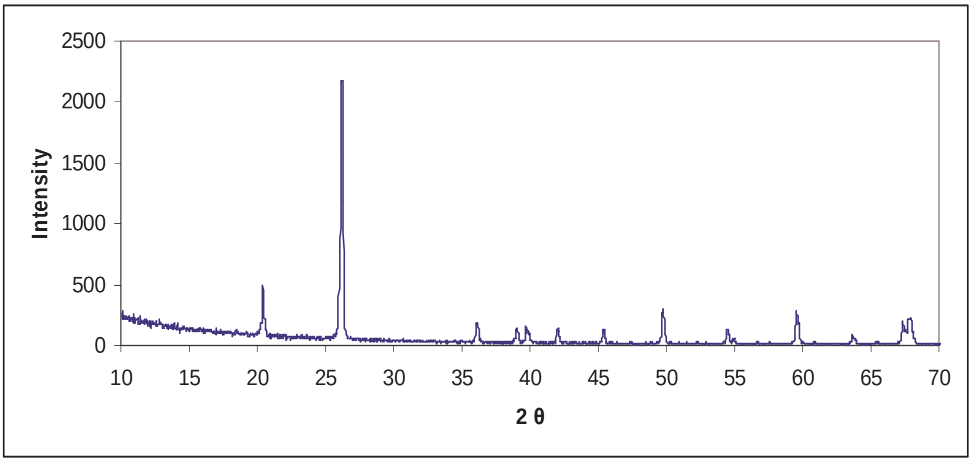

Figure 7.2. XRD patterns of SO-02 silica powder.

The X–ray diffraction pattern of silica powder presented in Figure 7.3. The X–ray pattern confirms amorphous silicon dioxide.

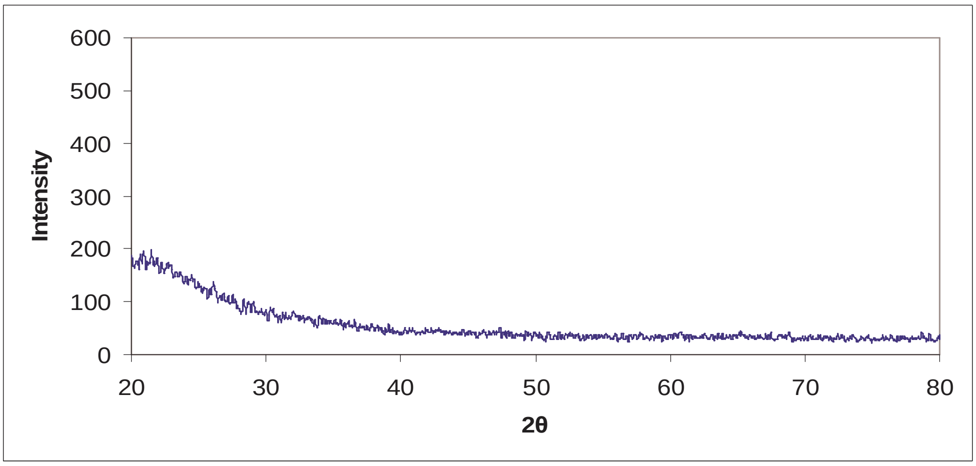

Figure 7.3. XRD patterns of SO-03 silica powder.

The XRD pattern of SN powder was presented in Figure 7.4. Phase identification was achieved by matching the measured patterns against those from the JCPDS database 410360 for α– Si_3N_4, and 331160 for β– Si_3N_4. Commercial α–type or β–type Si_3N_4 powder usually contains a few percent of each phase. The Si_3N_4 powder showed mainly the principal diffraction peaks of β–type Si_3N_4 with some α–type diffraction peaks. Hence, it was treated as β– Si_3N_4 sample.

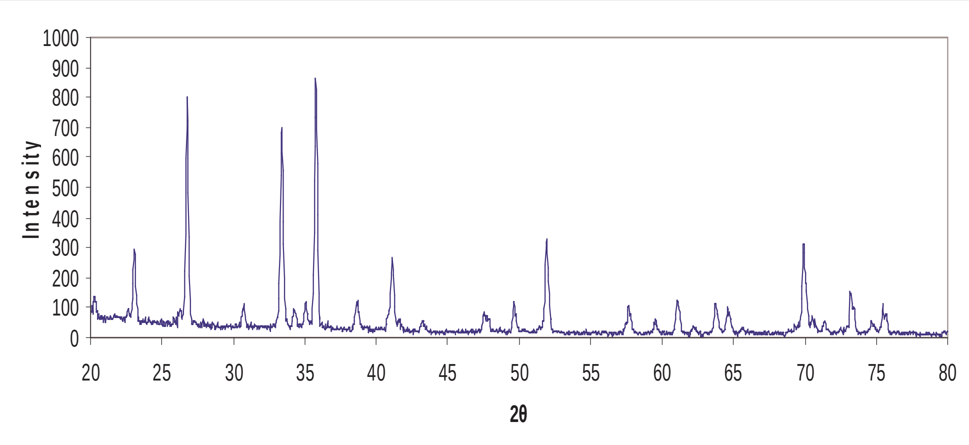

Figure 7.4. XRD patterns of SN silicon nitride powder.

The XRD patterns of α–alumina are given in Figure 7.5 and Figure 7.6 for AO-01 and AO-02 powders (the code was given in Table 6.1), respectively. They show the same diffraction pattern with that observed with standard α–alumina powders given by JCPDS was 11–0661. The main diffraction peaks were located at 27.71, 34.82, 37.77, 43.10, 72.27, 77.39, 66.37, 68.13, and 77.01 of 2θ. The crystalline size of the powder was calculated as 70 nm at 24.38 of 2θ by Sherer equation.

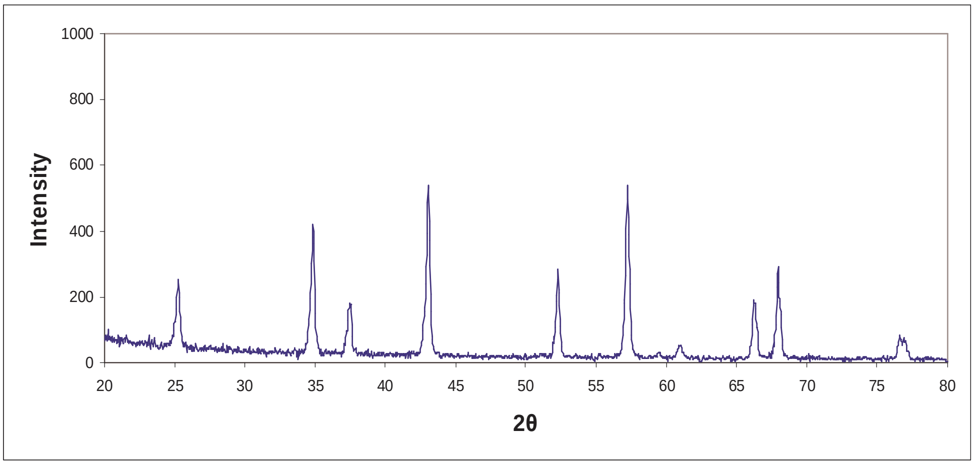

Figure 7.5. XRD patterns of AO–01 alumina powder.

Table 7.1 gives the crystallographic direction data for alumina (Santra et al., 2002).

Table 7.1. Crystallographic Direction versus 2θ vales of alumina

Crystallographic Direction	**2θ**
(012)	27
(104)	37
(110)	38
(113)	43
(024)	72
(116)	77
(214)	66
(300)	68
(1010)	77

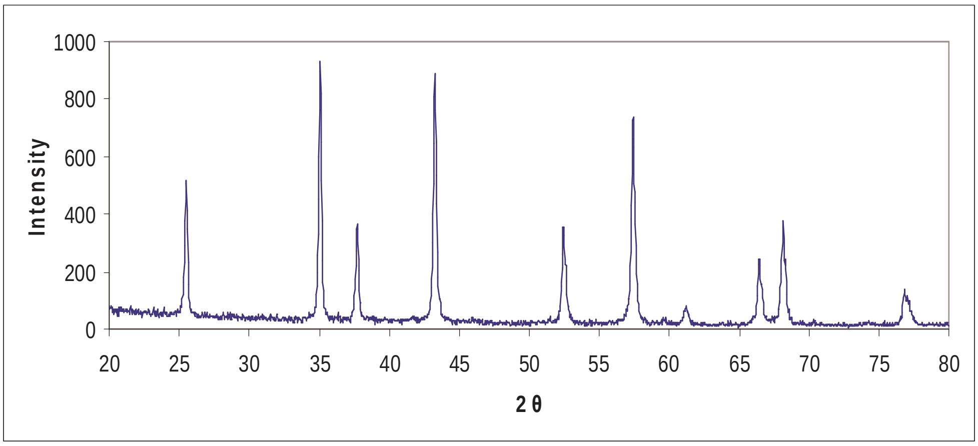

Figure 7.6. XRD patterns of alumina AO-02 powder**.**

The x-ray diffraction pattern of sample AO-O3 (the code was given in Table 6.1) is given in Figure 7.7. Powder showed mixed phases of alpha and gamma alumina.

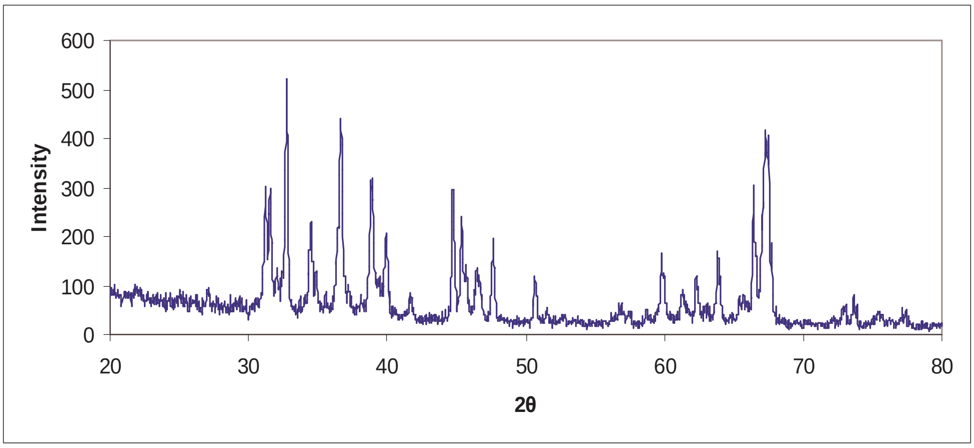

Figure 7.7. XRD patterns of alumina AO-03 powder.

7.1.2. BET Surface Area of the Powders

The surface areas of the oxide samples were determined by N_2 adsorption, using the BET method for the alumina and silicon nitride powders BET theory is based on the physical adsorption of gas molecules on solid surfaces and serves as the basis for the measurement of the specific surface area. Measurement of surface area of the powders was necessary to determine the surface area of powders for potentiometric titration experiments.

The quartz samples could not be analyzed by N_2 adsorption due to very low surface area. In the literature, the BET for the same quartz has been reported as 1 m^2/g (Kosmulski, 2009). Surface area values of the oxide samples are tabulated in Table 7.2.

Table 7.2 Surface area of the quartz, alumina and silicon nitride powders

Material	Surface Area (m^2/g)
SO-01	1*
SO-02	1*
SO-03	3.17
SN	1.26
AO-01	12.3
AO-02	3.94
AO-03	7.34

*** From Literature (Kosmulski, 2009)**

7.1.3. Particle Size Distribution of Powders

Particle size measurements are carried out using dynamic light scattering (DLS) (Malvern Mastersizer) and some were repeated by sedimentation (Sedigraph 5100). The median particle sizes of all samples were given in Table 7.3. The particle size distribution of the SO-01 was given in Figure 7.8. According to Sedimentation method, about 90% w of the quartz particles were below 50 μm and 50% w of the particles were below 27 μm. The D_{50} (median) particle size of the quartz was 25.76 μm. According to dynamic light scattering (DLS) technique about 90% of the quartz particles were below 77 µm and 50% of the powder was below 32 µm. Both of the particle size distribution techniques give nearly same particle size distribution for SO-01 sample.

Table 7.3. Particle sizes of the quartz, alumina and silicon nitride powder

Material	**Particle Size (µm)** **Median (by Laser Diffraction Techniques)**
SO-01	32.21
SO-02	26.28
SO-03	1.95
SN	2.60
AO-01	0.20
AO-02	0.75
AO-03	0.78

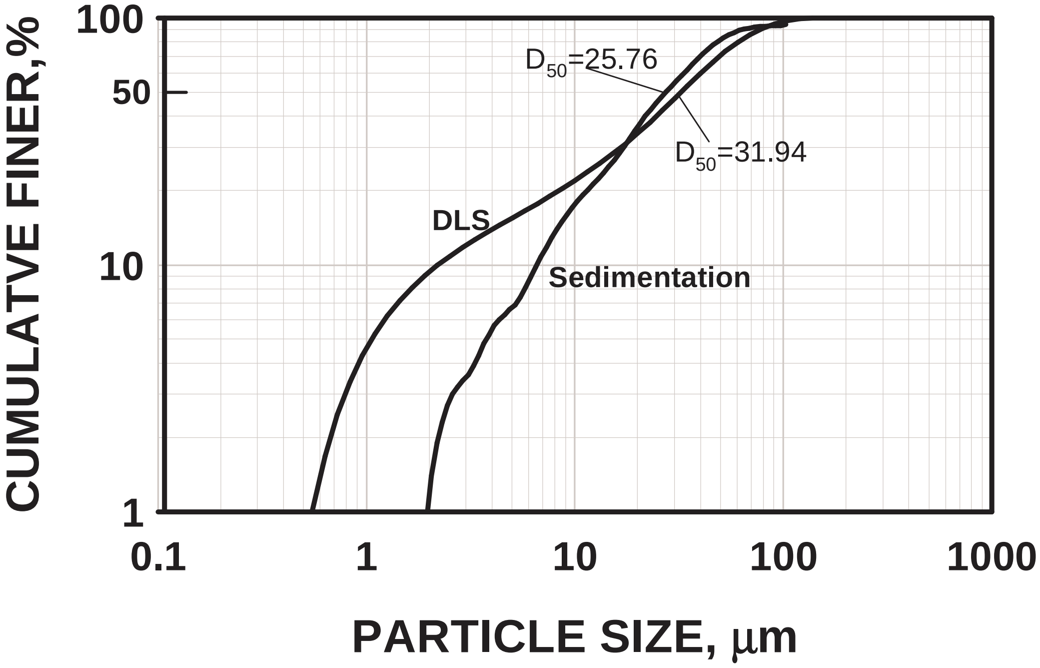

Figure 7.8. The particle size distribution of SO-01 quartz powder by sedimentation and DLS techniques.

The particle size distribution of the SO-02 was given in Figure 7.9. For this powder we could not obtain the size distribution by Sedimentation because we haven't had enough powder for this experiment prepared sample amount was too low. According to size measurement by DLS, about 90% of the quartz particles were below 96.3 μm and 50% of the particles were below 26.3 μm. Particle size ranges of the natural quartz were measured between 10–100 μm.

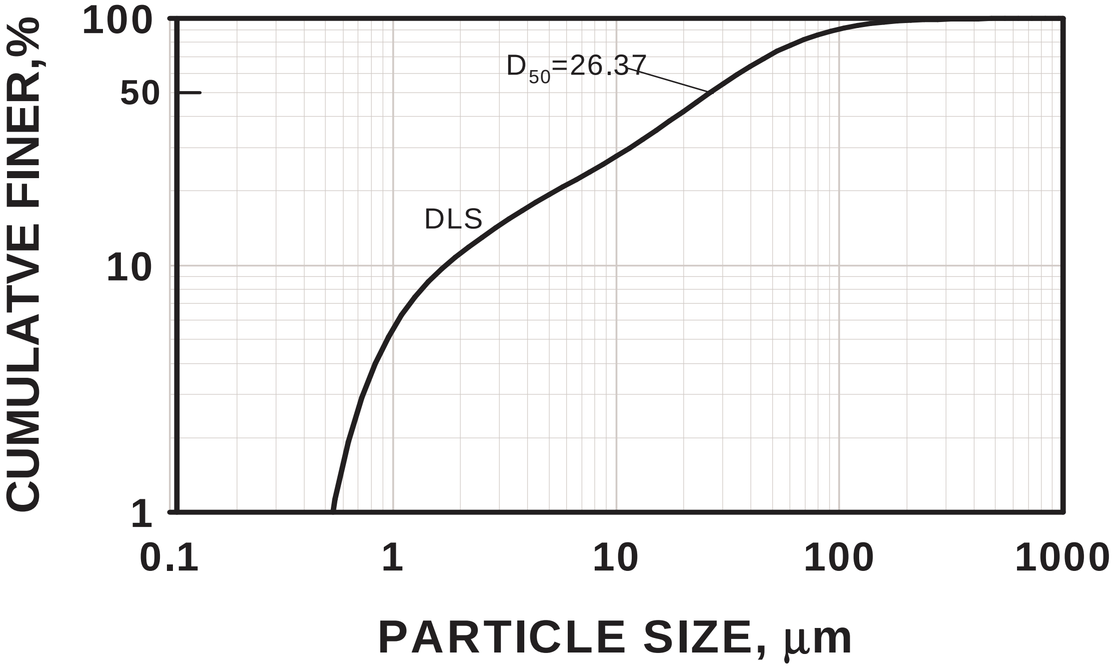

Figure 7.9. The particle size distribution of SO-02 quartz powder by DLS technique**.**

The particle size distribution of the SO-03 was given in Figure 7.10. 97% of the particles were below 10 μm by Sedimentation. About 90% of the silica particles were below 4.9 μm and 50% of the particles were below 1.9 μm. Particle size ranges of the silica were measured between 0.6–27 μm. But the main particle size distribution is in between 0.6–8 μm by DLS.

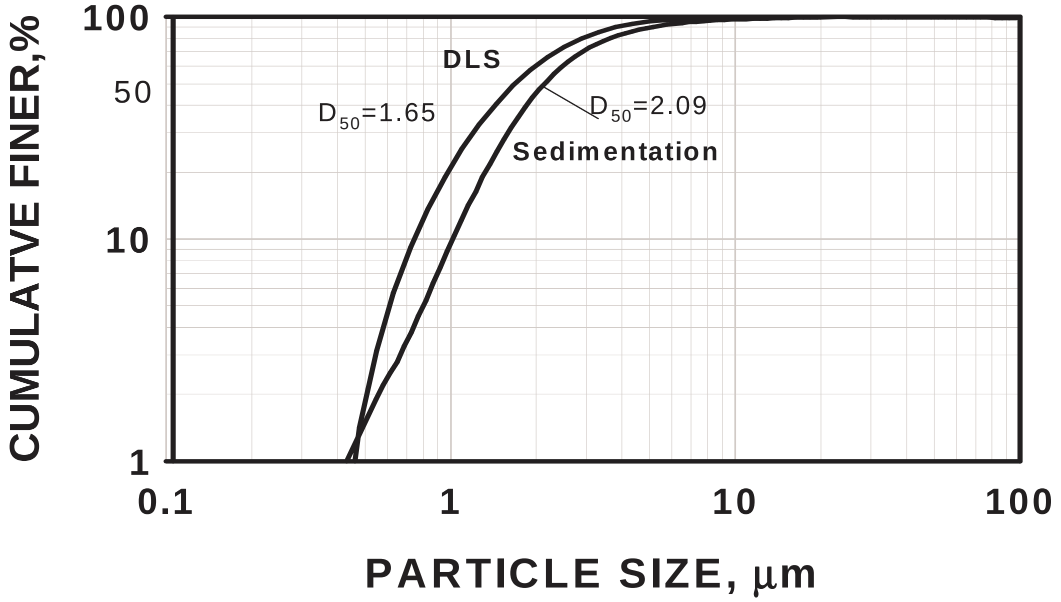

Figure 7.10. The particle size distribution of SO-03 quartz powder by sedimentation and DLS techniques.

The particle size distribution of SN is given Figure 7.11, by Sedimentation about 97% of the silicon nitride particles were below 30 µm and an important part of the particles (86% wt) were below 20 µm The D_{50} (median) particle size of the silicon nitride was 5.02 µm According to DLS, 90% w of the quartz particles were below 20.3 µm and 50% of the particles were below 2.6 µm Particle size ranges of the silicon nitride were measured between 0.28– 47 µm.

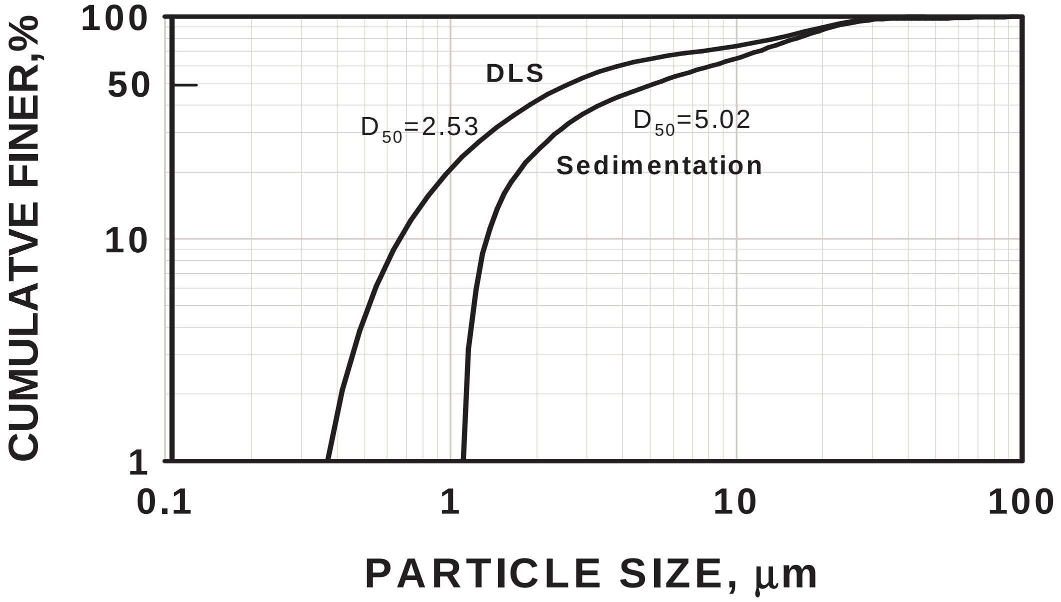

Figure 7.11. The particle size distribution of SN silicon nitride powder by sedimentation and DLS techniques.

The particle size distribution of AO-01, which is measured by sedimentation, is given Figure 7.12. About 94% w of the alumina particles were below 1 µm and 90% wt of the particles were below 0.7 µm. The D_{50} (median) particle size of the alumina was 0.18 µm. The particle size distribution of AO-01, which is measured by DLS,. 90% w of the quartz particles were 0.3 µm and 50% of the particles were below 0.2 µm. Particle size ranges of the alumina were measured between 0.1–10 µm, but the main distribution is in between 0.1–1 µm range. According to literature Particle size distribution of the AO-01 is 100–300 nanometers (Kosmulski, 2009). Particle size distribution of AO-01 was good agreement with literature data.

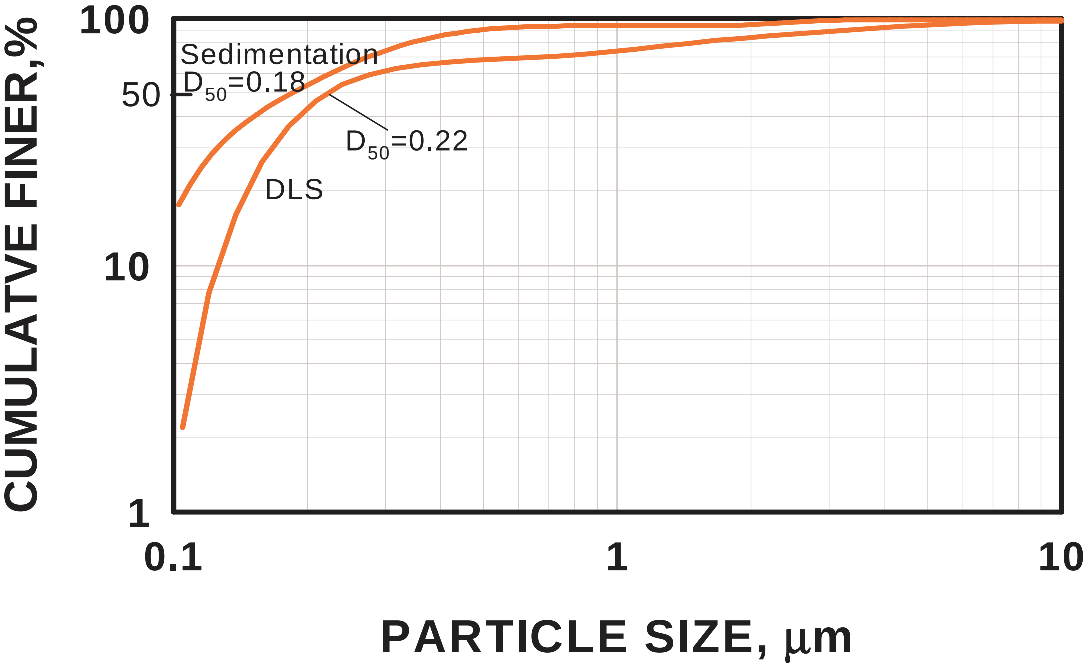

Figure 7.12. The particle size distribution of AO-01 alumina powder by Sedimentation and DLS techniques.

The particle size distribution of AO-02, which is measured by DLS, is given Figure 7.13. 90% of the quartz particles were 2.3 µm and 50% of the particles were below 0.7 µm. Particle size ranges of the alumina were measured between 0.1–10 µm.

The particle size distributions of the AO-03 were given in Figure 7.14. About 90% of the quartz particles were below 2 µm for both sedimentation and DLS methods. 50% of the particles were measured below 0.5 µm according to both measurements. Particle size ranges of the alumina were measured between 0.1–10 µm.

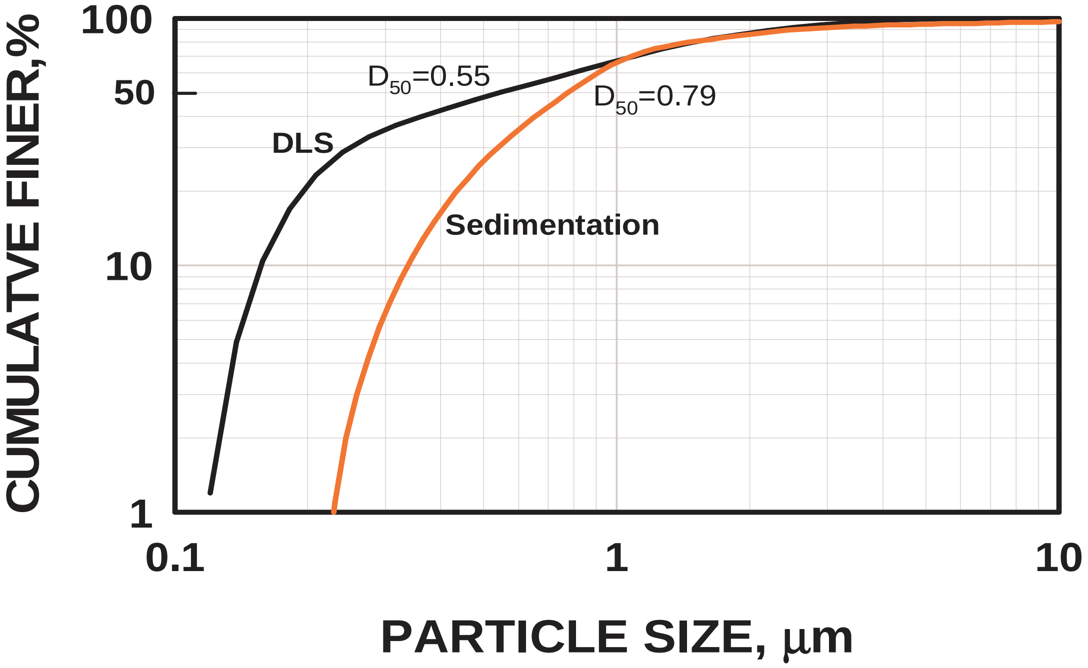

Figure 7.13. The particle size distribution of AO-02 alumina powder by Sedimentation and DLS techniques.

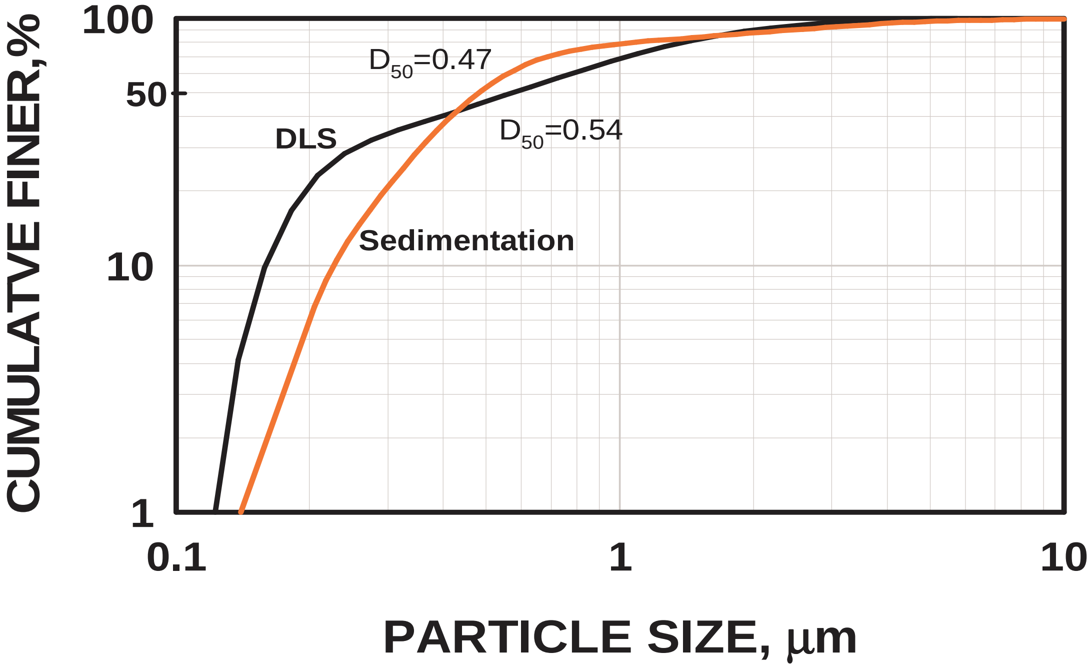

Figure 7.14. The particle size distribution of AO-03 alumina powder by Sedimentation and DLS techniques.

7.1.4. SEM Micrograph

The SEM micrographs of the SO–01 are given Figure 7.15. The minimum and maximum particle sizes observed from the micrograph were 1.02 and 28.42 µm, respectively in Figure 7.15.a and 3.2 and 28.36 µm respectively in Figure 7.15.b. The particles were irregularly shaped and nonporous. Particle size is around 20 µm according to the SEM images as seen in Figure 7.6 particle size is varying between 1–30 µm, SEM micrograph and particle size distributions have good agreement.

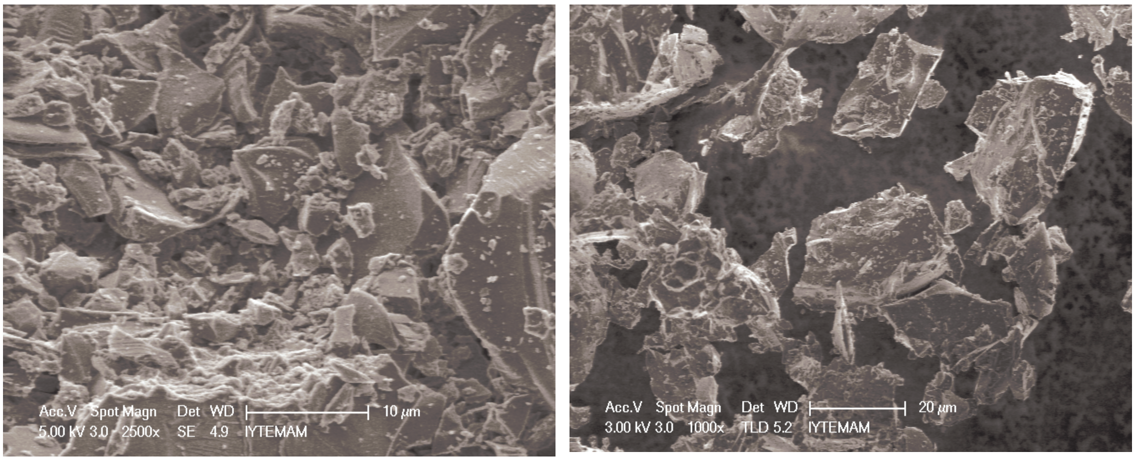

Figure 7.15. SEM micrographs of SO-01 silica powder.

The SEM micrographs of the SO-02 are given Figure 7.16. The minimum and maximum particle sizes observed from the micrograph, were 1.44 and 79.42 µm, respectively in Figure 7.16.a, and 0.44 and 17.37 µm respectively in Figure 7.16.b. The particles were irregularly shaped and nonporous.

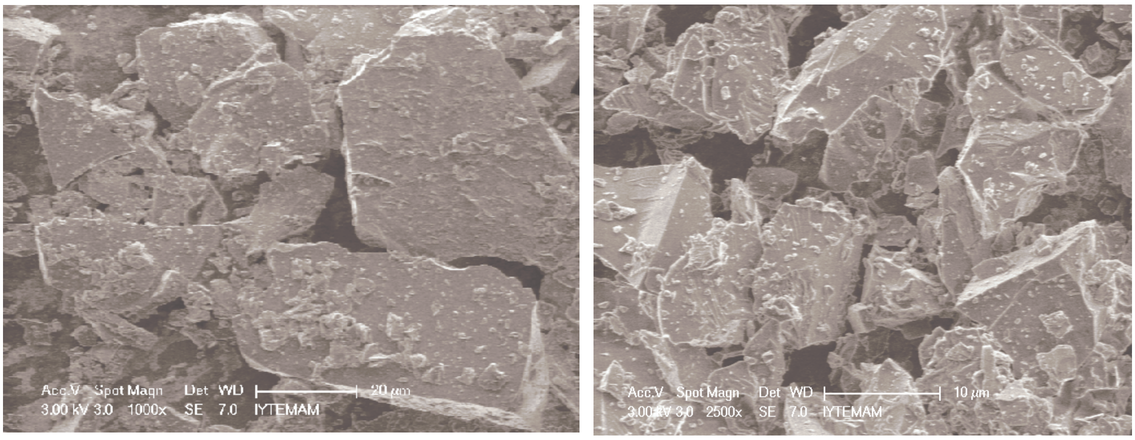

Figure 7.16. SEM micrographs of SO-02 silica powder.

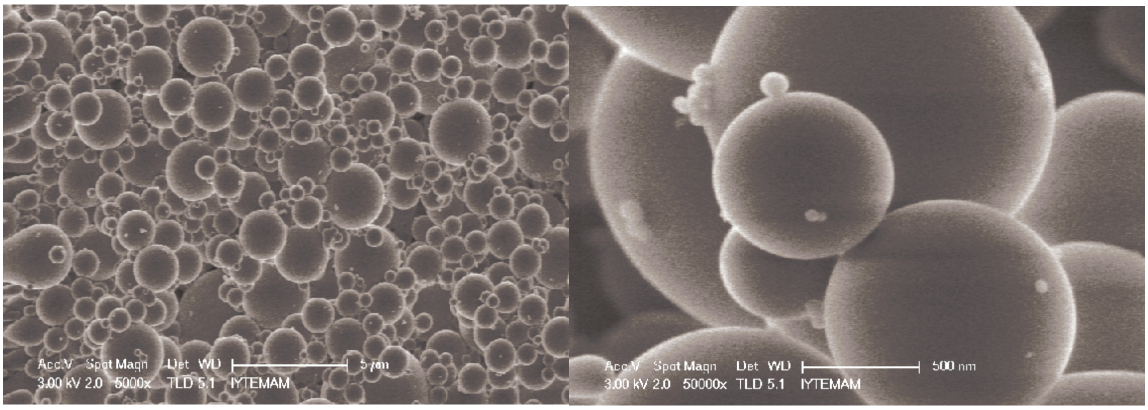

Figure 7.17. SEM micrographs of 01 silica powder SO-03.

The SEM micrograph of the alumina SO-03 is given Figure 7.17. The smallest and biggest sizes of the particles were observed from the micrograph, 0.27 and 3.02 µm, respectively in Figure 7.17.a. 0.37 and 1.7 µm respectively in Figure 7.17.b. The particles were nonporous and spherical shaped.

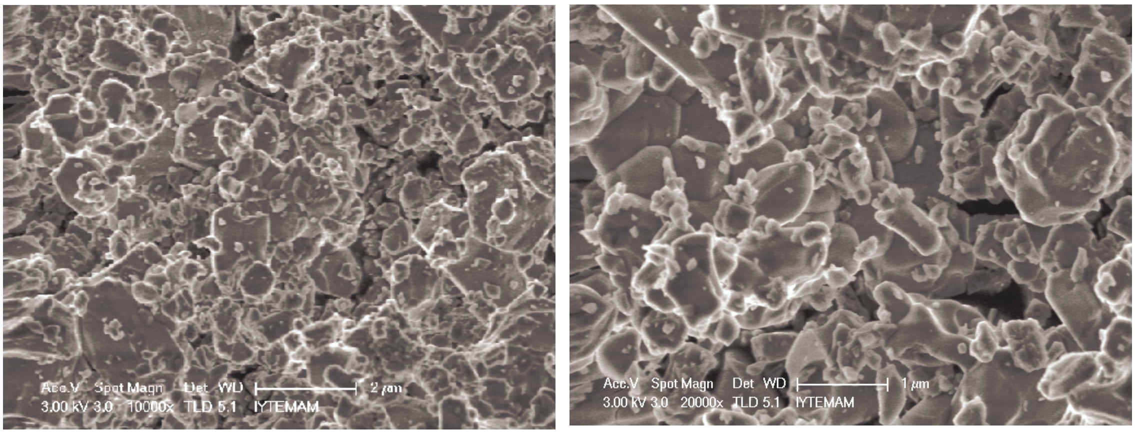

Figure 7.18. SEM micrographs of SN silicon nitride powder.

The SEM micrographs of the SN are given Figure 7.18. The smallest and biggest sizes of the particles were observed from the micrograph 0.19 and 2.72 µm, respectively in Figure 7.18.a, and 0.11 and 1.24 µm respectively in Figure 7.18.b. The particles were irregularly shaped and nonporous.

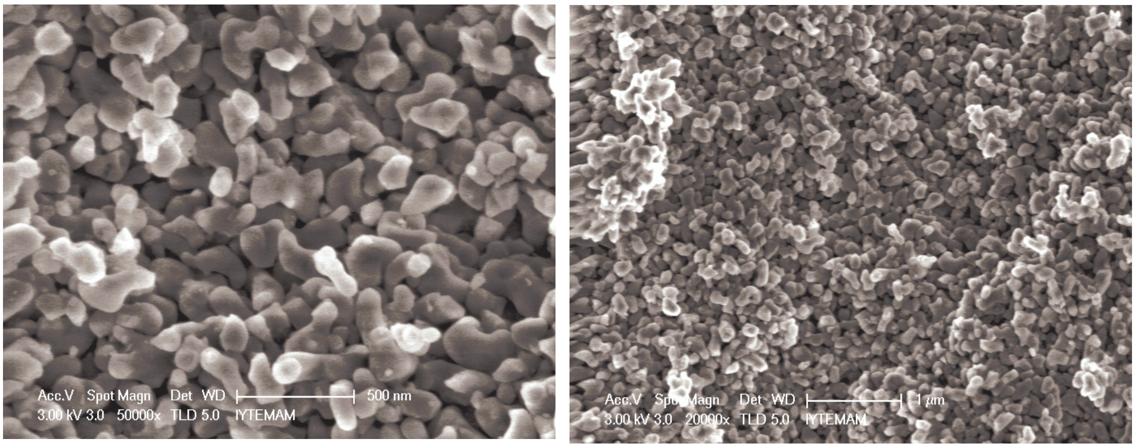

Figure 7.19. SEM micrographs of AO-01 alumina powder.

The SEM micrograph of the alumina AO-01 is given Figure 7.19. The smallest and biggest sizes of the particles were observed from the micrograph 83 and 284 nm, respectively in Figure 7.19.a and 0.06 and 0.47 μm respectively in Figure 7.19.b. The particles were irregularly shaped and nonporous.

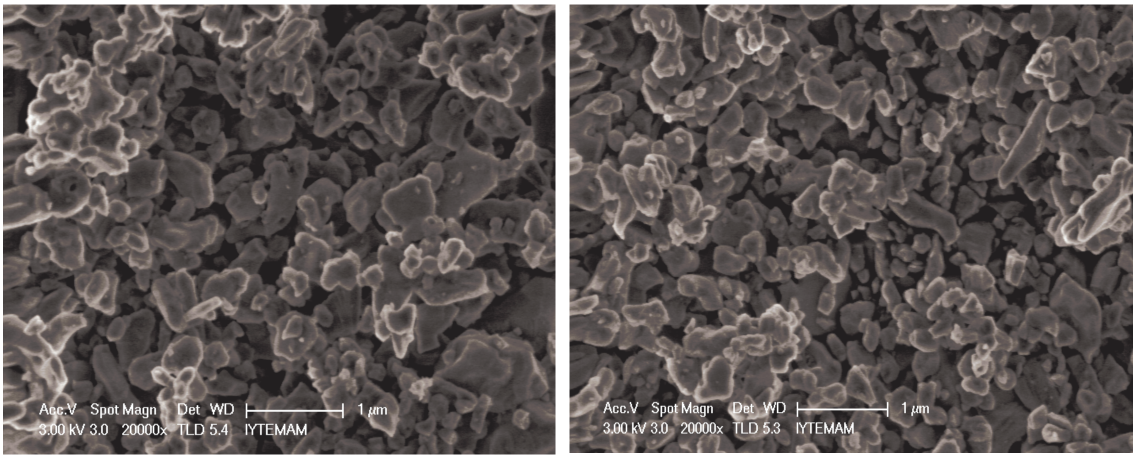

Figure 7.20. SEM micrographs of AO-02 alumina powder.

The SEM micrograph of the alumina AO-02 is given Figure 7.20. The smallest and biggest sizes of the particles were observed from the micrograph, 0.08 and 0.72 μm, respectively in Figure 7. 20. a. 0.09 and 0.98 μm respectively in Figure 7. 20. b. The particles were irregularly shaped and nonporous.

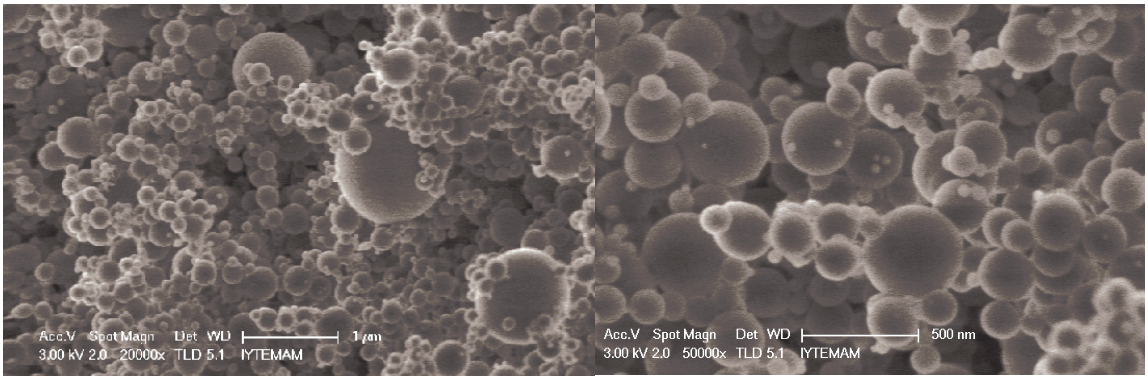

Figure 7.21. SEM micrographs of AO-03 alumina powder.

The SEM micrograph of the alumina AO-03 is given Figure 7.21 The smallest and biggest sizes of the particles were observed from the micrograph, 0.16 and 2.37 µm, respectively in Figure 7.21.a. 0.77 and 1.17 µm respectively in Figure 7.21.b. The particles were nonporous and spherical shaped.

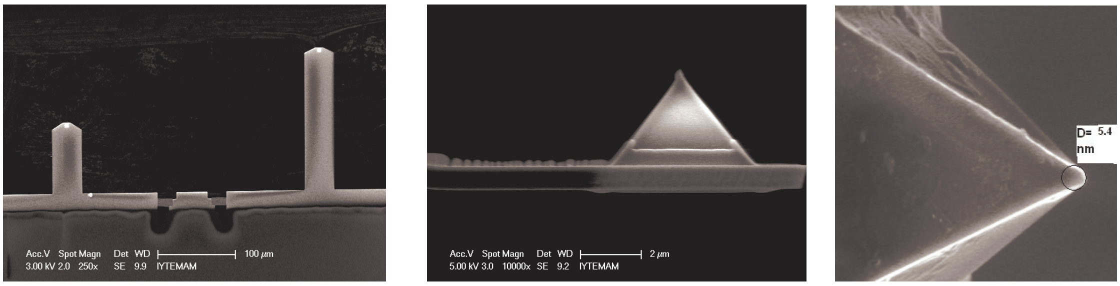

Figure 7.22. SEM micrographs of silicon nitride probe.

Probes (Veeco, ORC series) consisting of rectangular silicon nitrite cantilevers with integrated pyramidal tips with spring constant 0.73 nm. SEM micrographs of tips were presented in Figure 7.22. According to SEM images it is easily calculated and read the tip end curve radius is 2.7 nm for these tips.

7.1.5 FTIR Analysis of Powders

A major obstacle to understanding the intrinsic surface properties of metal oxides is the ubiquitous presence of hydrogen. Molecular H_2O and surface hydroxyl groups are generally present because of either the incomplete devaluation of H_2O from precursors or the adsorption of H_2O from the environment (Du et al., 1994, Hass et al., 2000, Eng et al., 2000,).The stabilities of different H_2O binding modes on different metal-oxide surfaces clearly depend on such factors as the surface structure, acidity of the surface metal site, and basicity of surface O. Dissociative adsorption is more favorable on R-Al_2O_3 (0001) than MgO (100), for example, because 3- coordinated surface Al is a much stronger Lewis acid than 5- coordinated surface Mg. understanding f the full effects of hydration, it’s the key parameter to understand surface properties (Hass et al., 2000). One of the most widely used methods for characterizing oxide surfaces is the spectroscopic analysis (FTIR) (Sides et al., 1988; Vazquez et al. 1997; Du et al., 1994; Baraton, 1999; Baake, 2009; Raharjo et al., 2000;Al-Abdeleh and Grassian, 2003; Shirai et al, 2005; Qi et al., 2005; Mc Cool et al., 2006; Dai et al., 2008).

FTIR spectra of a pure quartz and SiO_2 powders are given in Figure 7.23. The broad absorption band between 3700–3300 cm^{-1} has been assigned to the (OH) stretching vibration of surface hydroxyl groups involved in hydrogen bonds with water molecules and/or with adjacent silanols. The band at 1630 cm^{-1} corresponding to the OH bending vibration of adsorbed water molecules also decreases. In the 1000–400 cm^{-1} region of the spectrum have three main peaks. They are due to the decrease in the following modes: Si–O in Si–OH surface groups, –OH of the Si–O–H angle, and O–Si–OH of the O–Si–OH angle. Moreover, changes in the frequencies and/or band intensities, caused by thermal desorption, can be related to Si–O surface bonds distorted by surface dehydration. These distortions, which already exist on a surface in equilibrium with its environment, can increase when the equilibrium is displacing (Baraton, 1999). The peak located at about 2370 cm^{-1} was related with chemisorbed CO_2 on powder’s surface at 25 °C.

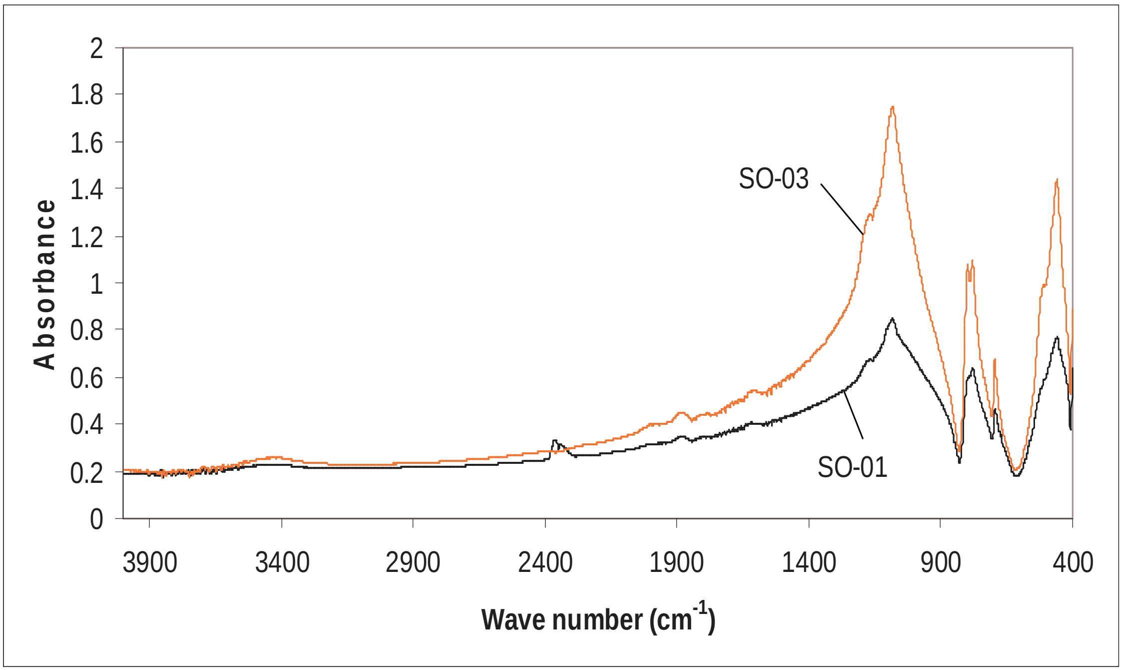

Figure 7. 23. The FTIR spectra of silica samples; SO-01 and SO-03.

Silicon nitride exists in two crystalline forms (α and β) and in an amorphous state. The crystalline morphologies exhibit unique vibrational fingerprints between 400–800 cm^{-1}. FTIR spectra of available Si_3N_4 powders to those reported in the Trout et (1989) we ascertained that the SN powder is a mixture of α and β phase but predominantly β–phase in composition. Also x–ray diffraction results which were given in Figure 7.4 showed that the same result. FTIR analysis were performed with α –phase and β–phase silicon nitride by Trout et al. 1989 showed sharp peaks at 462, 499, 601 and 685 cm^{-1} for α–phase, 586 cm^{-1} for α and β–phase.

The analysis of the FTIR spectra of SN powders is presented out in Figure 7.24. This analysis showed that the main absorption band mostly corresponds to the superposition of asymmetric stretching vibration of Si–N–Si bonds at 470cm^{-1}, symmetric stretching vibration of Si–N bonds at 970cm^{-1}, and stretching vibration of C–N or Si–O bonds at 1030cm^{-1} (Baake et al., 2009).

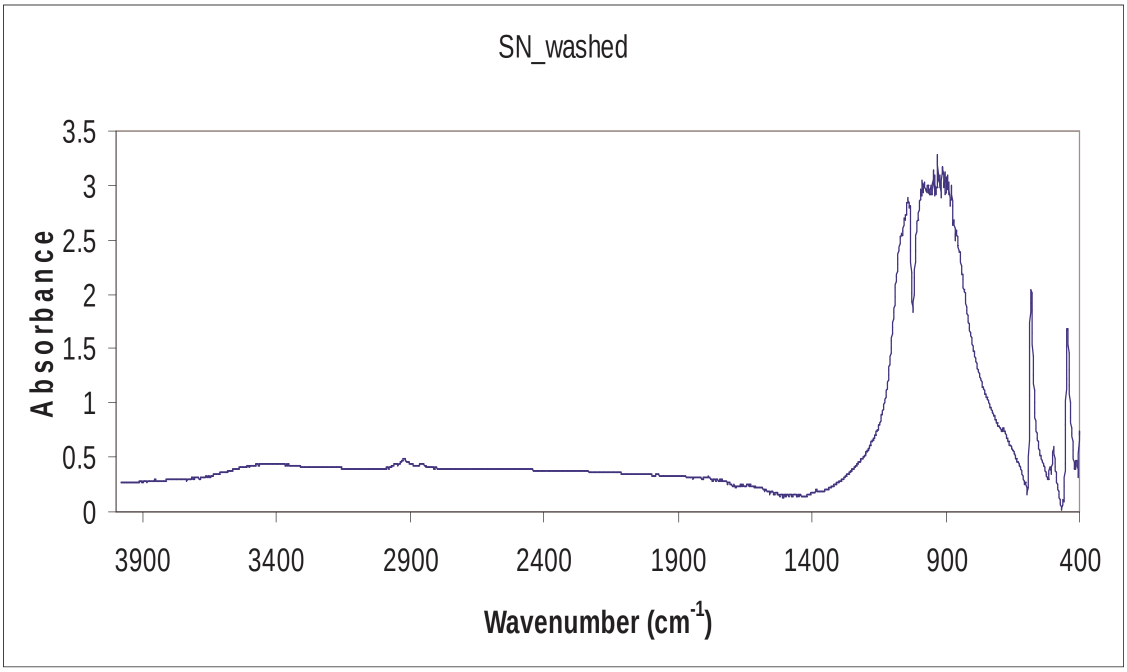

Figure 7. 24. The FTIR spectra of silicon nitride sample SN.

The weak bands observed at 1132 cm^{-1} were produced by the Al–O bonds. It showed bands at 830, 603, and 455 cm^{-1}, which probably were produced by vibrations of Al–O bonds corresponding to aluminum ions with tetrahedral symmetry as shown in Figure 7.25. The stretching vibration of the OH ions of residual water has a very intense broadband at 3200–3700 cm^{-1} (Vazquez et al. 1997), (Baraton, 1999).

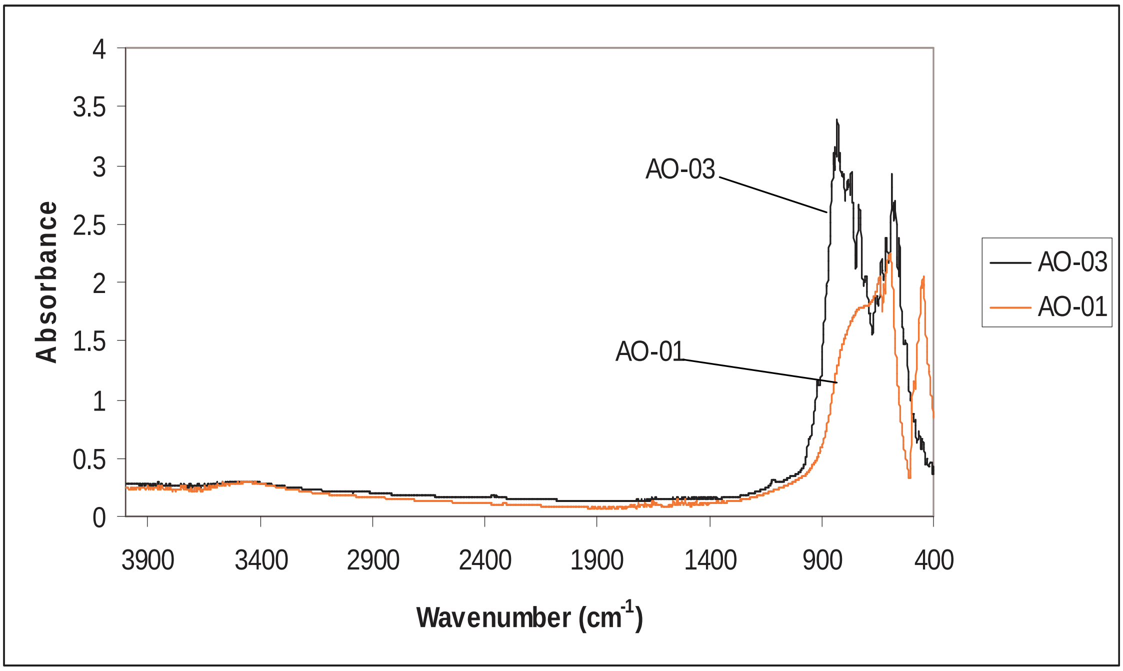

Figure 7.25. The FTIR spectra of alumina samples; AO-01 and AO-03.

Diffuse reflectance infrared fourier transform (DRIFT) spectra was obtained for silica, silicon nitride and alumina. Results of FTIR-DRIFT spectra measurements at 2500-400 cm^{-1} wavenumber range are shown in Figure 7.26- 7.34. The O-H stretching vibration bands were observed in the spectra of silica, silicon nitride and alumina samples. The distance between OH groups differ on the hydroxylated surface, some OH groups are closer together and stronger hydrogen bonds are formed between them. These show infrared absorption at 3250 cm^{-1}. Others are far apart and more weakly hydrogen bonded and show adsorption at 3600 cm^{-1}. Isolated single MOH or free hydroxyl groups in between 3745-3750 cm^{-1}, isolated pairs of adjacent MOH groups mutual hydrogen bonded in 3650-3660 cm^{-1}, adjacent pairs of MOH groups with hydrogen bonded o each other in 3540-3550 cm^{-1}, water molecule adsorbed on the above 3400-3500 cm^{-1} (Iler, 1979). The sharp peak at 3747 cm^{-1} is due to isolated hydroxyl groups on the silica surface (Mc Cool et al., 2006).

FTIR-DRIFT spectra measurements which the powder preparation method was given in Section 6.2.5 are shown in Figure 7.26-7.28 for silica powder at pH 2 and pH 10 at 2500-4000 cm^{-1} wavenumber range. Initial peaks corresponds wet powder, final peaks corresponds vacuum dried powders. The broad peaks were observed between 3000-3800 cm^{-1}. Silica powder FTIR spectra at pH 2, peaks between 3000-3300 cm^{-1} which corresponds the physisorbed water was reduced after vacuum and heating up to 40 ºC. The peak between 3300-3800 was not changed after vacuum and heating. In literature Sides et al. (1988) also found same results as our FTIR spectrum. Hydration properties of silica were investigated at atmospheric pressure and vacuum with heating powder up to 346 ºC. At atmospheric pressure at 26 ºC, they reported a broad band between 4000-2600 cm^{-1}. Further heating reduces the intensity on the 3725 cm^{-1} band is due to silanol group vibrations which became increasingly narrow and higher frequency as they become more isolated (Sides et al., 1988).

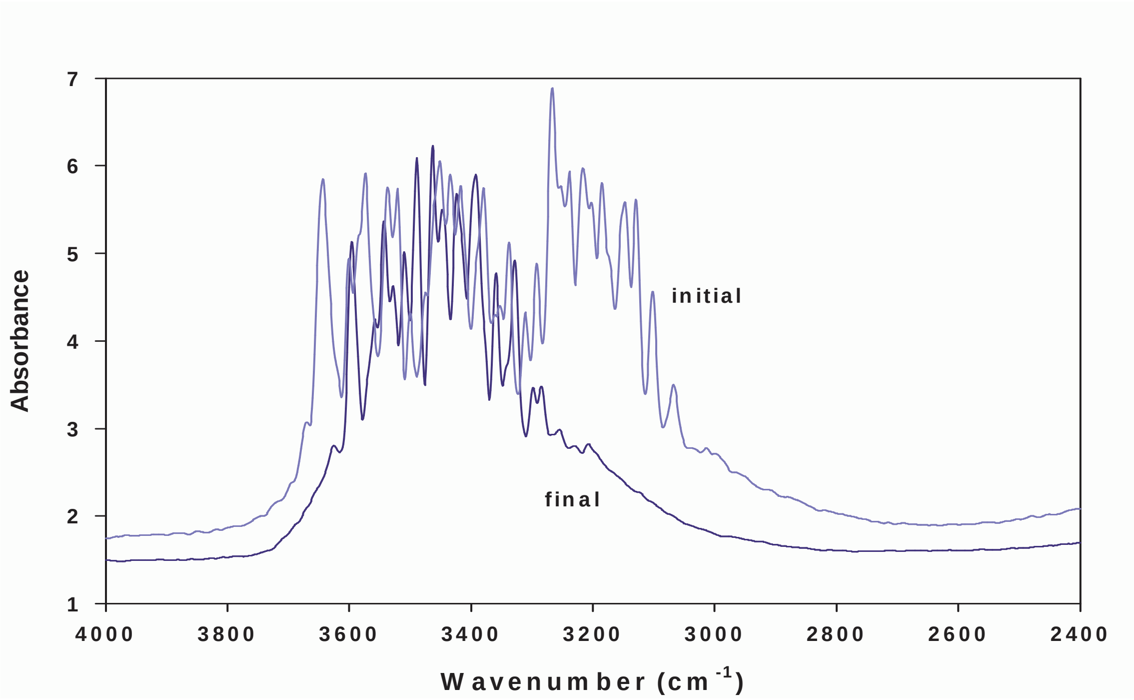

Figure 7.26. FTIR-DRIFT spectra for silica sample (SO-03) treated in 10^{-3} M KCl at pH 2 for 24 h. (Initial at atmospheric pressure 25 ºC, final at vacuum 40 ºC).

A silica powder FTIR spectrum at pH 10 broad peak was observed between 3000-3800 cm^{-1} as shown in Figure 7.27. The peak intensity was reduced after vacuum and heating up to 40 ºC, so weakly bonded OH groups were reduced.

FTIR-DRIFT spectra of pH2 and pH 10 was observed after vacuum and heating up to 40 ºC as shown in Figure 7.28.The peak intensity between 3800-2800 cm^{-1} was reduced at pH 10 compared with pH 2. This was not expected because the 3800-2800 cm^{-1} the O-H stretching vibration bands were observed. Especially powder was hydrated more at pH 10 because of basic environment, compared with pH 2.

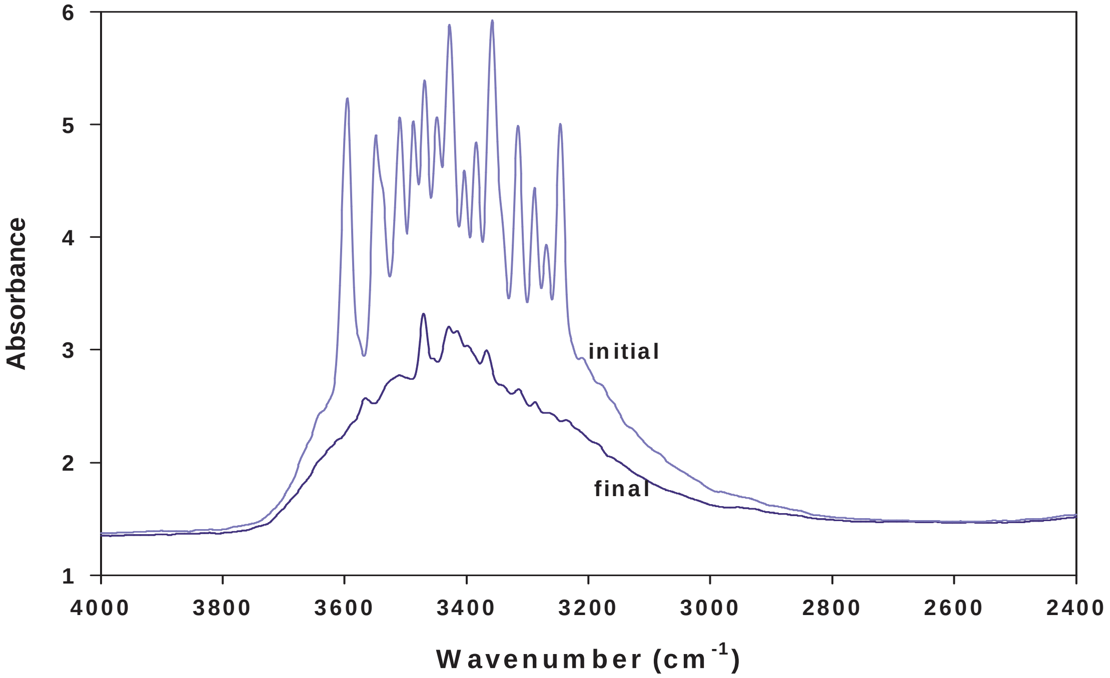

Figure 7.27. FTIR-DRIFT spectra for silica sample (SO-03) treated in 10^{-3} M KCl at pH 10 for 24 h. (Initial at atmospheric pressure 25 ºC, final at vacuum 40 ºC).

Du et al., (1994) investigated pH and electrolytes effect on quartz. They have found that the two peaks at 3200 and 3450 cm^{-1} vary with the pH value in water. At low pH (1.5) the spectrum indicates that most of the interfacial water molecules are orderly arranged with tetrahedral coordination. If the quartz surface is neutral (at pH 1.5), then interfacial water molecules tend to form hydrogen bonds with their oxygen facing the quartz surface, opposite to the orientation expected for high pH case. As pH values increase (pH 3.8-12.3) the relative strength of the two peaks varies, with pH> 5.6 both peaks get strengthened, with former increasing more rapidly. At pH 12.3 the peak strength decrease compared with pH 8. High pH case, the signal strength is much smaller, with hydrogen bonding to the surface providing orientation force; one would expect only 1 or 2 monolayer of water molecules being oriented. This supports the argument that for the high pH case, the surface field can align up to 3 to 5 layers of semi-long-range nature of the hydration force at ionic surfaces and well accepted view that oriented water molecules are the origin of the repulsive hydration force between surfaces (Du et al., 1994) . To further confirmation of the opposite orientation at low and high pH at quartz/water interfaces, they were measured the FTIR spectra of quartz/water interfaces by dissolving at 0.5M NaCl solution. They found that at low pH case with quartz being neutral, the salt ions have no effect on the spectrum. For high pH case, the addition of NaCl reduces the spectra intensity because of screening of the surface field by the positive Na^+ ions (Du et al., 1994). Li et al. (2004) was also found the same results, which they used NaOH solution at pH 10, the peak intensity was decreased at 3450 cm^{-1}, and the AFM images showed that the surface flattens following prolonged exposure to base. The flattening is attributed to an electrostatic barrier protecting the surface from water attack. According to literature, in Figure 7.28 the broad peak between 3800-2800 cm^{-1} was observed the peak intensity at pH 2 much higher than pH 10.

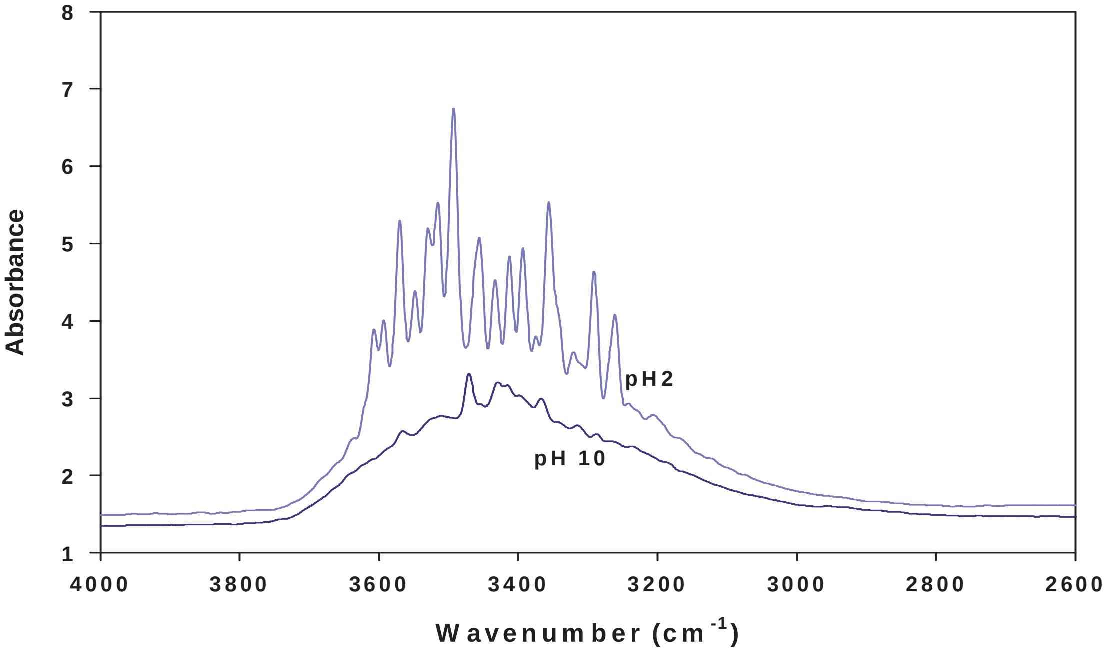

Figure 7.28. FTIR-DRIFT spectra for silica sample (SO-03) treated in 10^{-3} M KCl at pH 2-pH 10 for 24 h (after vacuum at 40 ºC).

FTIR-DRIFT spectra measurements at 2500-4000 cm^{-1} wavenumber range are shown in Figure 7.29-7.30 for silicon nitride (SN) sample treated in 10^{-3} M KCl at pH2 and pH 10 for 24h. Initial peaks corresponds wet powder, final peaks corresponds vacuum dried powders. The broad peaks were observed between 2800-3800 cm^{-1}. The peak intensity was reduced after vacuum and heating up to 40 ºC, so weakly bonded OH groups were reduced.

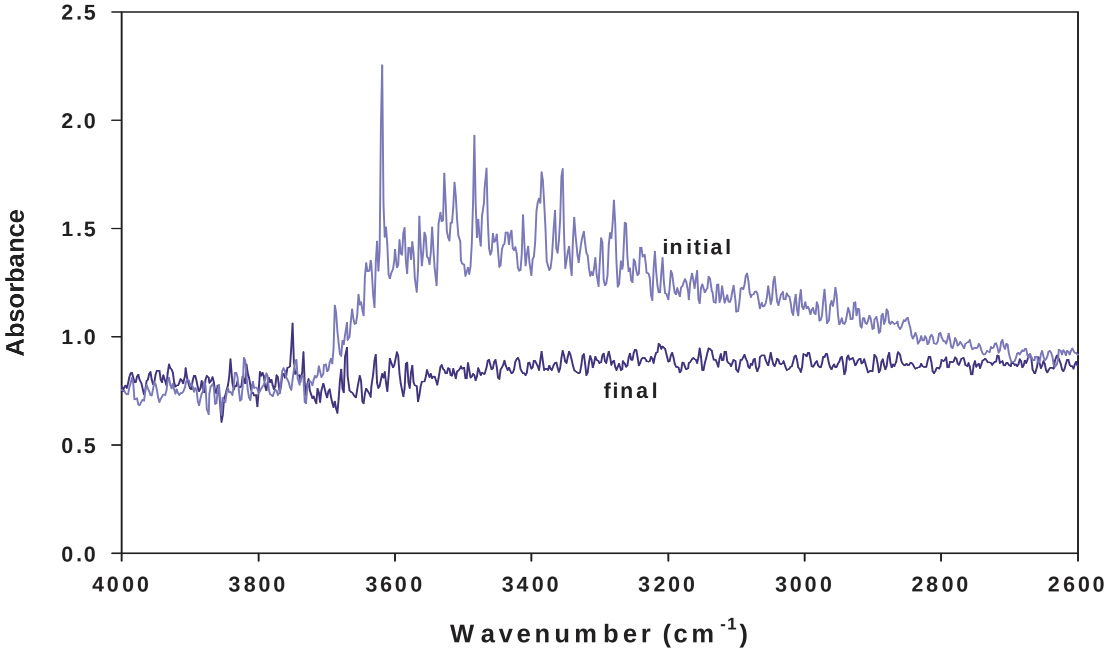

Figure 7.29. FTIR-DRIFT spectra for silicon nitride (SN) sample treated in 10-3 M KCl at pH 2 for 24 h. (Initial at atmospheric pressure 25 ºC, final at vacuum 40 ºC).

Silicon nitride powder FTIR spectra at pH 10 broad peak were observed between 2800-3800 cm^{-1} as shown in Figure 7.30. The peak intensity was reduced after vacuum and heating up to 40 ºC, so weakly bonded OH groups were reduced.

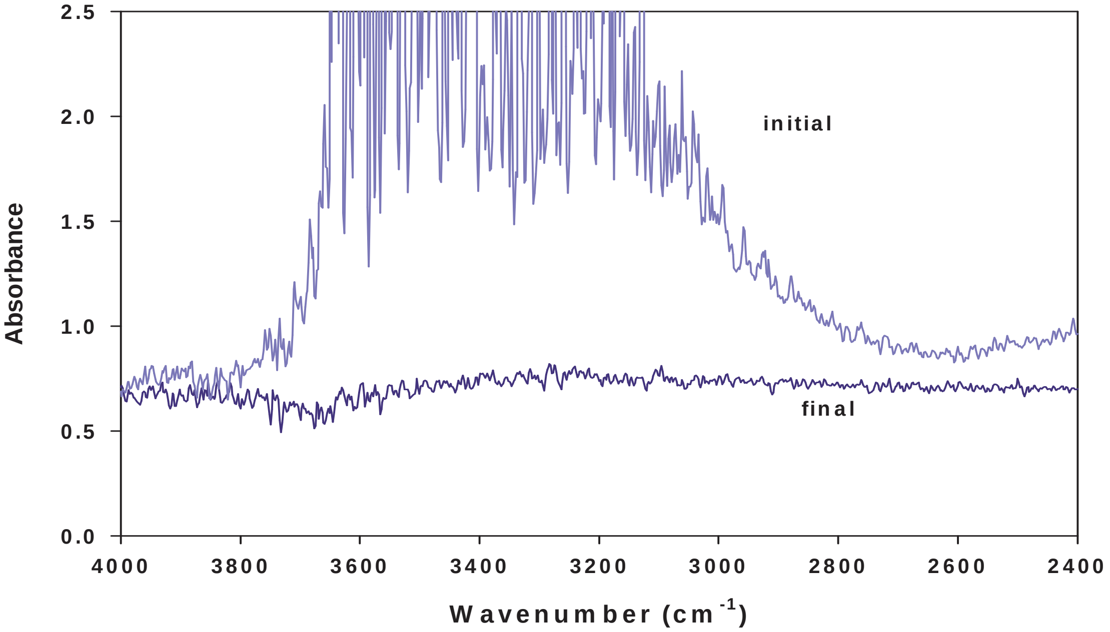

Figure 7.30. FTIR-DRIFT spectra for silicon nitride (SN) sample treated in 10^{-3} M KCl at pH 10 for 24 h. (Initial at atmospheric pressure 25 ºC, final at vacuum 40 ºC).

Dai et al., (2008) who investigated four types commercial silicon nitride powders with influences of acid leaching, surface hydrolysis and thermal oxidation with DRIFT spectra. The DRIFT spectra of acid cleaned surface at 2600-4000 cm^{-1} change little compared with received powders. Hydrolyzed powder peak intensity at 2600-4000 cm^{-1} as much higher than 150 ºC dried powders. FTIR-DRIFT spectra in Figure 7.29-7.30 for silicon nitride (SN) sample at pH2 and pH 10 were shown the same results as in literature, hydrolyzed powders at pH 2 and pH 10, peak intensity was decreased after vacuum heating.

FTIR-DRIFT spectra of SN sample at pH2 and pH 10 was observed after vacuum and heating up to 40 ºC as shown in Figure 7.32. The peak intensity between 3800-2800 cm^{-1} was not changed at pH 2 and pH 10. FTIR spectrum of silicon nitride was analyzed and the adsorption bond of Si–OH group is centered at 3355 cm^{-1} which is assigned to Si–NH–Si imido group by Baraton et al. (1999). Also they found υ-NH symmetric and asymmetric stretching frequencies absorb as shoulder in the 3580–3450 cm^{-1} range. The silanols and Si-NH-Si imido groups were presented in abroad bond between 3500-3000 cm^{-1}. They also found an Si-OH group at around 3700 cm^{-1} in which the silicon neighboring atoms are not three oxygen atoms as on silica. . In Figure 7.31, the broad band between 2800-3700 cm^{-1} was not changed influence of pH because of that region was depicted υ-NH symmetric and asymmetric stretching frequencies and NH-Si imido groups. Only, the peak at 3750 cm^{-1} which corresponds Si-OH group was observed at pH 10 compared with spectra of pH 2.

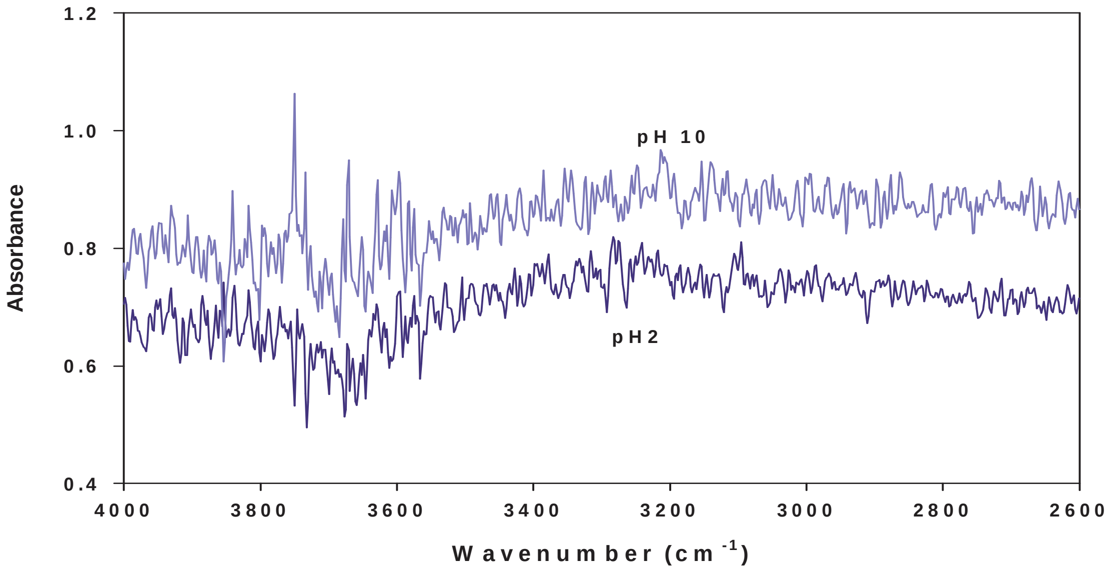

Figure 7.31. FTIR-DRIFT spectra for silicon nitride (SN)sample treated in 10^{-3} M KCl at pH 2 –pH 10 for 24 h (after vacuum at 40 ºC).

The presence of hydroxyl groups on the surface with hydrogen-bonding contributions also is supported by recent theoretical calculations of the interaction of water with α-Al_2O_3 (0001) surfaces. These studies suggest that, under sufficiently high water loadings, the surface Al atoms on the single Al-terminated surface convert to terminal $AlO_3(OH)_3$ species, which should be highly labile, and their removal or diffusion results in a OH-terminated surface The simulations of Hass et al. (2000) on the OH-terminated surface suggest that extensive hydrogen bonding occurs in-plane among the surface hydroxyls and that the hydrogen bonding is dynamic, with an average of one of three hydroxyls lying in the surface plane. They also calculated O-H vibrational frequencies are consistent with known trends on alumina but indicate a discrepancy between experimental observations for α-Al_2O_3 (0001) and models based on simple hydroxylation.

FTIR-DRIFT spectra of the surface of the α-alumina sample, which was treated for 24 h in pH 2 and 10 KCl 10-3 M solutions, are given in Figure 7.32 and 7.33 respectively. It can be seen that the reflectance for the OH stretching region between wavelengths 3300 and 3600 cm−1 was increased as relative humidity increased.

Raharjo et al. (2000) observed surfaces of the different α-alumina powders using FTIR-DRIFT analysis. They observed broad peaks at approximately 3300 cm^{-1}, 3450 cm^{-1} and 3690 cm^{-1}. DRIFT spectra of alumina powders. The broad peak at 3300 cm^{-1} might be partially attributed stretching vibrational modes of water molecules physisorbed on the alumina surface hydroxyls modes. Baraton et al. (2000) was observed a small peak at 3700 cm^{-1}free hydroxyl groups. Shirai et al. (2005) also was investigated DRIFT spectrum of alumina powder and found 3400-3450 cm^{-1} depicted hydrogen bonded OH. Hass et al (2000) gave a table for type of OH group versus wavenumber for a-alumina (0001). In 3450-3560 was depicted molecularly adsorbed water, 3780 and 3430 cm^{-1} attributed dissociated water, 3650 cm-1 was assigned free hydroxyl groups and finally 3470 cm-1 bond was depicted hydrogen bonded OH.

At pH 2 initial and final spectra was not showed the much difference only free hydroxyl groups and physisorbed water molecules peak intensity was reduced after heating under vacuum condition.

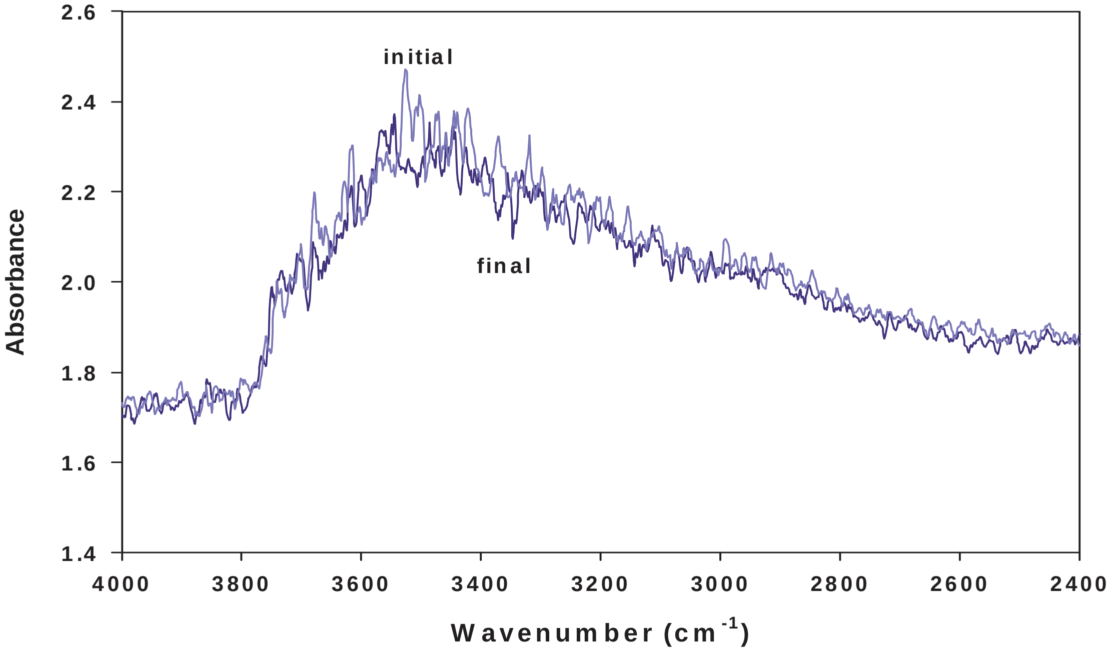

Figure 7.32. FTIR-DRIFT spectra for alumina (AO-03)sample treated in 10^{-3} M KCl at pH 2 for 24 h. (Initial at atmospheric pressure 25 ºC, final at vacuum 40 ºC).

At pH 2 and pH 10 the DRIFT spectrum showed that the broad peak at 3300 cm^{-1} were decreased because the peak attributed stretching vibrational modes of water molecules physisorbed on the alumina surface hydroxyls modes. In other words when the water molecules evaporates the peak intensity was decreased. Al-Abadleh and Grassian, (2003) also measured the DRIFT spectrum of alumina powder in various relative humidity. They found OH bond in the range extending from 3660-270 cm^{-1} and as RH was increased, the coverage of adsorb water increased. At pH 10 initial and final spectra showed the difference because of the basic nature, free hydroxyl groups and physisorbed water molecules peak intensity was reduced after heating under vacuum condition.

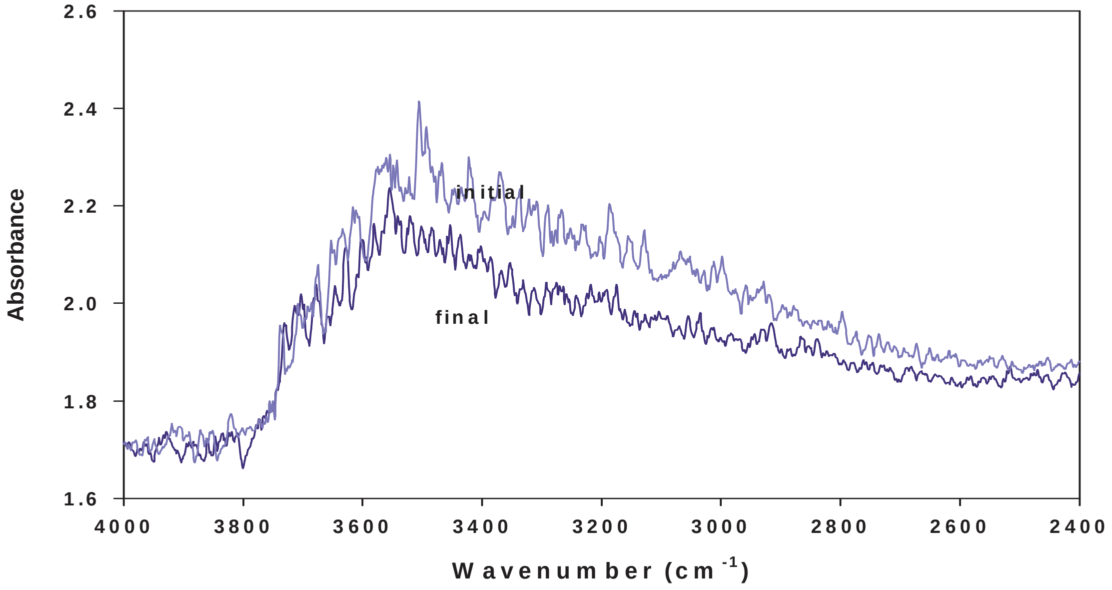

Figure 7.33. FTIR-DRIFT spectra for alumina (AO-03) sample treated in 10^{-3} M KCl at pH 10 for 24 h. (Initial at atmospheric pressure 25 ºC, final at vacuum 40 ºC).

FTIR-DRIFT spectra of the surface of the α-alumina sample, which was treated for 24 h in KCl 10^{-3} M solutions with pH 2 and 10, are given in Figure 7.34. It can be seen that the reflectance for the OH stretching region between wavelengths 2800 and 3800 cm−1, which corresponds to the H-bonded water, is deeper in the case of pH 10. The spectrum of pH 10 was showed a little difference; main OH bands peak intensity was higher than the OH peak intensity at pH 2.

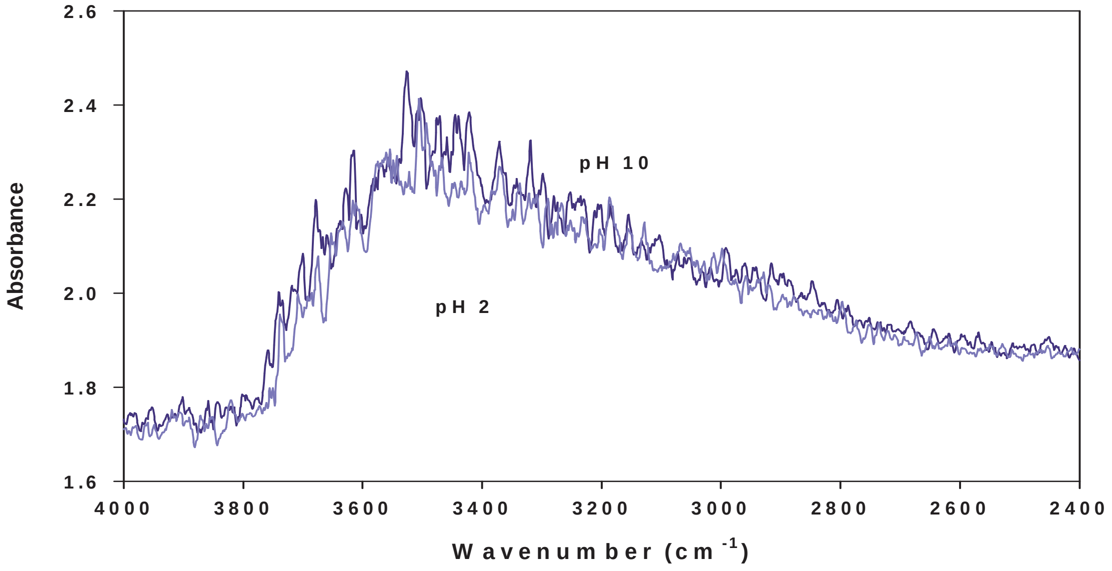

Figure 7.34. FTIR-DRIFT spectra for alumina (AO-03) sample treated in 10^{-3} M KCl at pH 2-pH 10 for 24 h (after vacuum at 40 ºC).

7.1.6 XRF Measurement of Substrate

Glass substrate was investigated by using XRF (METEC–Spektro IQ II). The composition of the oxides was tabulated in Table 7.4. According to XRF analyses the SiO_2 content in the glass is 71.2 %. XRF experiments were not performed for silica and alumina single crystals because single crystals with their one polished sides were not suitable for XRF experiments.

Table 7.4. XRF analysis results of glass surface

Element	**%**
Na_2O	17.3
Al_2O_3	7.7
SiO_2	71.2
K_2O	4.7
TiO_2	2.9
Other oxides (MgO, CaO, MnO)	0.7

7.1.7. Surface Topography by AFM

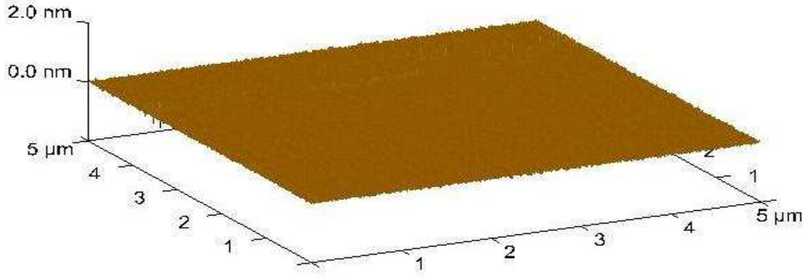

Figure 7.35. Surface topography analysis of glass substrate using AFM.

Surface roughness of the smooth glass substrate was investigated by AFM. The roughness data are; Ra =0.118 nm, Rq=0.200 nm, Rz=0.133 nm, Rmax=1.8 nm, as shown in Figure 7.35.

In Figure 7.36, surface topography images of quartz (0001) single crystal surface are shown. The surface roughness of smooth quartz (0001) substrate were investigated by AFM. The roughness data are; R_a =0.109 nm, R_q=0.141 nm, R_z=0.123 nm, R_{max}=1.79nm.

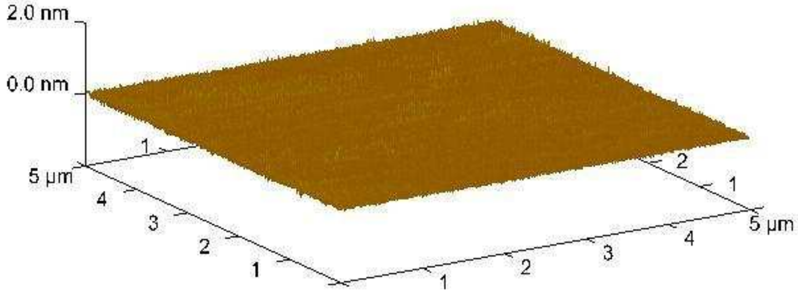

Figure 7.36. Surface topography analysis of quartz substrate using AFM.

Surface topography images of sapphire (0001) single crystal surface are shown in Figure 7.37,.The sample was atomically smooth with a surface roughness of Ra =0.107 nm, Rq=0.098 nm, Rz=0.113 nm, Rmax=1.2 nm, as determined by the AFM scans.

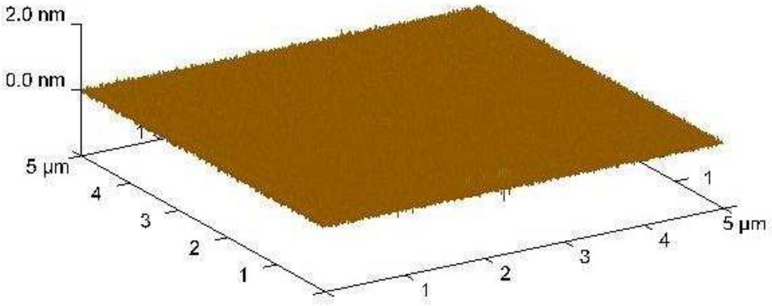

Figure 7.37. Surface topography analysis of sapphire substrate using AFM.

7.2. Characterization of Powders and Substrates Relevant to Charge and Force Measurements

7.2.1. Electrokinetic Potential Measurements of Powders

Electrokinetic methods have been used to estimate the electrical potential difference between charged oxide surface and bulk solution electrokinetic potential measurements were investigated by *Zetasizer Nano–Zs* (Gebze Institute of Technology). Only SO-01, SO-02, SO-03, SN,AO-01, AO-02 and AO-03 powders were measured by Zetasizer.

Zeta potentials of oxides are a result of the distribution of ions around the solid particles. Calculations of potentials from the motilities are a problem in itself. Its accurate solution is known for spherical particles. For small particles ($\kappa r < 100$, where r is the radius), the result depends on the particle size used in the calculations; therefore a dispersion of uniform, spherical particles is desirable for electrophoretic measurements. Methods to obtain such particles of various oxides have been developed by Matijevic (1993). Obviously, particles prepared using these methods are not identical but the distribution of particle size is narrow enough to avoid serious errors due to sample polydispersity. The samples of oxides used in electrophoretic studies should be analyzed in terms of the shape and size distribution of the particles to assess how the deviation from spherical shape and/or polydispersity may affect the calculated ζ-potentials. Systematic studies of the solvent effect on the potentials of various oxides were carried out by Kosmulski (2009).

For SO-01 powder, the pH dependence of the zeta potential in water and 0.001M is shown in Figure 7.38. As expected for such oxides, the zeta potential is negative at the higher pH, with a plateau region from pH 3–12. This behavior may be explained by the proton equilibria that occur at the surface of the oxides. According to quartz particle surface charge, zeta potential is still negative even in low pH. Kosmulski (2009) reviewed many oxide particles point zero charge (pzc). One of the unspecified Silica’s from Sigma–Aldrich with BET surface area is 1 m^2/g; was investigated with KCl electrolyte by using DLS Nano ZS, they have found the pzs at pH 2.1. Another unspecified Silicas from Sigma were investigated with NaCl, $NaNO_3$ electrolyte, they have found the pzs at pH samller than 2. (Kosmulski, 2009). SO-01 powder was investigated under deionized water with various pH, to find pzc.

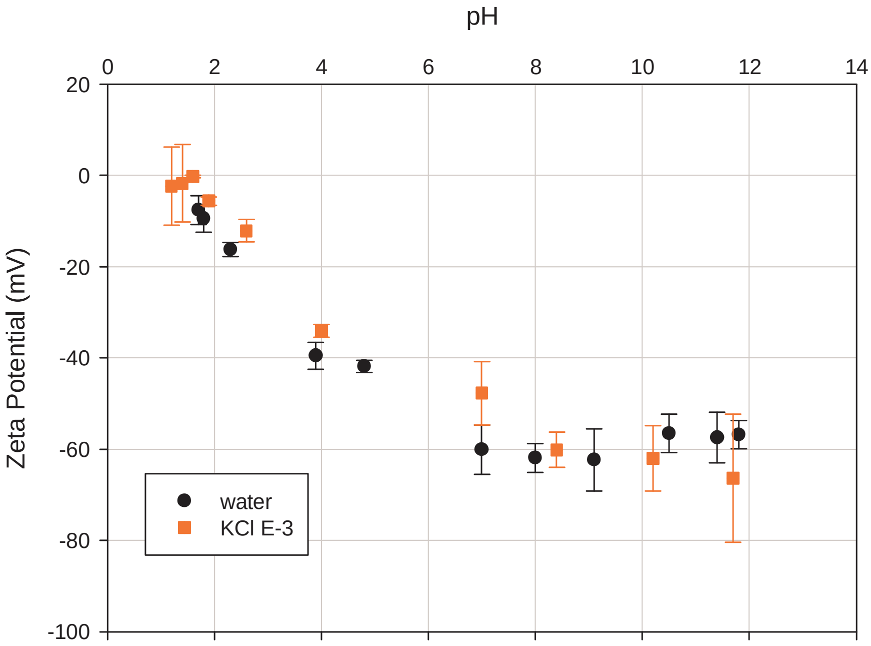

Figure 7.38. Zeta Potential of SO-01 powder in deionized water and 10^{-3}M KCl.

For natural SO-02 powder the pH dependence of the zeta potential in water, is shown in Fig.7.39. Natural quartz powder was investigated in deionized water and its pzc was found to be around at pH 2. Kosmulski (2009), acid washed quartz mineral from Earth with the particle size mean diameter 2 µm ; was investigated with 0.0007 M NaCl electrolyte , they have found the pzc at smaller pH 1.

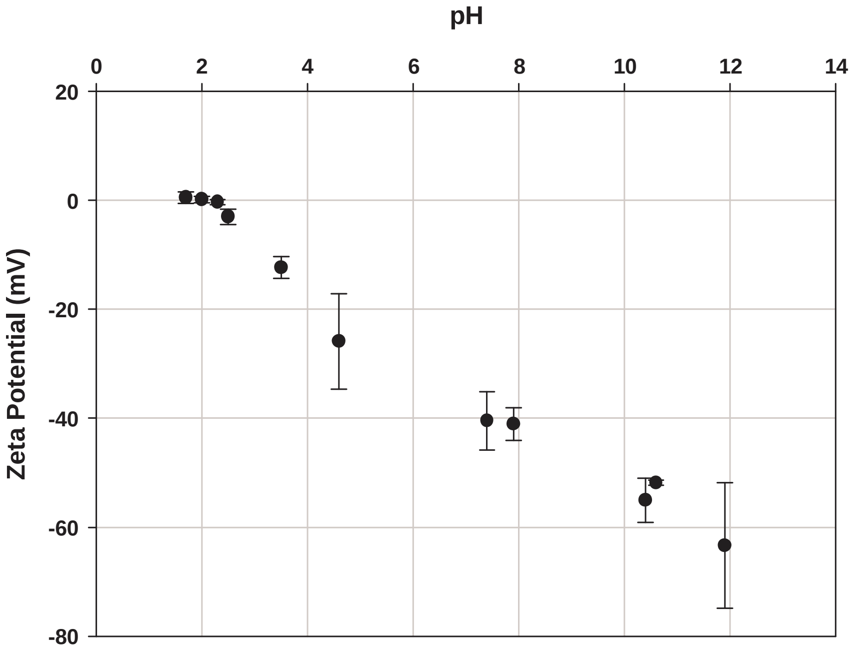

Figure 7.39. Zeta Potential of SO-02 powder in deionized water.

For SO-03 powder the pH dependences of the zeta potential in water, 0.01 M and 0.001M KCl are shown in Figure 7.40. The average magnitude of the zeta potential is greater in 0.001 M than in 0.01 M, a result which may be explained by a decrease in the effective thickness of the diffuse layer as the ionic strength increases. The isoelectric point (iep), that is the pH at which the particle has a zeta potential of zero, is smaller than 2. The same value is obtained for both ionic strengths. The fact that pH (iep) is independent of the ionic strength indicates either the absence of a specific adsorption of $C1^-$ and K^+ ions or a nearly identical adsorption of both co– and counterions or a noticeable affinity for one ion (Mullet et al., 1997). Indeed, if the affinity of the adsorbed ion is very high, the surface may be saturated by a very low electrolyte concentration. Therefore, the pH (iep) appears not to change as ionic strength varies. It is thus necessary to vary the nature of the electrolyte to verify the position of the real pH (iep).

There was no chance to compare literature data of silicon dioxide powder which commercial name is Admatech SO-E6, because of unstudied powder. SO-03 powder iep was found between pH 3-4 in water, 10^{-2} M and 10^{-3} M KCl. Surface potential of the powder was measured -5 mV, -35 mV and -70 at pH 2, 6, 10 respectively.

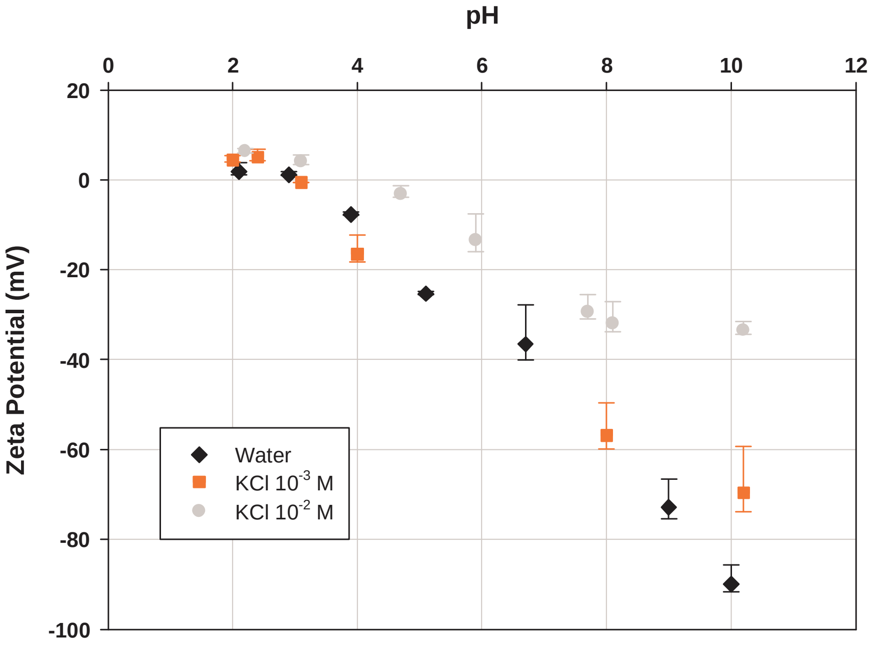

Figure 7.40. Zeta Potential of SO-03 powder in deionized water, KCl 10^{-3}M and 10^{-2}M.

The zeta potentials of the Si_3N_4 surfaces are shown in Figure 7.41. The measurements made in deionized water and 0.001M KCl. The ieps of the Si_3N_4 lie within the range pH 2–3. Whitman and Feke, (1988) examined the five different suppliers silicon nitride powders to perform surface titration methodology. They have found the pzc of these silicon nitride powders, 7.7, 6.7, 3.2, 8.6, 7. Even though, silicon nitride specimen from different manufacturers exhibit little difference in the magnitude of relative proton adsorption over the pH range studied. This indicates that silonol site density on the various powders roughly equivalent.

Bergström and Pugh, (1989) investigated the iep of three different silicon nitride powders, found 4.2, 6.7–8, 6.2. But the original difference in iep between three powders disappears by aging the powders.

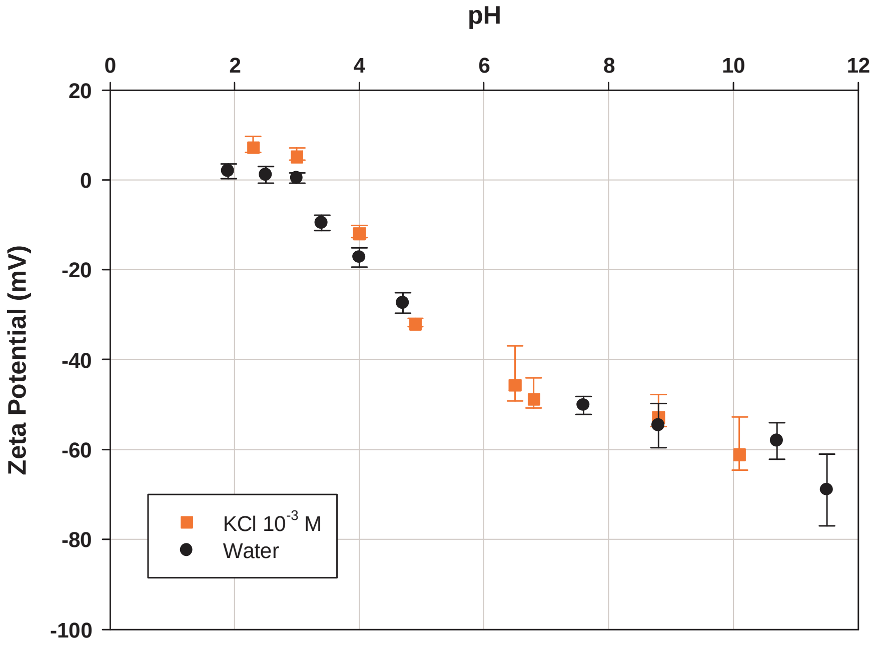

Figure 7.41. Zeta Potential of SN powder at deionized water and 10^{-3} M KCl.

The zeta potential measurements of AO-01 were investigated in deionized water. The data was shown in Figure 7.42. The ieps of the Sumitomo AO-01 α-alumina lie within the range pH 8.8–9.These results are in good agreement with those of Kosmulski (2009). They have investigated Sumitomo AKP 50 under different electrolyte types and concentrations, ieps are changing between 7.9–9.6 .For the pre–acid washed powders ieps are between 9–9.7.

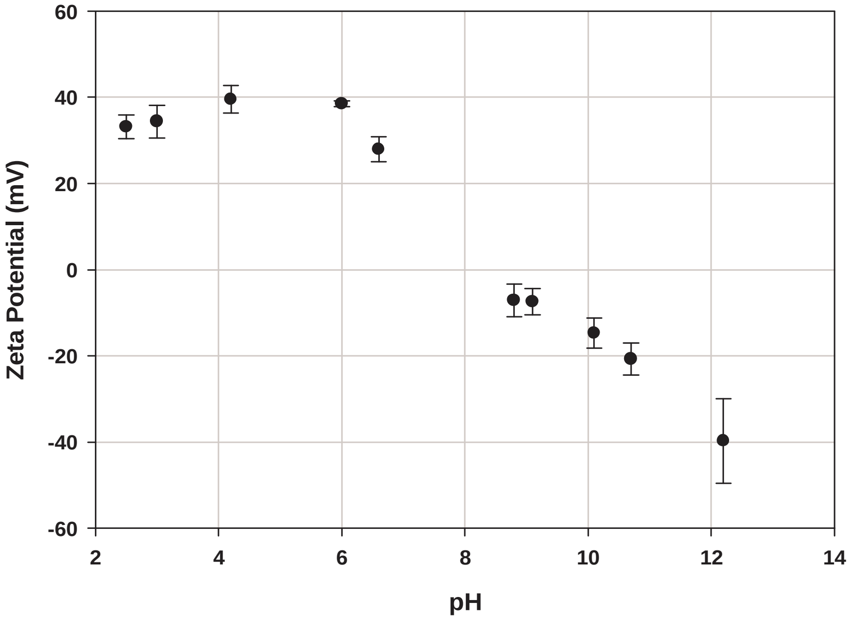

Figure 7.42. Zeta Potential of AO-01 powder at deionized water.

For AO-02, α–alumina powder the pH dependence of the zeta potential in water, is shown in Figure 7.43. As expected for α–alumina, the zeta potential is negative at the higher pH, at about pH 10–12. Then, zeta potential decreases and becomes positive towards the lower end of the pH range 7 –7.7. Iep of the AO-02 α-alumina is the range 7.7–8.1. This result is in good agreement with those of Kosmulski (2009). They have investigated CT3000SG under different electrolyte types and concentrations, ieps are changing between 8–8.3.

Another α–alumina powder (AO-03) was analyezed by zeta potential in deionized water, 10^{-3}M and 10-1M KCl as shown in Figure 7.44. The pzc was found around pH 7.8 in 10^{-3}M and 10^{-1}M KCl solution, around pH 8.1 in water. Zeta potential measurement of Admatech AO-802 was examined by Polat et al., 2006. They found pzc of the alumina powder in 10^{-2} M KCl pH 9.1. It can be seen that the zeta potential of sample shows to 60 mV, 20 mV and −58 mV at pH 2, 6, 10 respectively.

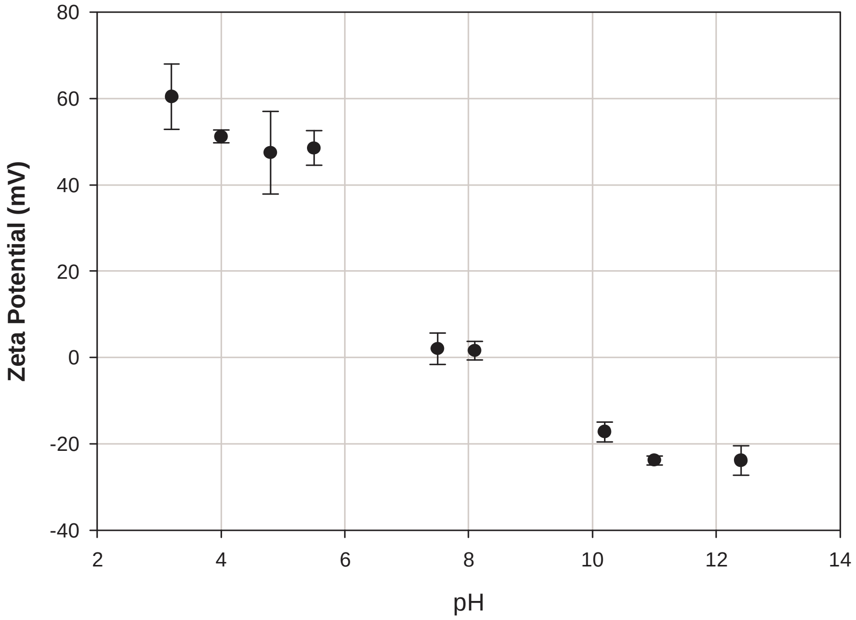

Figure 7.43. Zeta Potential of AO-02 powder in deionized water.

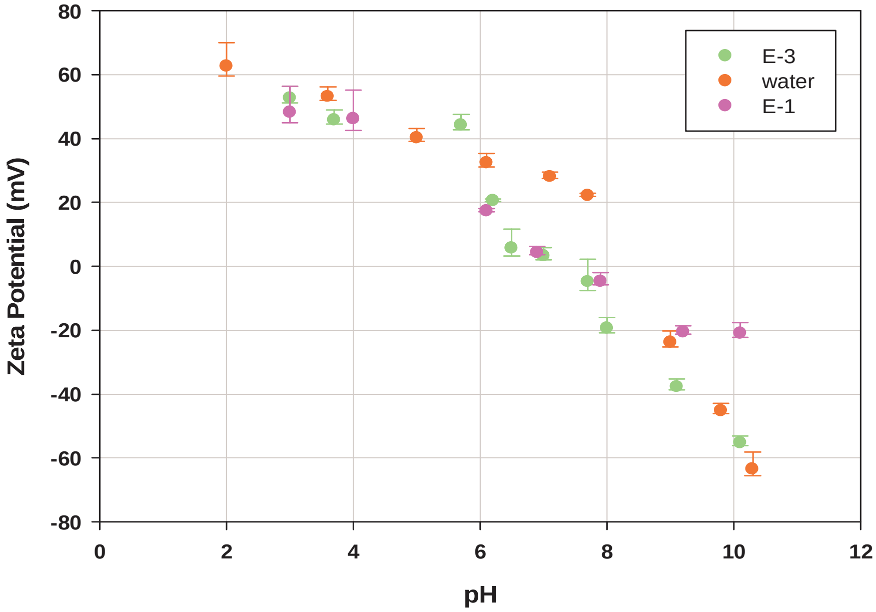

Figure 7.44. Zeta Potential of AO-03 powder in deionized water and 10^{-3}M and 10^{-1}M KCl.

Zeta potential measurement with fresh glass powders were carried out in 10^{-3} M KCl solution at a solid/liquid ratio of 0.1 g/L and then results are presented in Figure 7.45. The measurements were carried out using Zeta-Meter 3.0 which relies on eye observations. Hence, each zeta potential was an average of 10 readings. These zeta potential measurements which were obtained with powdered glass coverslip gives an idea about the average pzc of the glass coverslip. According to XRF measurement of glass coverslip which is tabulated in Table 7.4 on page 88, SiO_2 content is 71%. In the literature and our quartz and silica zeta potential measurement it was observed that the pzc of the glass was between pH 2 and 4. So pzc of the glass coverslip was in good agreement with previous measurements.

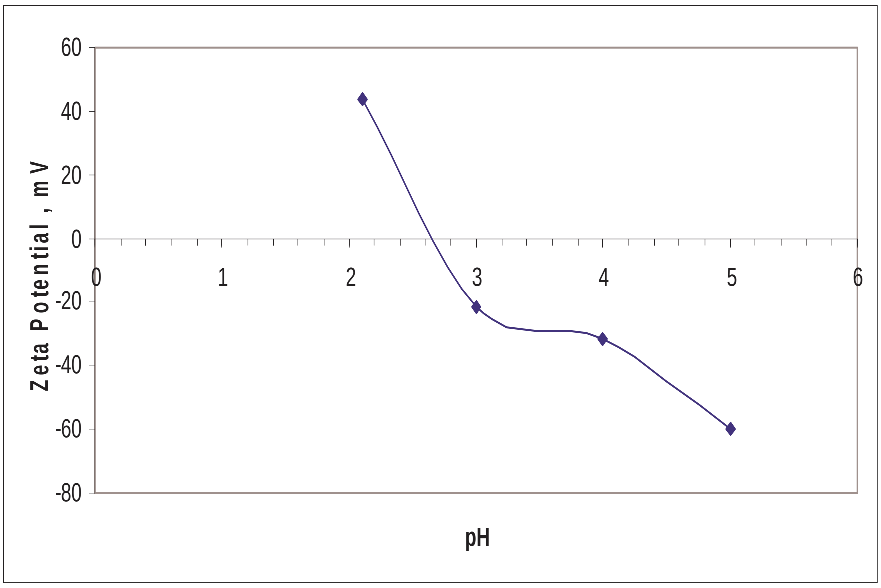

Figure 7.45. Zeta potential of the glass powder in 10^{-3} M KCl solutions.

7.2.2. Potentiometric Titration Experiments for Powders

Surface charge density and surface potential values for the oxides powders are determined by the well known method potentiometric titrations. In our titration tests, the uptake of acid or base by a suspension of the powders of used in this study was measured and compared with the uptake of acid or base by a reference solution of equivalent volume. The difference in the amounts of titrant necessary to produce the same pH value in the suspension and in the reference solution is attributed to adsorption or desorption of protons onto the solid surface.

A sample potentiometric titration experiment result is shown in Figure 7.46. This data is taken from the potentiometric titration experiment carried out with sample SO-01(2 g) under conditions 10^{-3} M KCl (100 mL) .

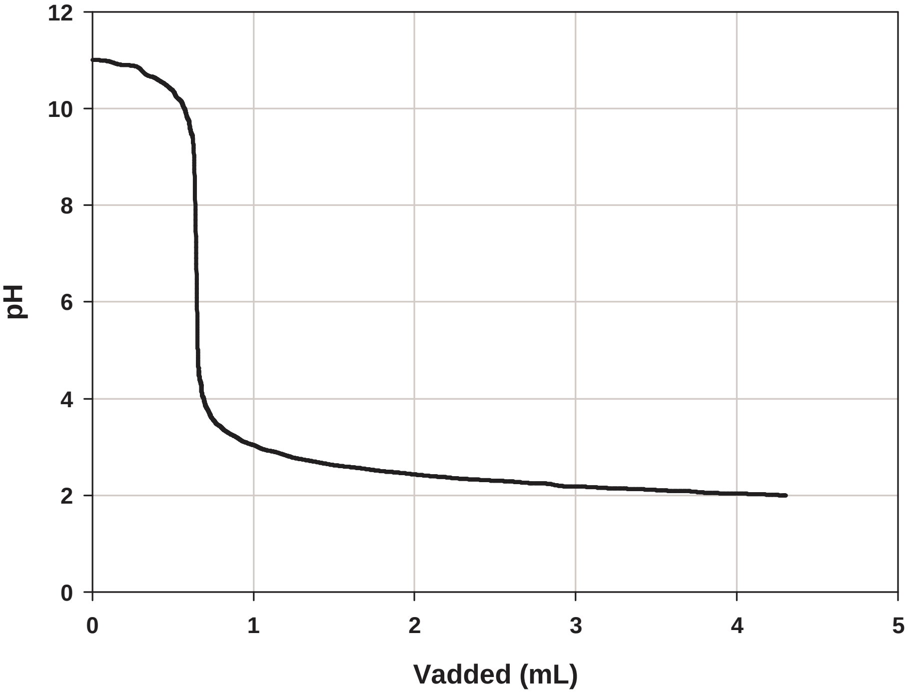

Figure. 7.46. Titration of a suspension of silica (SO-01) in 10^{-3} M KCl with 0.1M HCl and KOH.

The pH–added acid base concentration diagram are given in Figure 7.47, concentrations were calculated by Equation 5.5.

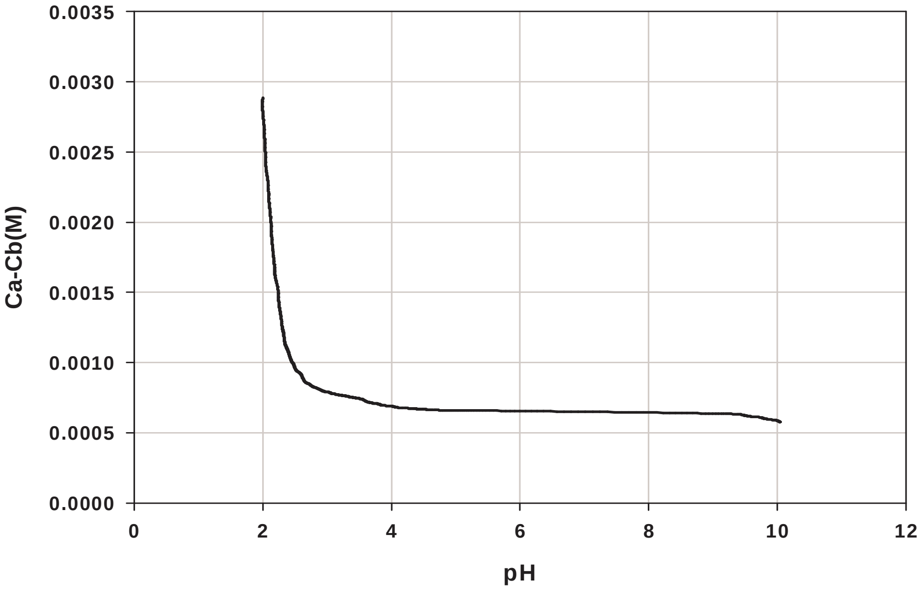

Figure 7.47. Concentration versus pH plot for SO-01 powder.

The mean surface charge (i.e., the portion of the charge due to OH^- or H^+) can be calculated as a function of pH from the difference between total added base or acid and the equilibrium OH^- or H^+ ion concentration for a given quantity a (kg/L) of oxide used by Equation 5.6, as shown in Figure 7.48.

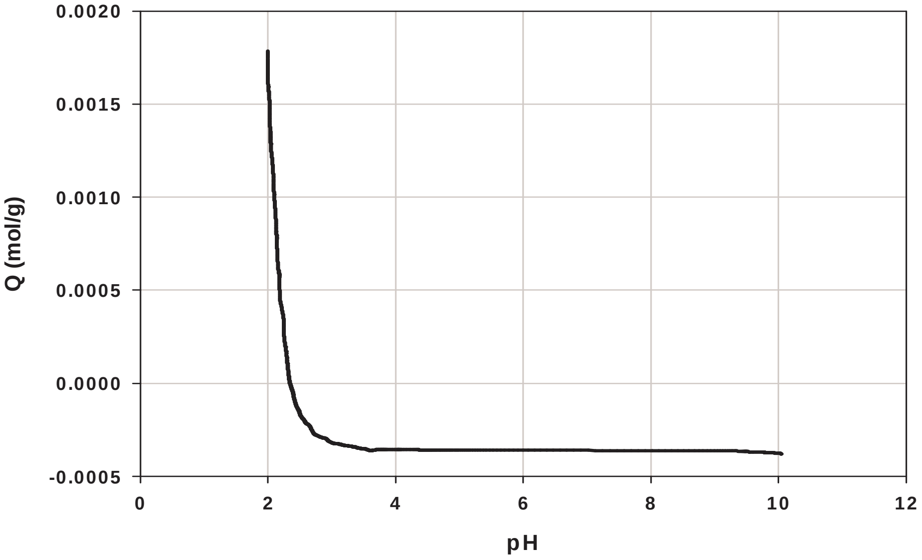

Figure 7.48. Charge calculated from the titration curve (charge balance).

If the specific surface area S (m^2/kg) of oxide used is known, the surface charge can be calculated using Equation 5.7, as shown in Figure 7.49.

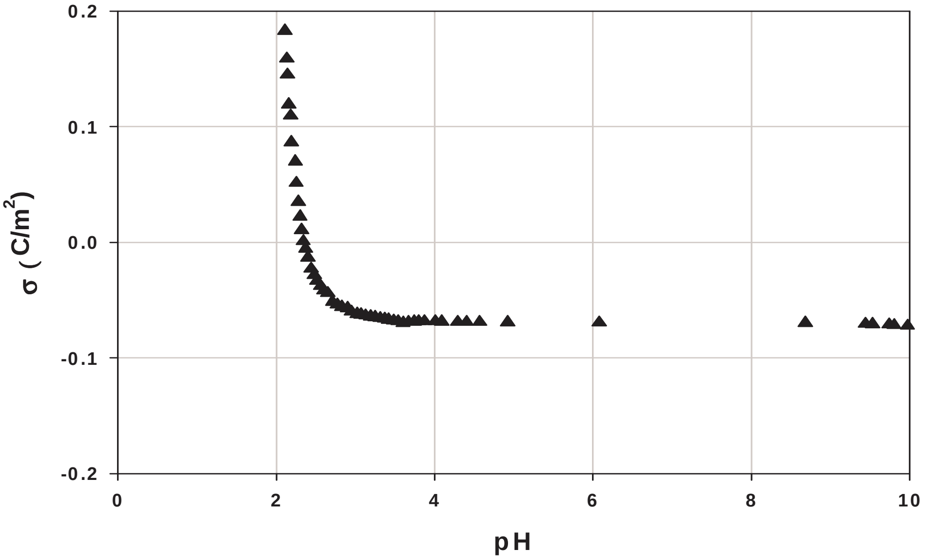

Figure 7.49. Surface charge density of silica SO-01**.**

Surface charge density (σ) is related to the potential at the surface (ψ) as Equation. 5.8.Surface potential versus pH graph were given in Figure 7.50.

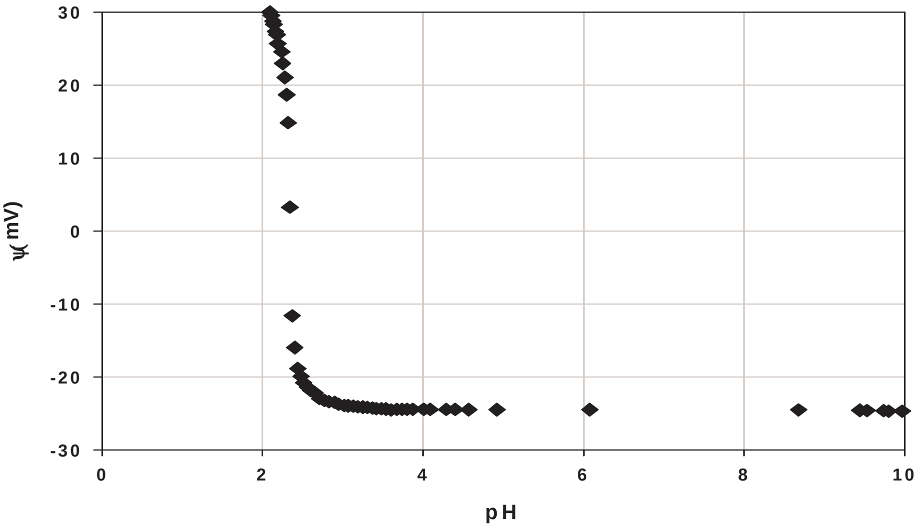

Figure 7.50. Surface potential of silica SO-01**.**

Surface acidity equilibrium constants were also calculated and found K_1=1.5 and K_2=3.2 for SO-01. If surface acidity equilibrium constants are known, the surface complexation of the system can be calculated according to main species of oxide system. Modeling of surface potential distribution for hydrated silicon dioxide was calculated and plotted according to surface species which was shown in Figure 7.51.

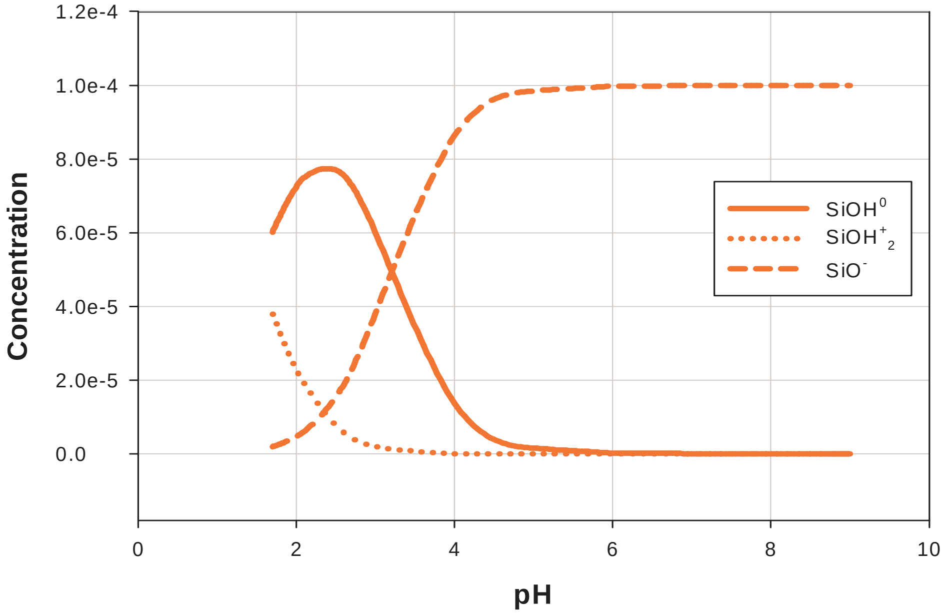

Figure 7.51. Surface complex formation of SO-01 at 10^{-3}M KCl.

For the silicon nitride and alumina powder detailed graphical representation given in Appendix B. Surface charge density and surface complexation of silicon nitride and alumina at various pH are shown in Figure 7.52- Figure 7.55.

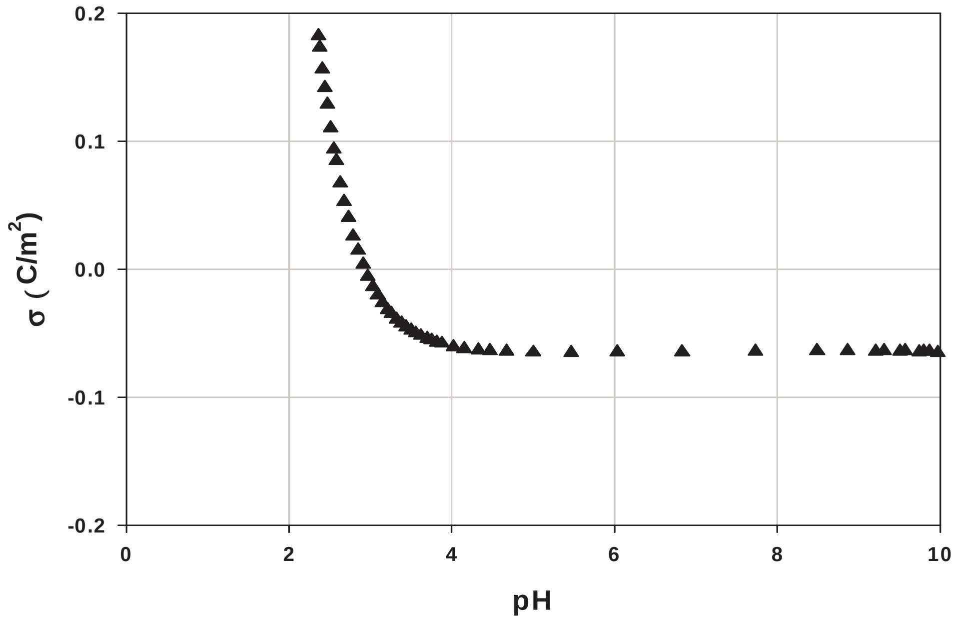

Figure 7.52. Surface charge density of SN.

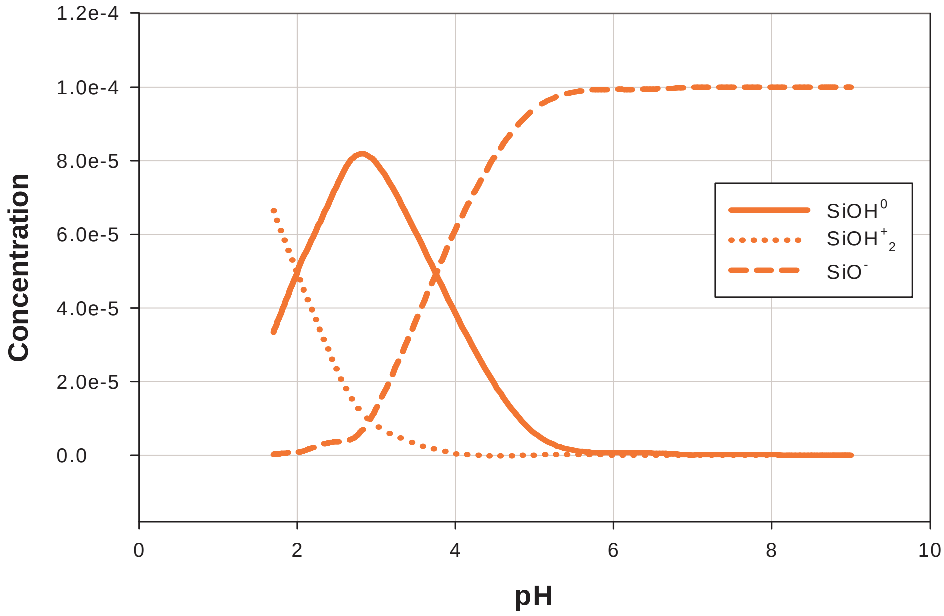

Figure 7.53. Surface complex formation of silicon nitride SN.

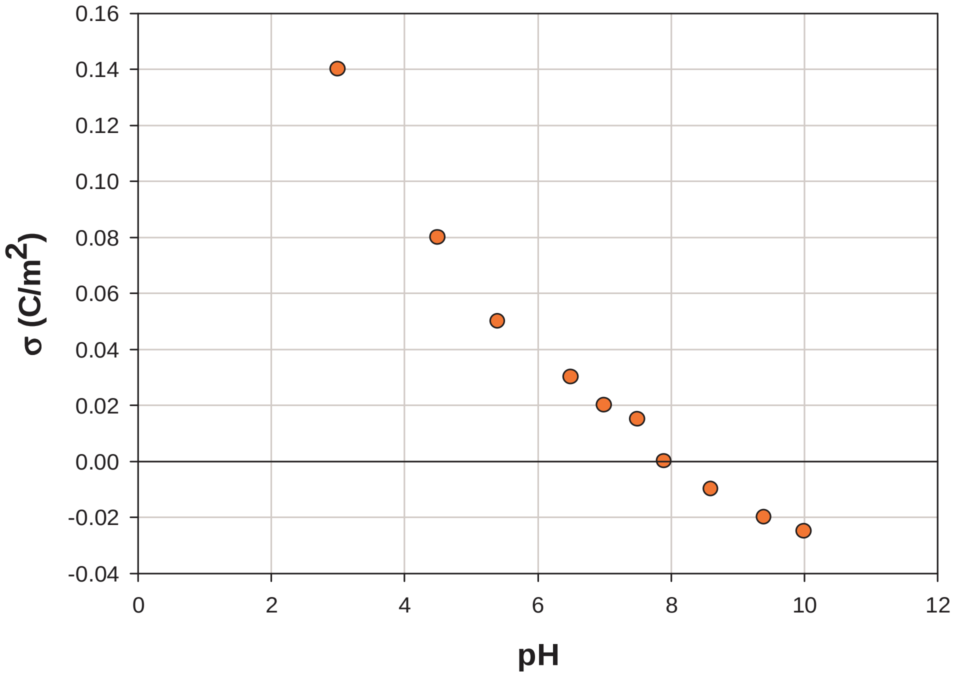

Figure 7.54. Surface charge density of AO-03.

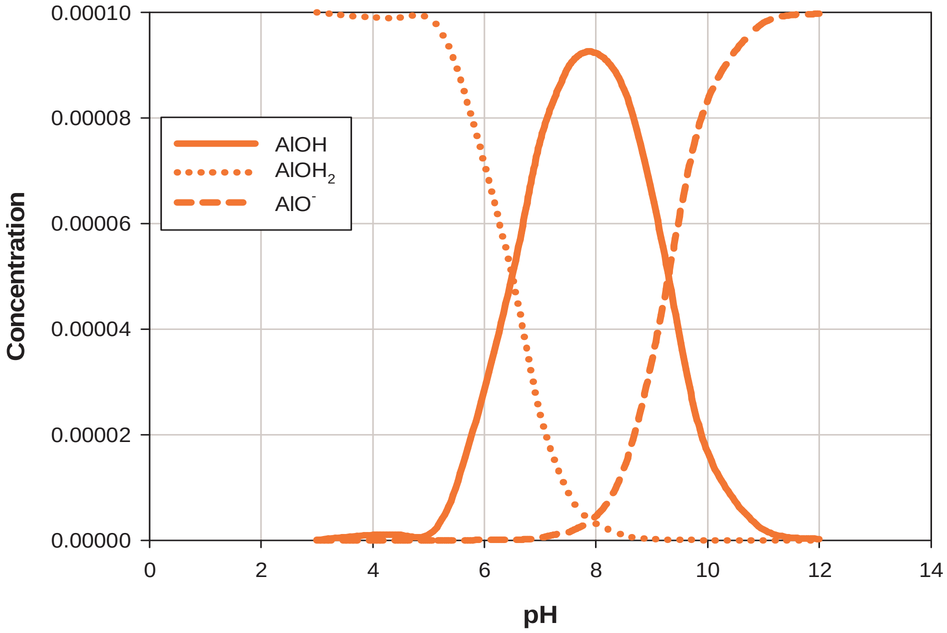

Figure 7.55. Surface complex formation of AO-03.

7.3. Measured and Theoretically Calculated Force –Distance Curves

The theoretical force calculations were carried out based on the DLVO theory assuming the net force of interaction (F_{net}) per unit area of the interacting plates was a sum of van der Waals and double layer forces. The force per area on any one of the plates (pressure force) due to the van der Waals component (F_{vdW}) is given by equation 2.8 whereas the force of electrostatic interaction is given by 2.15 The calculation of the electrostatic pressure force is carried out using the recent method developed by Polat and Polat (2010). The equation for the van der Waals component assumes that the interaction is in the non–retarded region which is not a bad assumption since the measured forces were mainly significant below about 10 nm.

The hamaker constant calculated for interaction of Si_3N_4 and Silica in KCl solution is A_{132} = 6.127 x10^{-21} J, and for Si_3N_4 and Alumina interacting in KCl solution is A_{132} = 2.166x10^{-20} J from the method given at Polat and Polat (2000-b).

A clear advantage of AFM compared with other techniques, such as pH–potentiometric titration routinely used for determination of surface potential, the surface force is almost unaffected by sample dissolution. This eliminates ambiguity introduced by a necessity to differentiate contributions made by dissolved and surface species unavoidable in treatment of titration data; the force measured in an AFM experiment is sensitive to the surface species only. Sometimes, this may shed new light on the properties of these species. The calculated force–distance– pH surface fits very well to the experimental force–distance curves measured at different pHs. For a more detailed description of the computational procedure, was given in Chapter 6, section 6.4.4.

The aim of this part is to estimate the surface charge distribution from force data obtained with the AFM. Atomic force microscopy data were taken between oxide single crystal surface and silicon nitride probe at KCl electrolyte solution at a specific point on the surface. The raw data was transformed to force–distance curves, using constant potential and constant charge boundary conditions. The algorithm of these calculation is given in Chapter 6, section 6.4.4. Usually, the obtained results show good reproducibility and are in reasonable agreement with the literature data. The basic procedure in determining the surface potential is based on simultaneous comparison between experimental and calculated force–distance curves obtained at different pH values of the background solution by varying the surface potential until an optimum is found. In these calculations, we assumed that the silicon nitrate tip is sharp and the surface potential of the tip does not change at a given pH. As a result the surface charge of oxide surface was found from this optimum potential at that point on the surface explained above and applicable any local area of our surface. The same procedure was applied to multiple points on the surface to obtain a surface charge distribution of the substrate. These potential was taken after many AFM experiments and comparison between these AFM result with theoretical calculation as Constant Potential and Constant Charge surface at different pH ranges.

In this section, experimental by obtained reading and theoretical calculations of force interaction between glass, quartz or alumina (sapphire) substrates and Si_3N_4 tips in aqueous media at various pHs are presented. The surface potential of silicon nitride probe was taken as + 60 mV for pH 2, 50 mV for pH 6 and -60 mV for pH 10. As stated above, the surface potential of the substrate at the poin5 of measurement was obtained by fitting the measured data to the theoretical force predicted for the environmental conditions employed.

The results of the normal force measurements with an Si_3N_4 probe and the glass surface are given in Figures 7.56, 7.57 and 7.58 as a function of separation for pH values of 2, 6, and 10 respectively. The reason for choosing these specific pH values is as follows: at pH 2, both the glass and the silicon nitride should be positively charged, since pH 2 is below the ieps of both solids but both solid ieps are between pH 2–3 according to zeta potential measurements. At pH 6 glass surface was negatively charged and silicon nitride surface was positively charge. Conversely, both surfaces must be negatively charged at pH 10. Therefore, besides the attractive van der Walls forces, the surfaces should feel an electrostatic repulsion at pH values of 2, and 10. The solid line and dash line represent the constant–charge and constant–potential scenarios, respectively. The parameters employed in computing these curves are given below the figure title. . The surface potential of silicon nitride probe was taken as + 60 mV for pH 2, 50 mV for pH 6 and -60 mV for pH 10. Correct calculation method of surface charge should be realized, before founding the correct charge at substrate surface. Glass substares were used to settle down the methodology both for AFM measurements and computer program.

The normal force measurements and their comparison with the DLVO theory show that the interaction between glass surface and silicon nitride tip are solely governed by electrostatic forces in Figure 7.56. Silicon nitride probe surface potential was taken 60 mV at pH 2 then calculated the glass substrate surface charge was found 40 mV at measured point of the substrate.

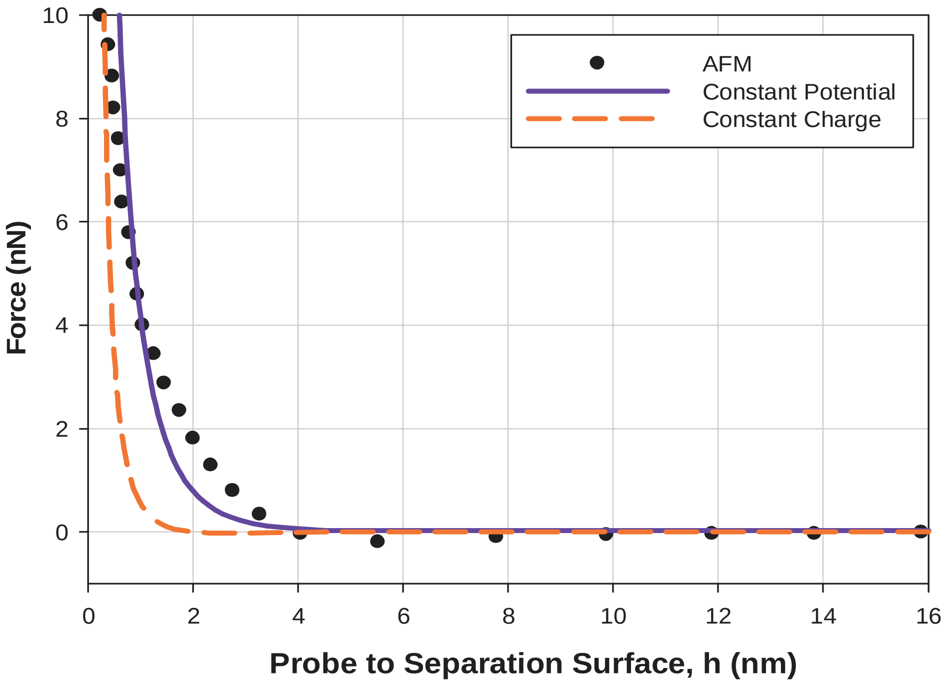

Figure 7.56. Force versus distance curves measured at 10^{-3} M KCl with a silicon nitrite tip on glass at pH 2 (ψ_{Si3N4}=+60 mV, ψ_{glass}=+40 mV).

Results of AFM experiments conducted at pH 6 are shown in Figure 7.57. If one surfaces are negatively charged and other positively charged, the long range interaction between the tip and glass surface should attractive The AFM experiment agree with the theory especially the AFM data clearly lie closer to the constant charge limit, but close separation the theory and experiment was disagree. In literature attributed to the possibility of surface hydration (Ducker et al., 1991).

The experimental force curve was taken at pH 10 with salt concentration 10^{-3} M in Figure 7.58. The AFM experiment and theoretical curves also show the repulsive curves both constant potential and constant charge case. The AFM experiment have good agreement with the theory especially the AFM data clearly lie in between constant potential and constant charge curves.

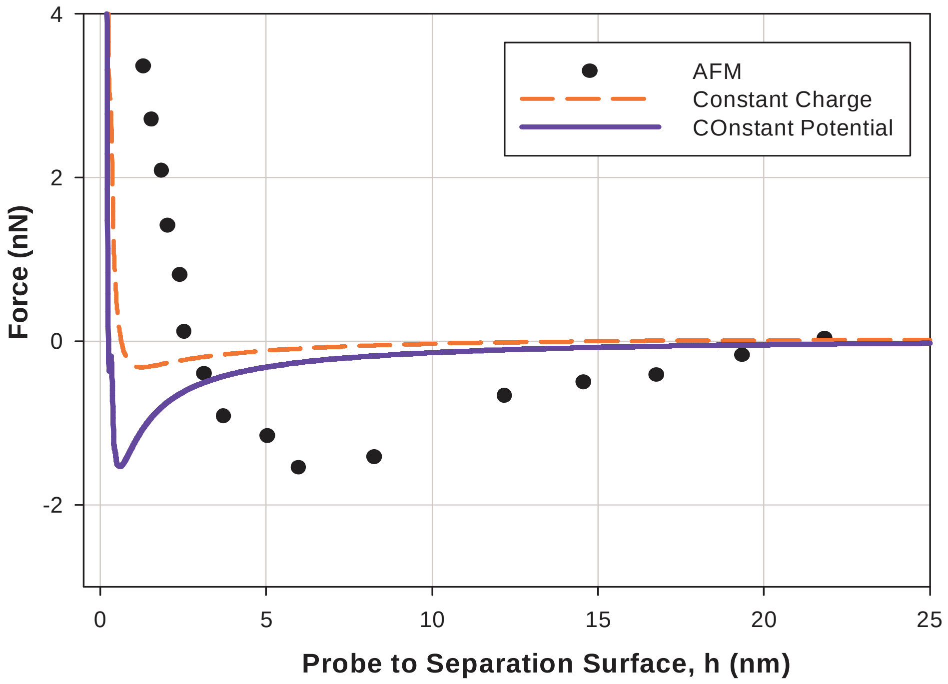

Figure 7.57. Force versus distance curves measured at 10^{-3} M KCl with a silicon nitrite tip on glass at pH 6 (ψ_{Si3N4}=+50 mV, ψ_{Glass}=10 mV).

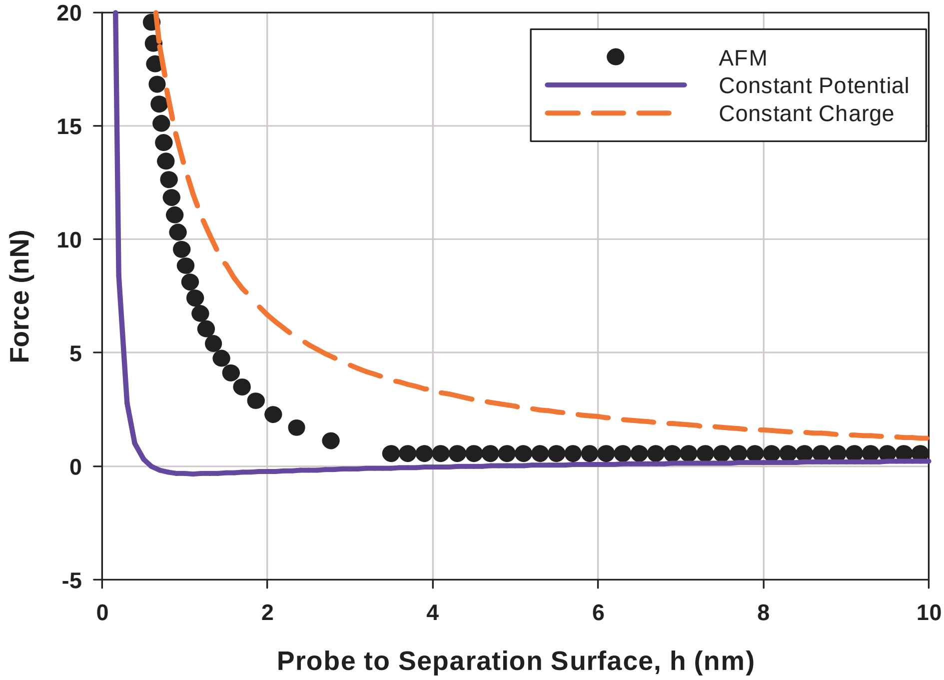

Figure 7.58. Force versus distance curves measured at 10^{-3} M KCl with a silicon nitrite tip on glass at pH 10 (ψ_{Si3N4}= -60 mV, ψ_{Quartz}= -100 mV).

Quartz and Sapphire surface charge distribution was determined for 10^{-3} M KCl solution for three different pH 2, 6, 10. The substrate was divided into three vertical regions to examine the surface charge distribution as shown in Figure 7.59. In these calculations, we assumed that the silicon nitrate tip is sharp and the surface potential of the tip does not change at a given pH. As a result the surface charge of oxide surface was found from this optimum potential at that point on the surface explained above and applicable any local area of our surface. The same procedure was applied to multiple points on the surface to obtain a surface charge distribution of the substrate.

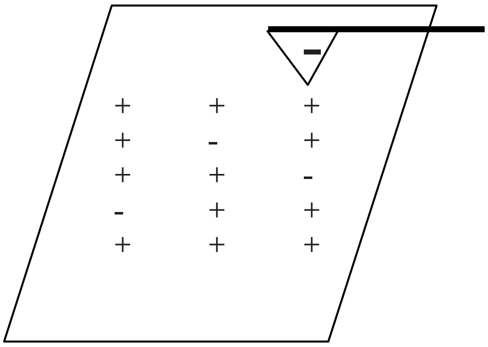

Figure 7.59. Schematic representation of estimation surface charge distribution of substrate by AFM.

The surface charge distribution of quartz (0001) and sapphire (0001) surface was determined by AFM by silcon nitride probe (R:5 nm) under 10^{-3} M KCl solution at various pH .

7.3.1. Determination of Surface Potential Distribution on a Quartz Substrate using Force data

Force separation curve of quartz (0001) surface and silicon nitride tip at pH 2 was shown in Figure 7.60. The AFM experiment and the theoretical curve also show the repulsive curves both constant potential and constant charged case. The AFM experiment have good agreement with the theory especially the AFM data clearly lie closer to the constant potential limit.

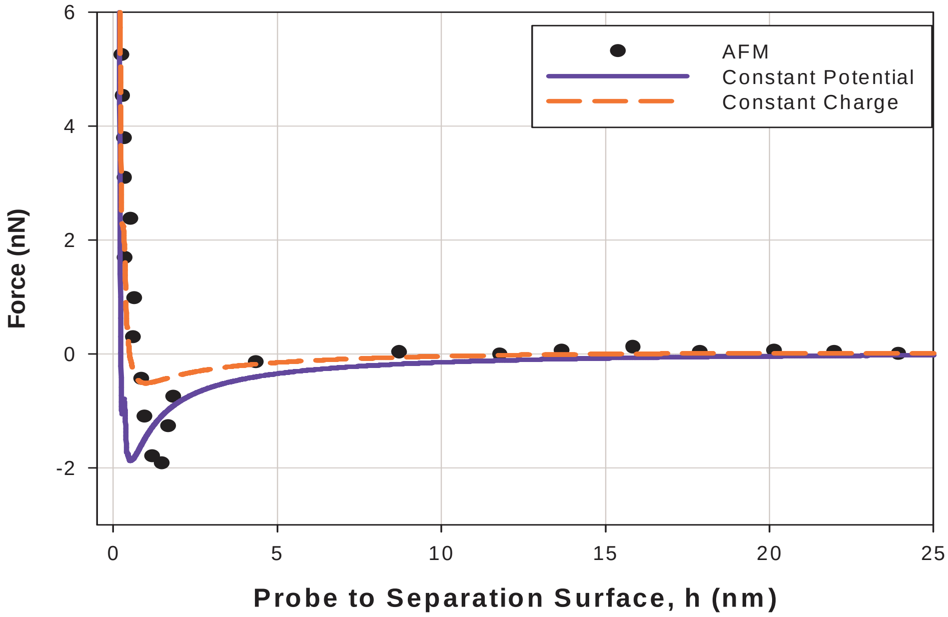

Figure 7.60. Force versus distance curves measured at 10^{-3} M KCl with a silicon nitrite tip on quartz (0001) at pH 2 (ψ_{Si3N4}=+60 mV, ψ_{Quartz}=+3 mV).

Silicon nitride probe surface charge was taken +60 mV at pH 2, and kept constant for all calculation at that pH. Then basic procedure was applied which is based on simultaneous comparison between experimental and calculated force–distance curves obtained at pH 2 of the KCl 10^{-3}M solution by varying the surface potential until an optimum is found as seen in Figure 7.61 and 7.62.

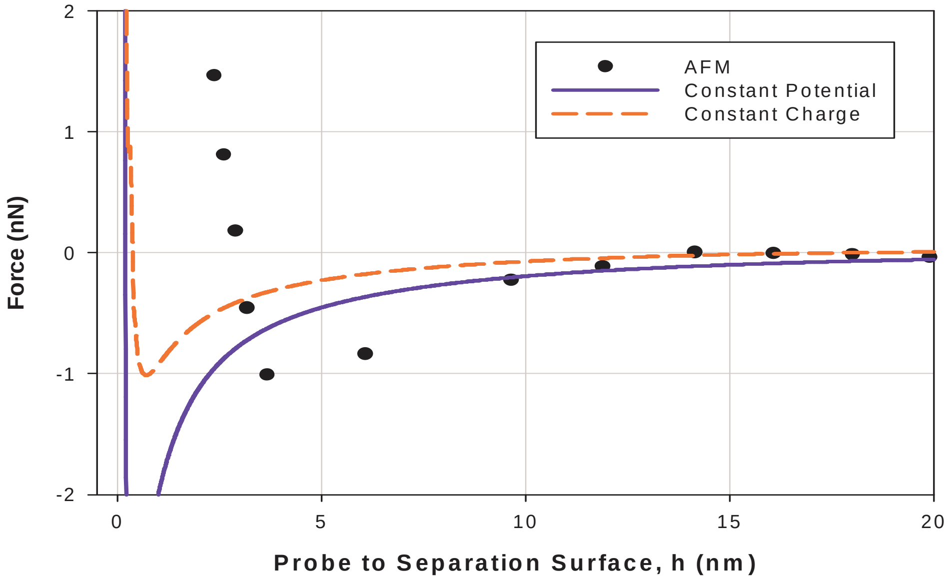

Figure 7.61. Force versus distance curves measured at 10^{-3} M KCl with a silicon nitrite tip on quartz (0001) at pH 2 (ψ_{Si3N4}=+60 mV, ψ_{Quartz}=-8 mV).

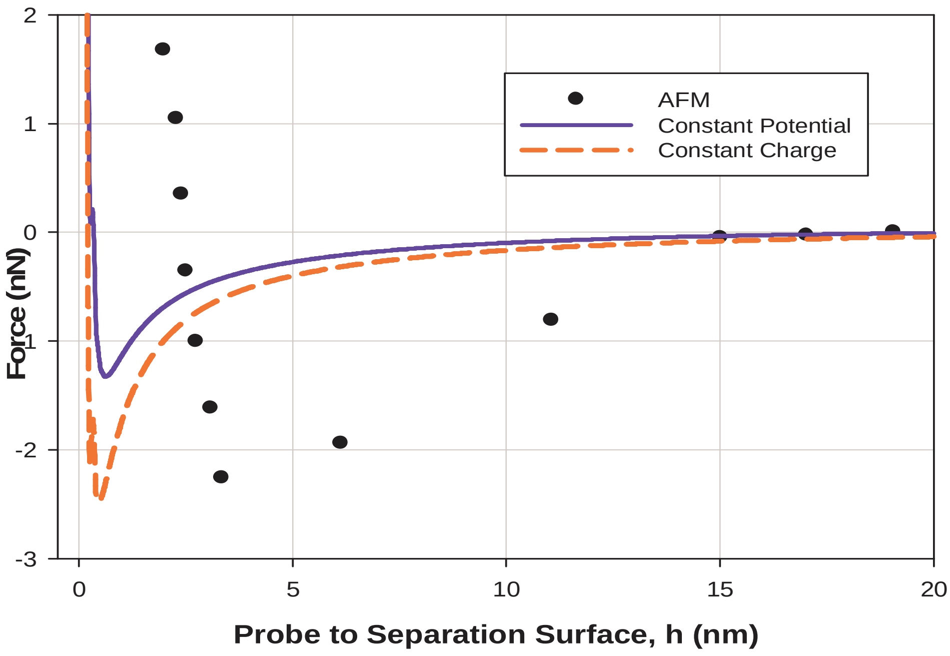

Figure 7.62. Force versus distance curves measured at 10^{-3} M KCl with a silicon nitrite tip on quartz (0001) at pH 2 (ψ_{Si3N4}=+60 mV, ψ_{Quartz}=+5 mV).

The surface charge distribution map of the quartz (0001) single crystal surface at pH2 was given in Figure 7.63. Charge distribution was changing between +0.10 Volt: -0.08 Volt of quartz at pH 2 as also was shown in Figure 7.63. There is a positive and negatively charged region at quartz surface because pH 2 is the point zero charge region of quartz. Zeta potential experiment results as seen between Figure 7.38–7.40 also have a good agreement with the AFM experiment results at pH 2, surface potential of that pH was around 0 mV. Surface charge distribution was calculated 30 mV, according to potentiometric titration results of quartz in Figure 7.50. If AFM measured surface potential data were compared to potentiometric titration data, the result is different. Potentiometric titration data were given only average surface potential but in AFM point analysis gave surface potential map of substrate as shown in Figure 7.63.

The force distance curve of quartz (0001) surface and silicon nitride tip at pH 6 was examined in Figure 7.64.

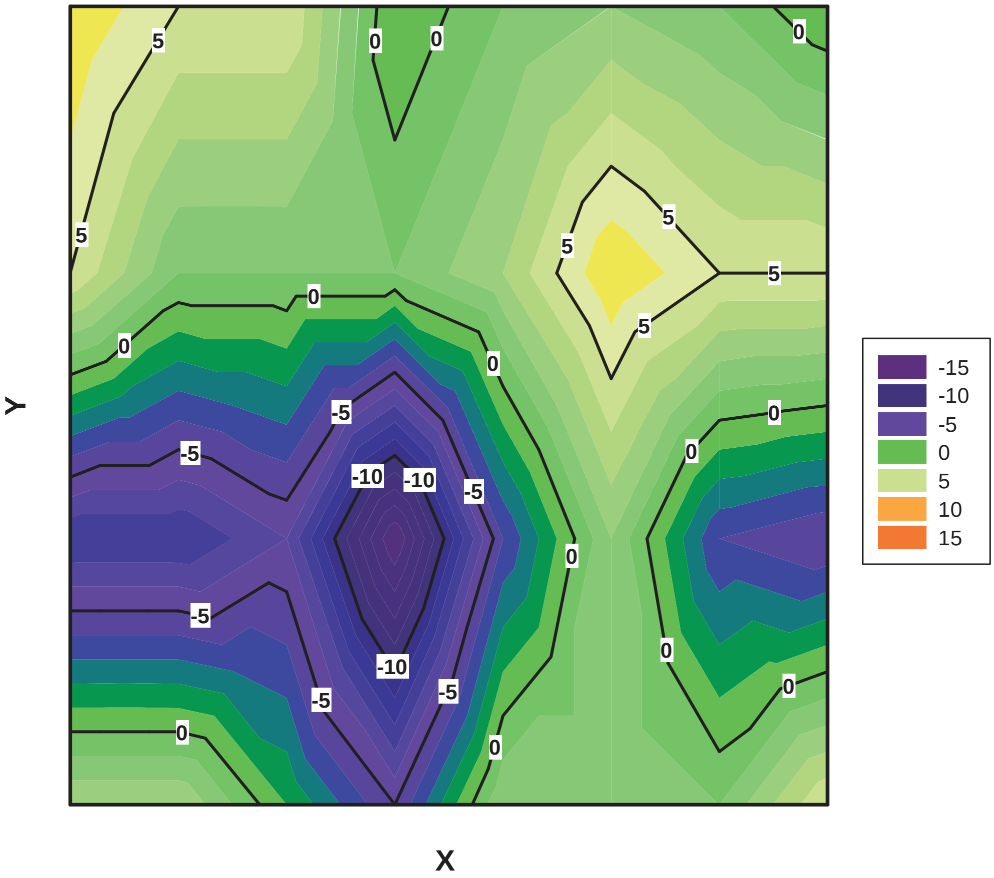

Figure 7.63. Surface charge distribution of quartz(0001) at KCl 10^{-3} M pH2, (ψ_{Si3N4}=60 m V).

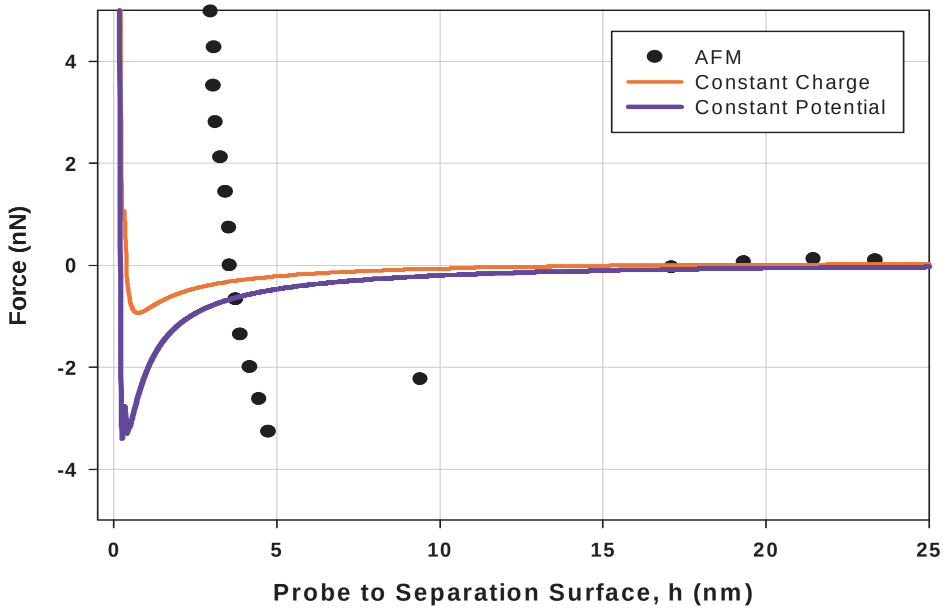

Figure 7.64. Force versus distance curves measured at 10^{-3} M KCl with a silicon nitride tip on quartz (0001) at pH 6 (ψ_{Si3N4}=+50 mV, ψ_{Quartz}=-9 mV).

In zeta potential measurement surface potential at pH 6 was calculated -40 mV (in Figure7.38–7.40) these results have a good agreement with the AFM experiment results. At pH 6 it was difficult to get AFM experiments. There was strong attraction between tip and surface as seen in Figure 7. 65, this cause after approaching the tip to the surface, it was difficult to retract tip from surface, to eliminate the attractive forces.

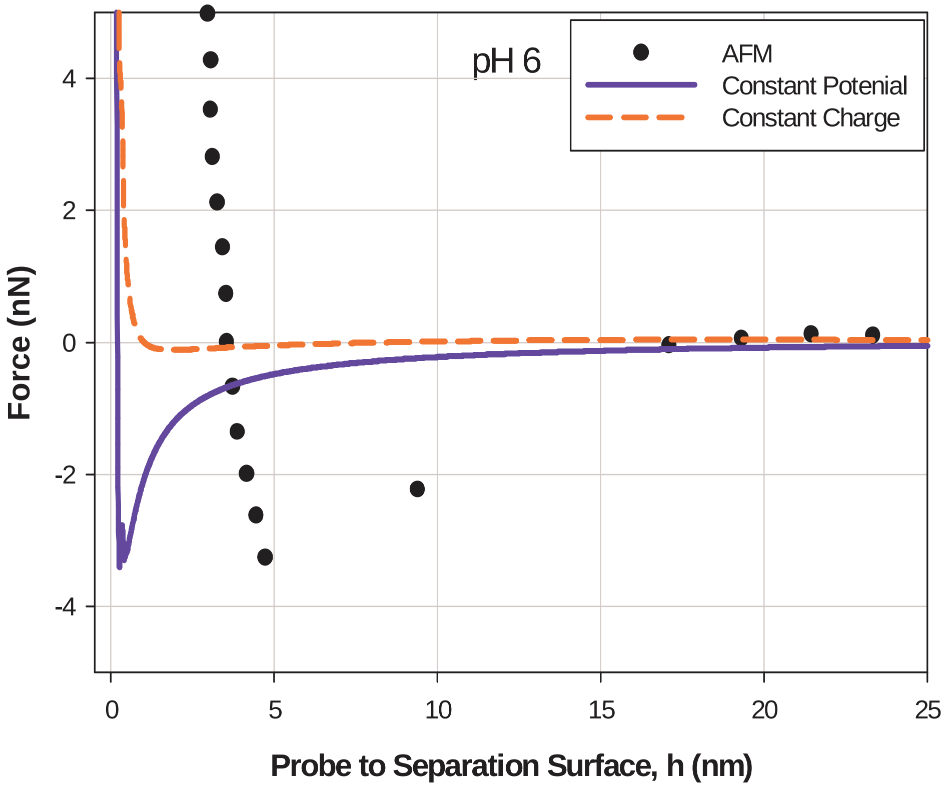

Figure 7.65. Force versus distance curves measured at 10^{-3} M KCl with a silicon nitrite tip on quartz (0001) at pH 6 (ψ_{Si3N4}=+50 mV, ψ_{Quartz}=-19 mV).

The surface charge distribution of quartz (0001) surface was examined by AFM by silicon nitride probe under 10^{-3} M KCl solution at pH 6. Silicon nitride probe surface charge was taken +0.05 Volt at pH 6. The surface charge distribution results of quartz at pH 6was shown in Figure 7.66. Charge distribution was changing between -0.009 Volt: -0.045 Volt as also shown in Figure 7.66. The average charge distribution was around -0.035 Volt.

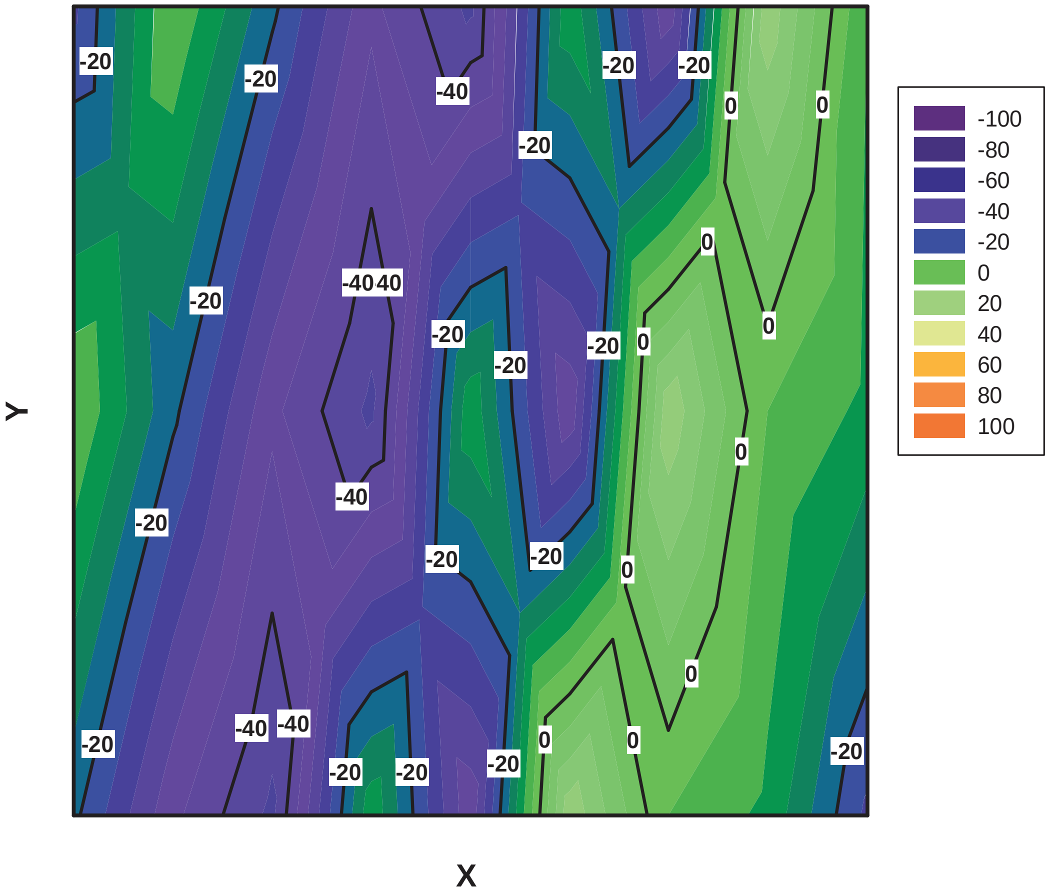

Figure 7.66. Surface charge distribution of quartz (0001) at KCl 10^{-3} M pH 6, (ψ_{Si3N4}=50 mV).

The surface charge distribution of quartz (0001) surface was examined by AFM by silicon nitride probe under 10^{-3} M KCl solution at pH 10. Silicon nitride probe surface charge was taken -0.060 Volt at pH 10, and kept constant for all calculation at that pH. There was strong repulsion between tip and surface as seen in Figure 7.67 and 7.68.

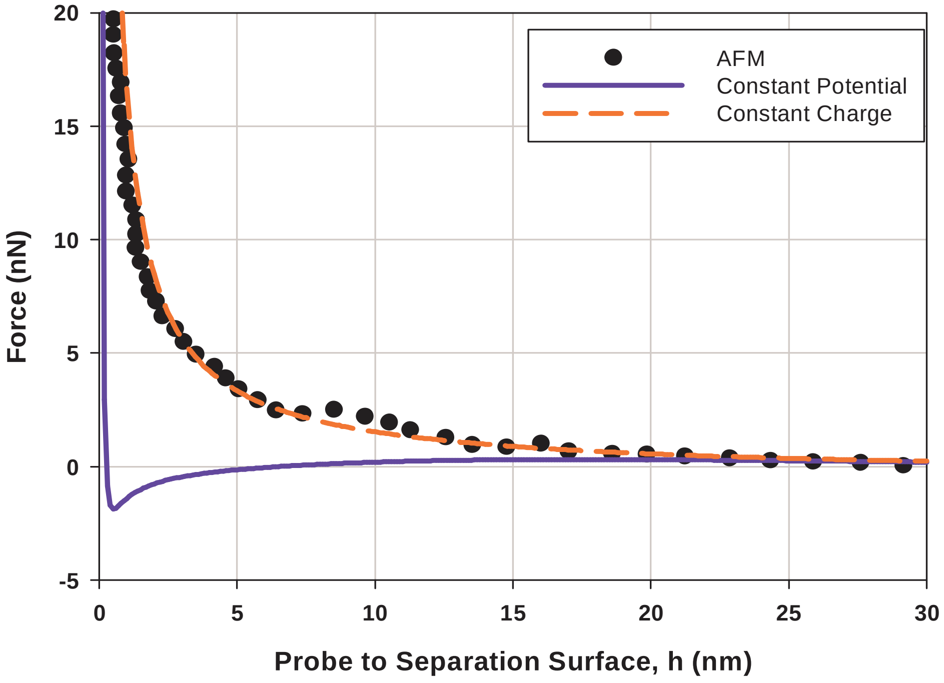

Figure 7.67. Force versus distance curves measured at 10^{-3} M KCl with a silicon nitrite tip on quartz at pH 10 (ψ_{Si3N4}= -60 mV, ψ_{Quartz}= -120 mV).

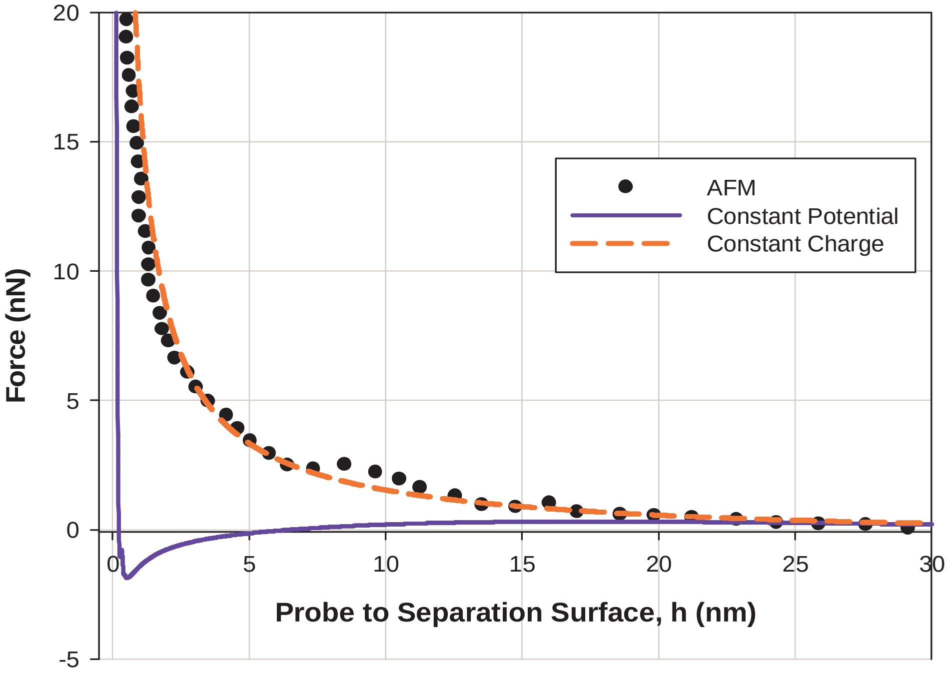

Figure 7.68. Force versus distance curves measured at 10^{-3} M KCl with a silicon nitrite tip on quartz (0001) at pH 10 (ψ_{Si3N4}=-60 mV, ψ_{Quartz}=-100 mV).

Charge distribution was changing between 0 mV: -120 mV as also shown in Figure 7.69. In zeta potential measurement surface potential at pH 10 was between -60: -80 mV, (in Figure7.40 –7. 38). The AFM surface potential values were changing between -100 mV and -120 mV. Larson et al. (1997) showed that silica particle surface potential was measured between -60: -120 mV at pH 10. The literature and AFM results were good agreement.

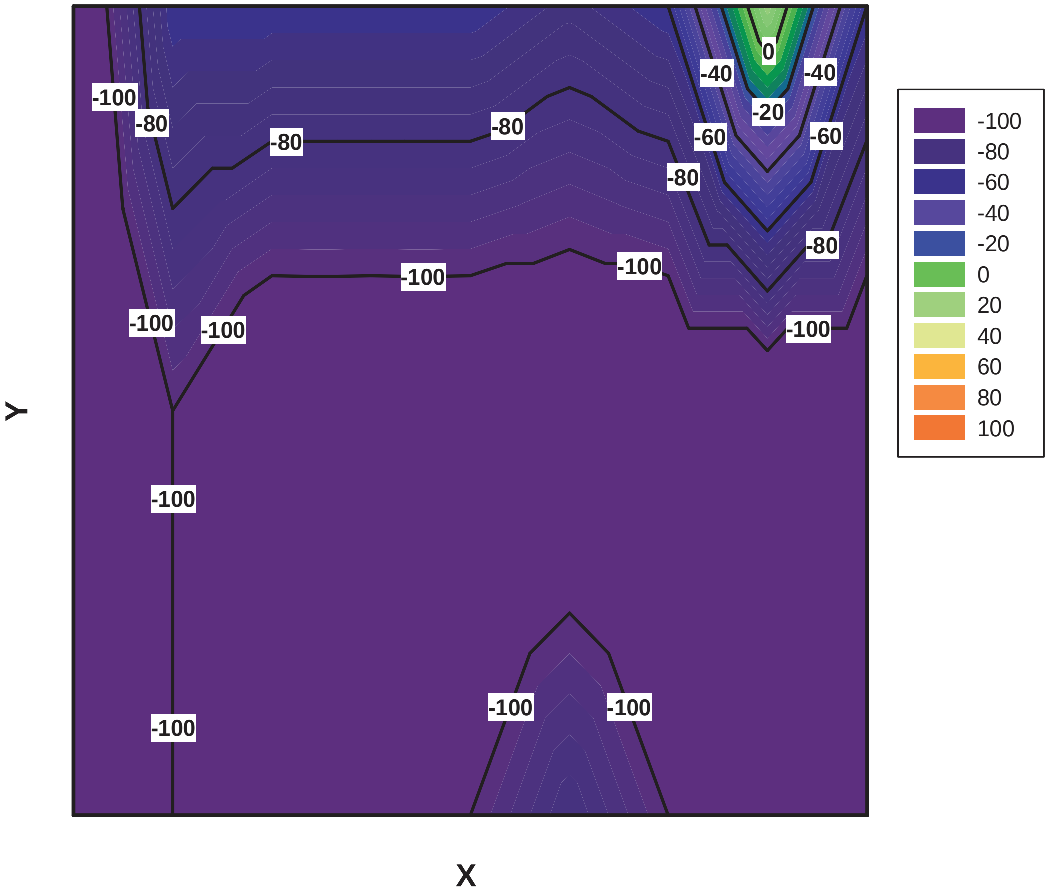

Figure 7.69. Surface charge distribution of quartz (0001) at KCl 10^{-3} M pH 10, (ψ_{Si3N4}=-60 mV).

7.3.2. Determination of Surface Potential Distribution on a Sapphire Substrate using Force data

Sapphire (0001) substrate surface potential distribution was also calculated same techniques as quartz. Silicon nitride tip surface potential values were not changed at pH 2, 6, 10 because tip and aqueous solution was not changed.

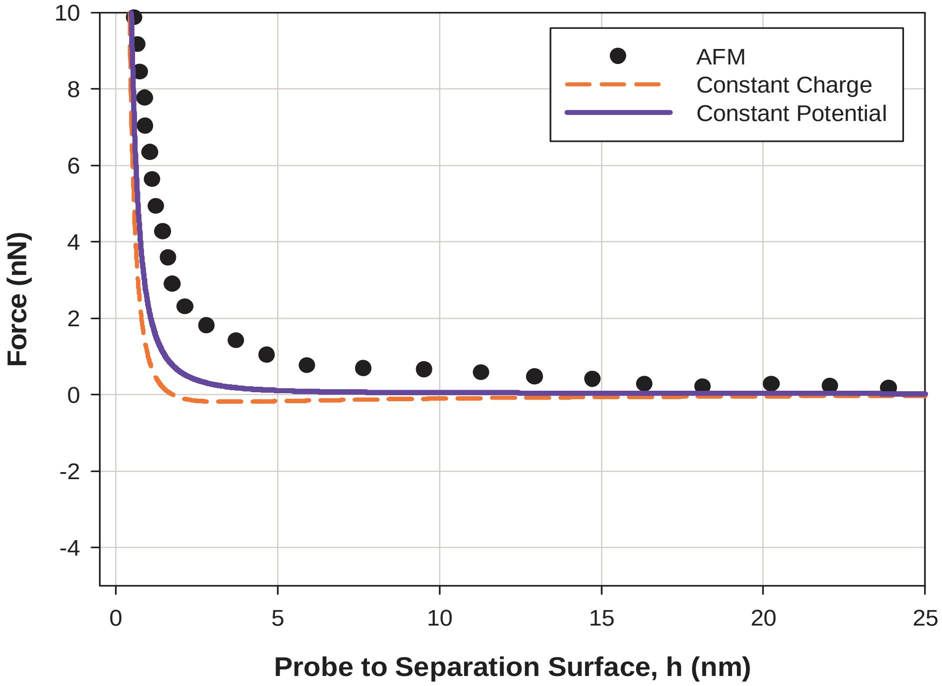

Figure 7.70. Force versus distance curves measured at 10^{-3} M KCl with a silicon nitrite tip on sapphire (0001) at pH 2 (ψ_{Si3N4}=+60 mV, $\psi_{Sapphire}$=+40 mV).

Results of AFM experiments conducted at pH 2 are shown in Figure 7.70 for sapphire (0001) substrate surface and silicon nitrate tip. If both surfaces are positively charged the long range interaction between the tip and glass surface should repulsive. The AFM experiment and the theoretical curve also show the repulsive curves both constant potential and constant charged case. The AFM experiment has good agreement with the theory.

The basic procedure is based on simultaneous comparison between experimental and calculated force–distance curves obtained at pH 2 of the KCl 10^{-3}M solution by varying the surface potential until an optimum is found as seen in Figure 7.71.

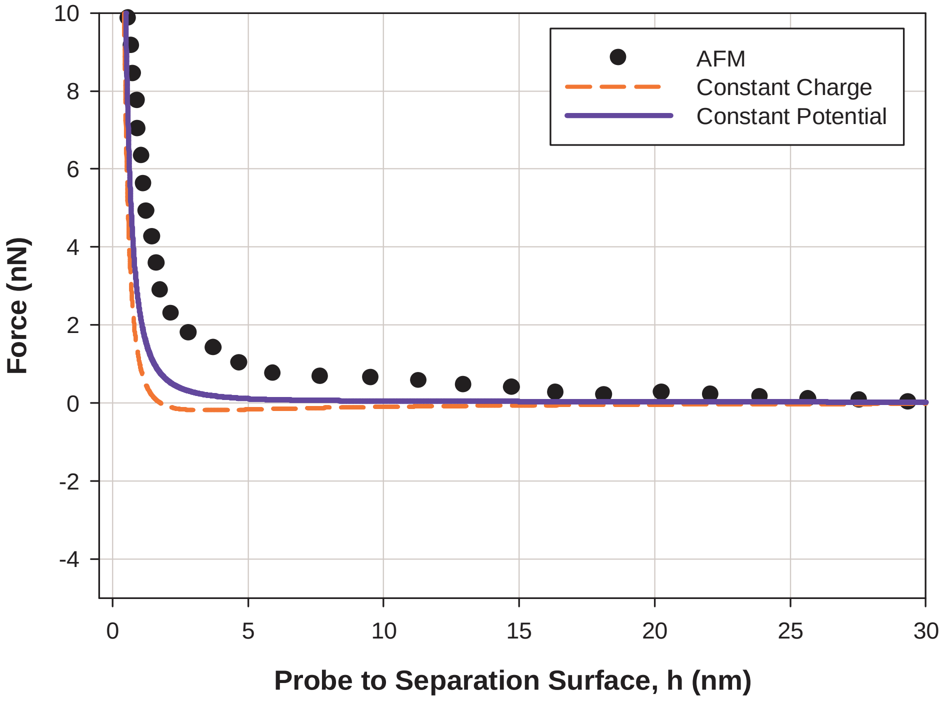

Figure 7.71. Force versus distance curves measured at 10^{-3} M KCl with a silicon nitrite tip on sapphire (0001) at pH 2 (ψ_{Si3N4}=+60 mV, $\psi_{Sapphire}$=+45 mV).

Polat et al. (2006) showed that for strongly basic solutions, the behavior of the alumina surfaces is profoundly different. The interaction is always repulsive, especially at separations below 7 nm, most probably due to the hydration of the oxide surface. The data suggest that the hydration layer acts as a repulsive barrier at separations closer than 10 nm.

Nowostawska et al. (2007) reveals that some alumina colloids display unusual high stability in the predictions of the DLVO theory, which is thought to be result of the formation of a gel layer of Keggin ions $Al_{13}O_4(OH)_x^{31-x}$ On the surface of the alumina particles that creates a steric barrier that is not described by classical zeta potential. The surface charge distribution of sapphire (0001) surface was determined by AFM by silicon nitride probe (R: 5 nm) under 10^{-3} M KCl solution at pH 2. Silicon nitride probe surface charge was taken +60 mV at pH 2, and kept constant for all calculation at that pH. The AFM–derived surface potentials of sapphire at pH 2 are shown. Charge distribution was changing between +15 mV: + 45 mV as also showed in Figure 7.72. Zeta potential experiment results as seen between Figure 7.42–7.44 also have a good agreement with the AFM experiment results. According to potentiometric titration experiment results of alumina (Figure 7.54), surface charge distribution was calculated 30 mV. Franks and Meagher (2003) have used sapphire single crystals. The potential of (0001) sapphire surface was measured by streaming potential techniques between 30–60 mV.

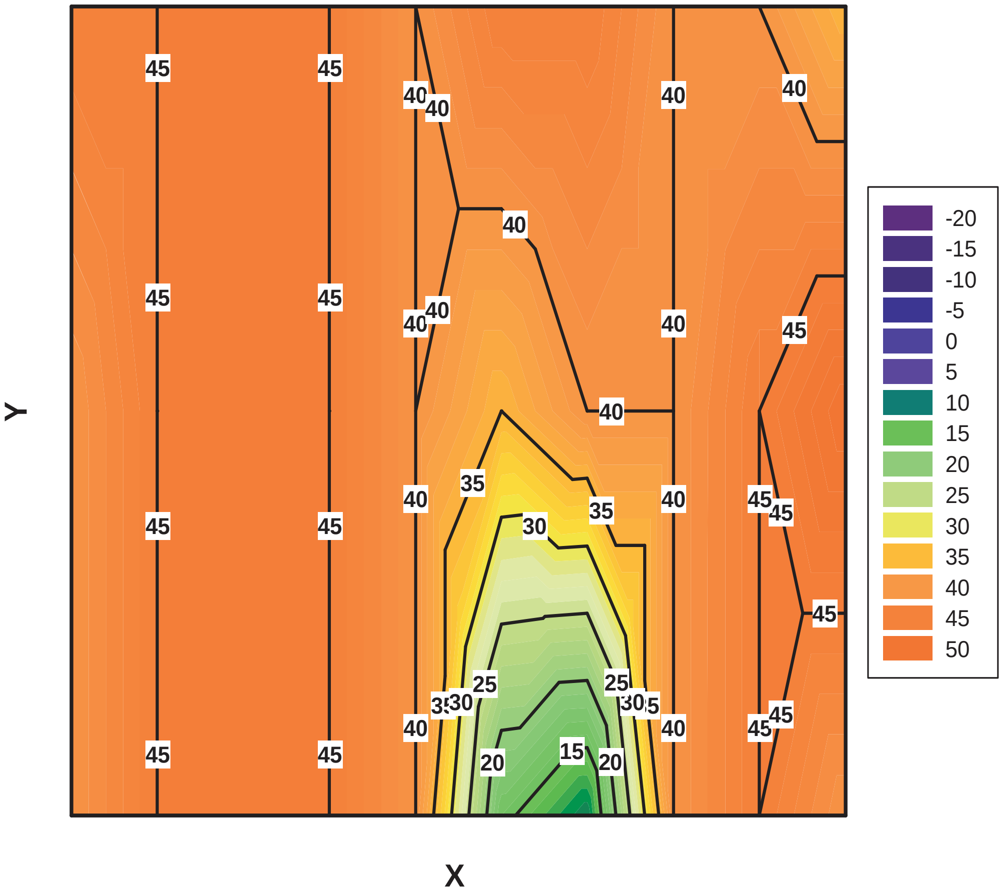

Figure 7.72. Surface charge distribution of sapphire (0001) at KCl 10^{-3} M pH2, (ψ_{Si3N4}=60 m V).

Force separation curves for sapphire (0001) substrate and silicon nitrate tip are shown in Figure 7.73. At pH 6 the alumina surface is positively charged, according to our zeta potential and potentiometric titration results. Most reports of the iep of sapphire tend to indicate much lower values than those obtained for powders. In many instances this lower iep has been unjustifiably silica contamination. Larson et al. (1997), took extreme care to avoid silica contamination and the amount of silicon on the surface before and after force measurements was characterized and no silica contamination was detected. Karaman and Pashley (1997) found the iep between an oxidized aluminum coated sphere and α–Alumina flat to be at pH 7. But in this work it was not clear that the α–alumina flat was polycrystalline or single crystal sapphire. Franks and Meagher (2003), measured isoelectric points of α–Alumina sapphire single crystals for four different crystallographic orientations; (0001), (1120), (1010), (1102). Both types of measure-ments indicated that the iep of sapphire single crystals between about 7 and 6. The powder α–Alumina was found 9.4, and they explained the difference between two types of α–Alumina is attributed to the presence of different types of surface hydroxyl groups on the two different types of α–Alumina surfaces.

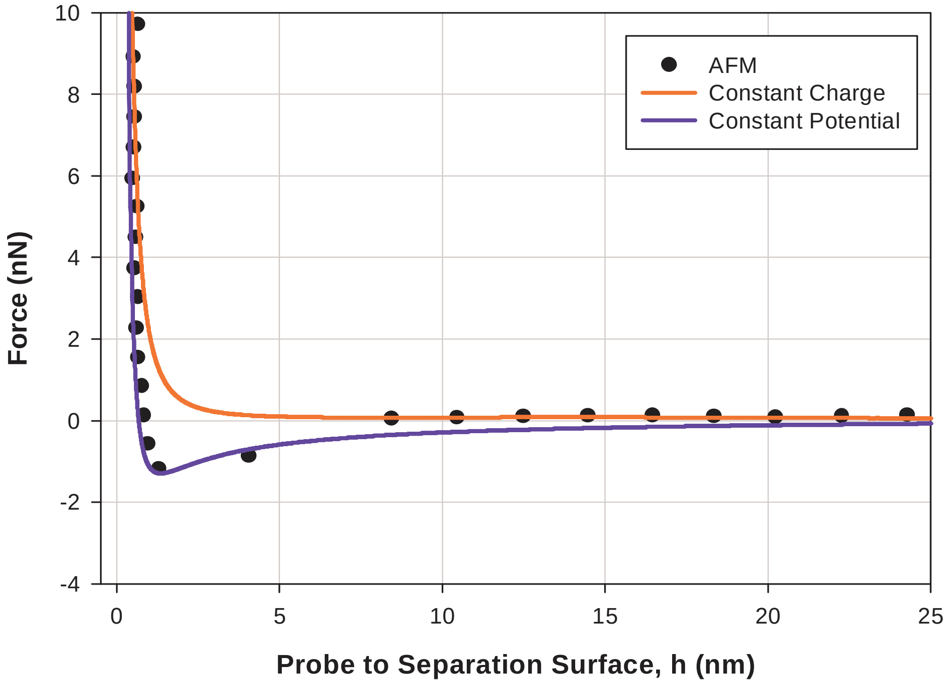

Figure 7.73. Force versus distance curves measured at 10^{-3} M KCl with a silicon nitrite tip on sapphire (0001) at pH 6 (ψ_{Si3N4}=+50 mV, $\psi_{Sapphire}$=-20 mV).

Also the silicon nitrate tip is negatively charged according to our zeta potential measurements (iep=3). In literature powder silicon nitride both α and β phases, iep found between pH 3 and pH 9. Raiteri et al.(1998), found the pzc of silicon nitride tip (Microlevers, PSI, Sunnyvale,CA) 4.7. So silicon nitride tip pzc is really difficult to observed from powder form because of various pH range. It can be seen pzc of silicon nitride tip should measured by AFM according to solution which are used in the system.

Sapphire (0001) surface charge distribution of was examined by AFM by silcon nitride probe under 10^{-3} M KCl solution at pH 6. Silicon nitride probe surface charge was taken +0.05 Volt at pH 6. In Figure 7.75 was shown the surface charge distribution results of sapphire at pH6. Charge distribution was changing between -0.009 Volt: -0.045 Volt.

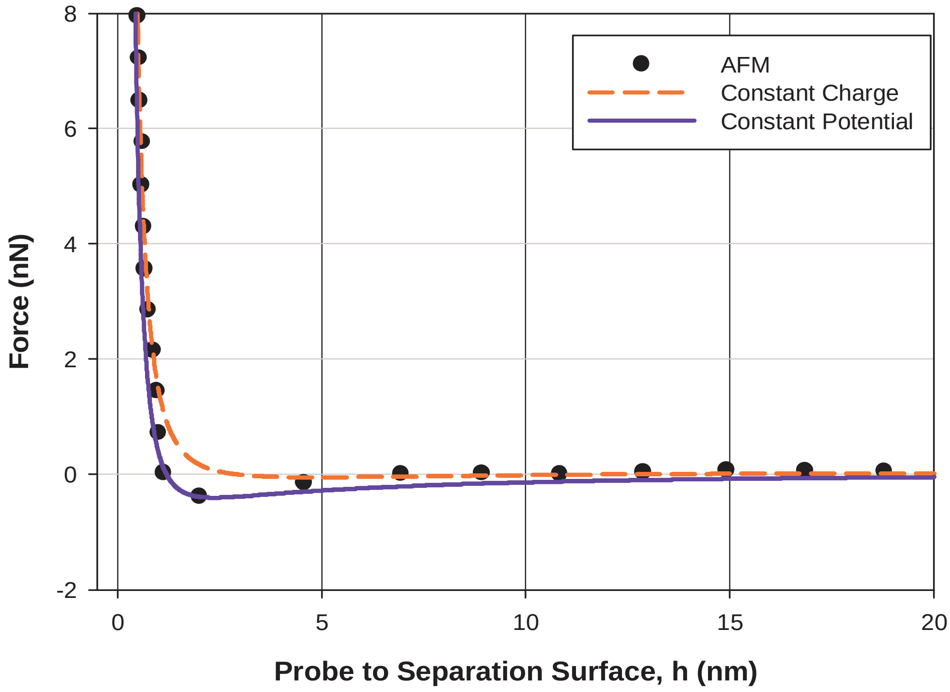

Figure 7.74. Force versus distance curves measured at 10^{-3} M KCl with a silicon nitrite tip on sapphire (0001) at pH 6 (ψSi3N4=+50 mV, ψSapphire=-10 mV).

Potentiometric titration experiment results of sapphire were given in Figure 7.75, surface charge distribution was calculated 20 mV at pH6 for alumina powder. AFM results were seen in. Figure 7.75, the average charge distribution around -30 mV. In zeta potential measurement surface potential at pH 6 was calculated +20 mV, (in Figure7.42-7.44). Zeta potential and potentiometric titration experiment were done by powder from of alumina but in AFM experiment were performed single crystal form of alumina. Franks and Meagher (2003) were explained that the different surface potentials of powders and single crystal form of alumina was due to the different types of surface hydroxyl groups with differing reactivity to acid and base. And also shape of powder and well-ordered single crystal was completely different so this also because different reactive site on surface and different bond of surface hydroxyl groups.

According to Franks and Meagher (2003), single crystal sapphire (0001) surface potential at pH 6 was measured by streaming potential between -10 mV: - 40 mV, depending of the electrolyte solution. In our AFM results were good agreement with their streaming potential data.

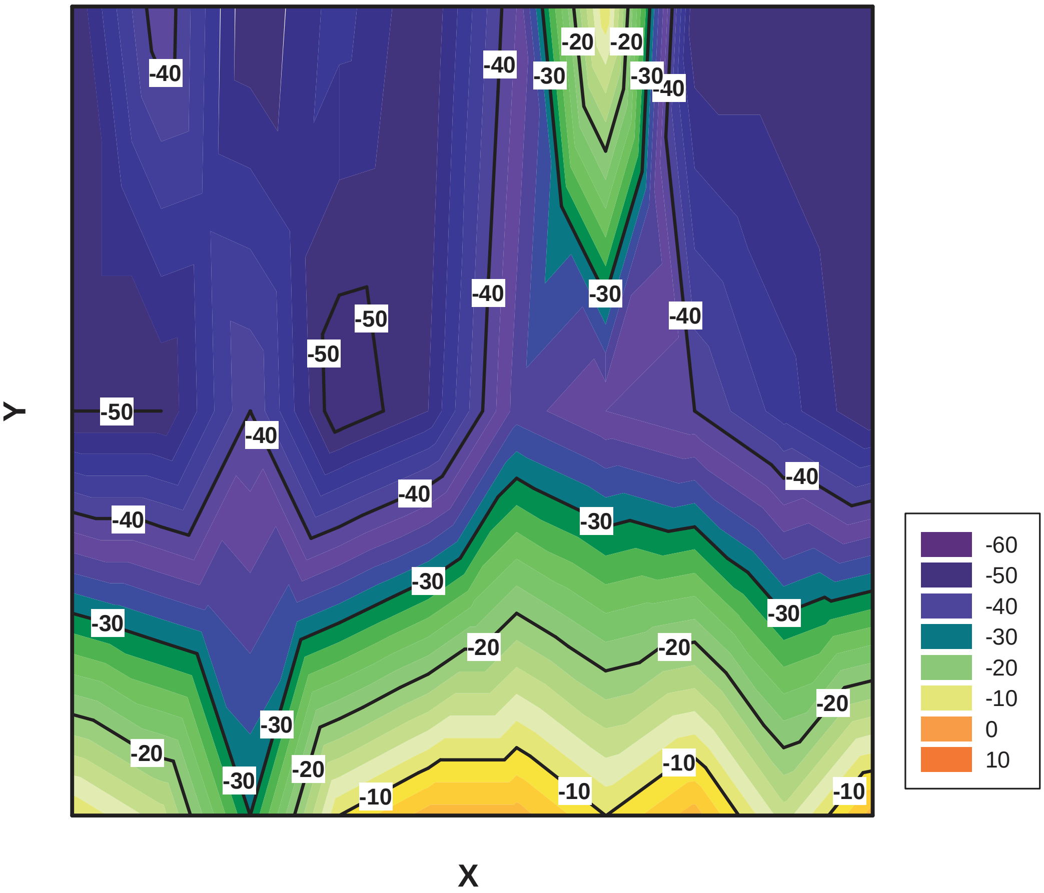

Figure 7.75. Surface charge distribution of sapphire (0001) at KCl 10^{-3} M pH 6, (ψ_{Si3N4}=50 m V).

There was repulsion between tip and surface as seen in Figure 7.76. Sapphire (0001) surface charge distribution of was examined by AFM with silicon nitride probe in 10^{-3} M KCl solution at pH 10. Silicon nitride probe surface charge was taken – 60 mV at pH 10.

There was strong repulsion between tip and surface also was determined in Figure 7. 77. AFM experimental result and theory has a good agreement, so we can find the correct surface potential of the surface.

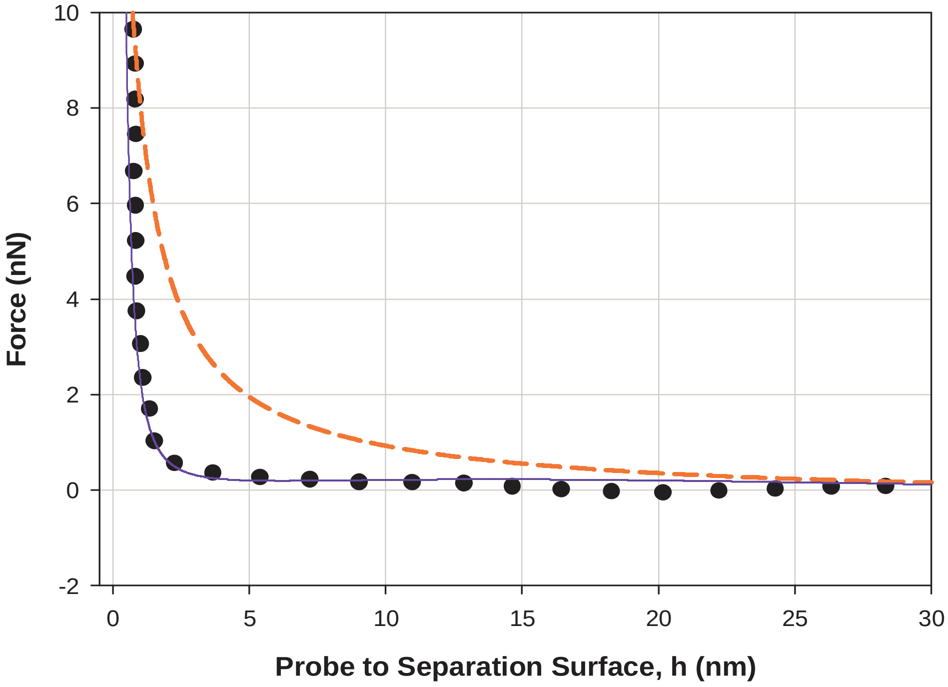

Figure 7.76. Surface charge distribution of sapphire (0001) at KCl 10^{-3} M pH 10, (ψ_{Si3N4}=-60 mV, $\psi_{Sapphire}$=-60 mV).

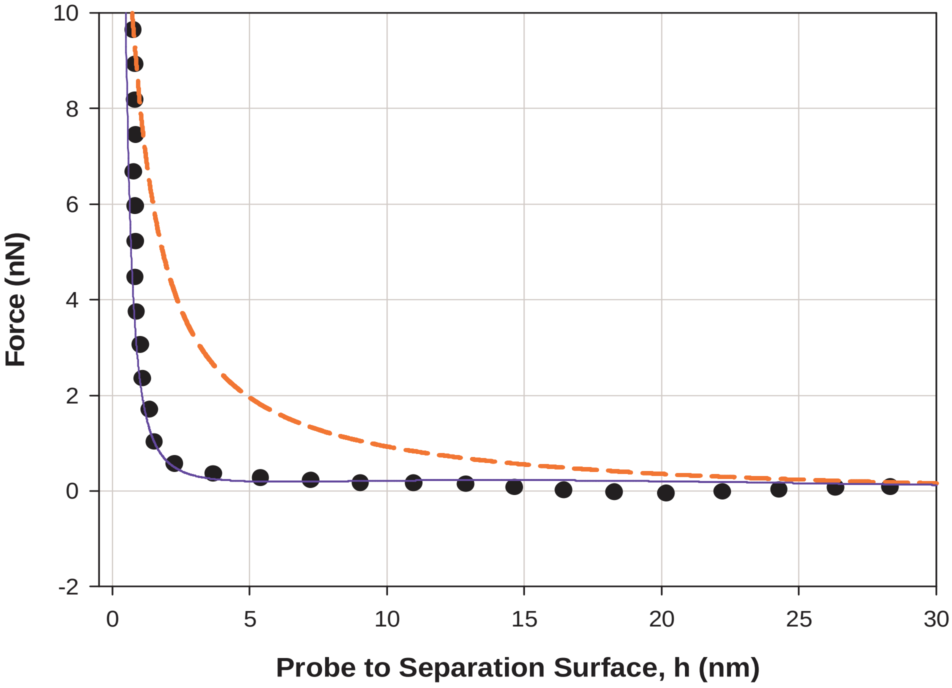

Figure 7. 77. Surface charge distribution of sapphire (0001) at KCl 10^{-3} M pH 10, (ψ_{Si3N4}=-60 mV, $\psi_{Sapphire}$=-65 mV).

In Figure 7.78 was shown the surface charge distribution results of sapphire. Charge distribution was changing between –50 mV: -65 mV as also shown in Figure 7.78. Zeta potential measurement and potentiometric titration result of powder alumina was not behaved like alumina single crystal. The result of surface potential by AFM and the other techniques were different.

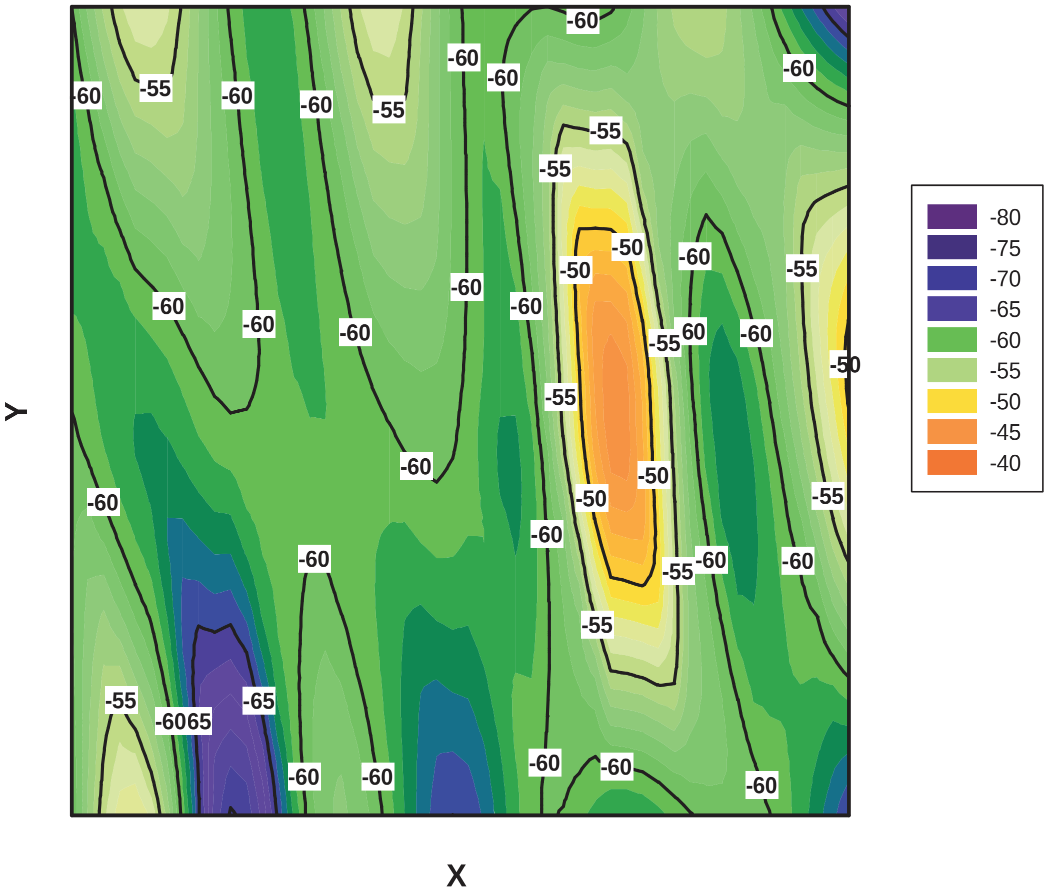

Figure 7.78. Surface charge distribution of sapphire (0001) at KCl 10^{-3} M pH 10, (ψ_{Si3N4}=60 m V).

Surface potential of quartz and sapphire single crystal substrates were measured by AFM with various pH in 10^{-3}M KCl as shown in Figure 7.79. Quartz single crystal pzc were measured pH 2 and sapphire single crystal pzc were evaluated around pH 4.5. Quartz single crystal pzc has a good agreement with quartz powder (SO-01, SO-02) pzc as shown in Figure 7.75, but SO-03 powder pzs has shown a little difference. This discrepancy could be explained by crystalline and amorphous silicon dioxide forms. SO-03 powder was measured by XRD as amorphous. The others SO-01, SO-02 and single crystal substrate were crystalline form of silicon dioxide. In literature search there weren't came across with quartz single crystal surface charge determination by any surface potential measuring techniques. Only quartz powder surface potentials were determined by many researchers which they were tabulated in Kosmulski (2001) pages 133-134.

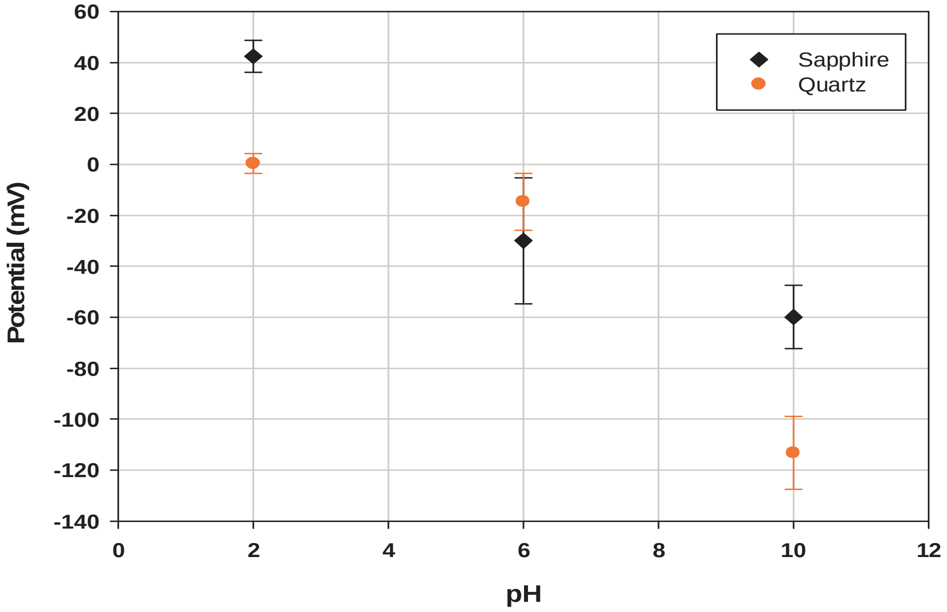

Figure 7.79. Surface potential of quartz and sapphire by AFM.

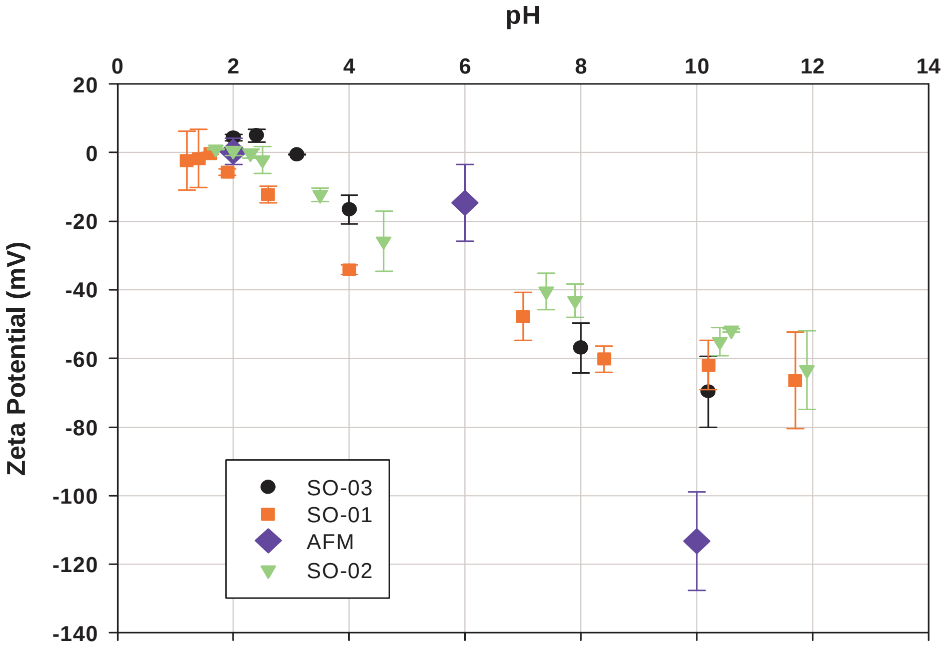

Figure 7.80. Surface potential of silica powder and quartz single crystal AFM.

AO-01, AO-02 and AO-03 powder pzc was shown good agreement with each other and also with literature (Kosmulski, 2001). Nevertheless sapphire single crystal has shown a little difference in pzc as shown in Figure 7.81. This discrepancy could be explained by crystalline and amorphous aluminum oxide forms. Franks and Meagher (2003) explained that the different surface potentials of powders and single crystal form of alumina was due to the different types of surface hydroxyl groups with differing reactivity to acid and base. And also shape of powder and well-ordered single crystal was completely different so this also because different reactive site on surface and different bond of surface hydroxyl groups. Franks and Meagher (2003) measured surface potential with various pH the sapphire single crystal substrate in (0001) orientation in 10^{-3}M KBr solution as shown in Figure 7.82. According to Figure 7.82 sapphire (0001) single crystal pzc was measured pH 4.9 by AFM., so this result in a good aggrement with literature data of single crystal sapphire pzc.

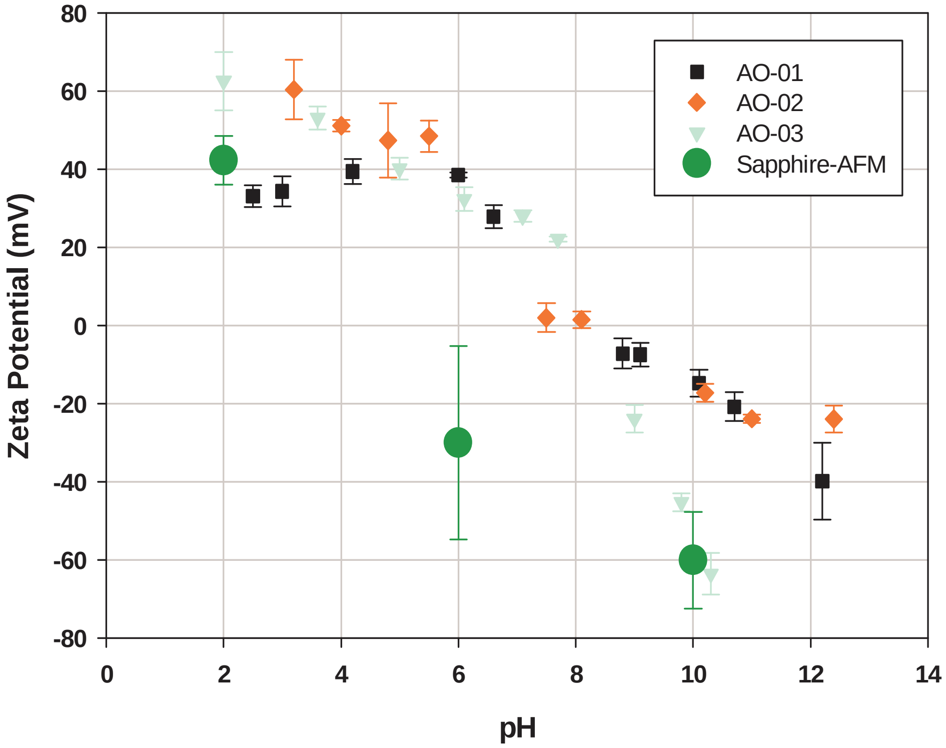

Figure 7.81. Surface potential of alumina powders and sapphire single crystal AFM.

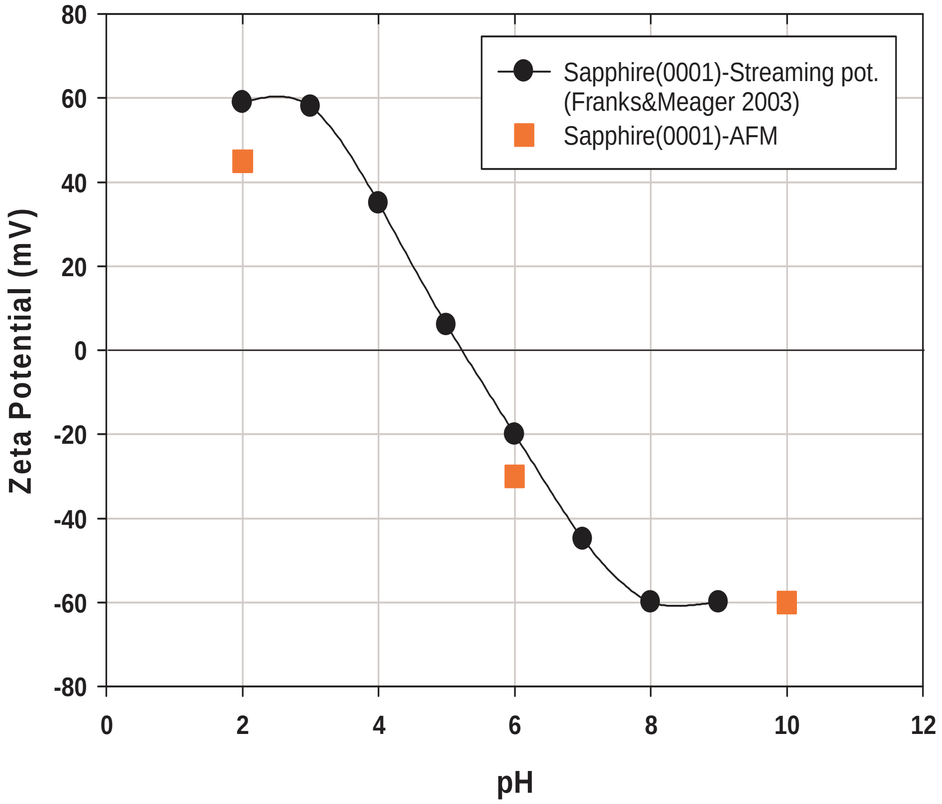

Figure 7.82. Surface potential of sapphire single crystal AFM experiments(■) , Zeta potentials of various sapphire crystalline orientations in 0.001 M KBr by Franks and Meagher (2003) (●)

CHAPTER 8

CONCLUSION

In this thesis we used a powerful surface analysis tool, AFM, to determine the surface charge or surface potential on solid metal oxide surfaces in aqueous solutions. This use of AFM is new and novel and requires insightful use of theory and experiment. Using AFM to map the charge distribution on surfaces in solution is different than the EFM measurements in air since measuring surface potential in air or in vacuum is a straightforward process which has been used for years using different devices. The methodology, we used is basically depends on a point by point comparison of measured interaction force between a surface and the AFM tip of known characteristics with the theoretical force predicted fort he same system.

Measurements of surface charge distribution on a solid surface have profound implications in colloidal science which use in numerous areas from ceramics to biotechnology to pharmaceuticals. Current techniques such as electrophoresis, streaming potential, colloidal titration, etc. all give in average charge or potential for the whole surface or for a collection of particles but do nothing towards estimating the charge distribution on these surfaces.

The methodology requires overcoming two obstacles: The first obtaining a very accurate measurement of the force of interaction between a well-defined tip and the surface in question at a given point. The details of obtaining accurate force-distance curves for such interaction using AFM is presented in this thesis. The second is predicting the force of interaction for the same system using theoretical tools. The details of how and under which conditions it is applicable are also explained in this thesis. Then, the surface charge or potential is determined at that single point on the surface where the measurement has been made by fitting the theoretical force-distance curve to that measured with the AFM. Then, the same procedure is repeated over multiple points on the surface to obtain separate charge or potential values on these points on the surface leading to a charge/potential map of the surface.

Powder form of silica, alumina and Si_3N_4 were used as the model systems, as its surface charge can be controlled by regulating pH. Behind this point of view we have to well characterize our oxide powders. XRD patterns were given crystal structure of the materials. The powders were used in this study showed crystal structure except spherical silica powder (S0-03). N_2 adsorption data was used to calculate surface area of the powders by using Brunauer-Emmett-Teller (BET) approximation. BET surface area of the powder was found between 1-3 m^2/g for silica powders, 1.2 m^2/g for silicon nitride and 3-12 m^2/g for alumina powders. Particle size analyzer like Sedimentation method and dynamic light scattering method were applied to measure particle sizes of the powders. As particle size measurement powders were observed generally bimodal particle size distribution. Particle sizes which observed by SEM, were good agreement with particle size measurement results. The particle morphologies were observed from SEM micrographs. SO-03 and AO-03 powders were spherical shape others irregular shape. For the identification of the chemical species constituting the first atomic layer as well as the chemical state of the surface atoms was observed by Fourier transform infrared (FTIR) spectrometry. For silica powders were shown the main characteristic peaks of silicon dioxide in 1000-400 cm^{-1} region, Si-O stretching vibrations. Silicon nitride powder were shown asymmetric stretching vibration of Si-N-Si bonds at 470 cm^{-1} and symmetric stretching vibration of Si-N bonds at 970 cm^{-1}. All alumina powder was seen Al-O bands which corresponds to aluminum ions with tetrahedral symmetry at 830, 603 and 455 cm^{-1}.

Zeta potential and potentiometric titration methods were applied to investigate electrokinetic potential for the powders. According to zeta potential experiments, point zero charges (pzc) of silica particles were found pH 1.8, 2, 3 for SO-01, SO-02, SO-03, respectively in deinozed water. Silicon nitride pzc was measured between pH 2.2-3 in water and pH 3.4 in 10^{-3} M KCl. AO-01 powder pzs was measured at pH 8.4 in deionized water. AO-02 powder pzc was evaluated between pH 7.8-8.1 in water. AO-03 powder pzc was calculated at pH 8.4 in water and pH 7.4 in 10^{-3} M KCl. Potentiometric titration experiment were performed to investigate surface potential and pzc for powders. Also surface complex formation with respect to concentration was calculated using potentiometric titration data.

Cantilever calibration, surface treatment (cleaning procedure), raw force measurements and conversion of the deflection signal-piezo translation data to interaction force-distance curves methods have been established. The theoretical Force-Distance Curve calculations have been produced. We have been used new Analytical Solution of One-Dimensional Poisson-Boltzmann Equation for all potential.

The interaction force between Si_3N_4 tip and a smooth oxide plates were directly measured using AFM. The influence of solution pH on the force was measured between the tip and a plate. Moreover, the measured force was found in a good agreement with theoretical predictions. The standard DLVO theory can be useful for calculations of the theoretical force curves to correct the measured force- distance curves, so we could able to found surface potential values of oxide substrate. New analytical solution of PB equation valid for any potential was applied successfully to estimate the surface charge of various surfaces. We have used well defined tips (Si_3N_4) which interact with well defined oxide surface under various pH in order to map the surface charge distribution of oxide surface. Quartz substrate was used as the first model system, as its surface charge can be controlled by regulating pH and surface charge map was established. At pH 2 which quartz surface potential nearly zero at this pH, surface potentials were differentiated positive, neutral and negatively charged areas. Surface charge map of pH 6 was showed -40 mV areas. Quartz substrate surface potential at pH 10 was evaluated -100 mV. Sapphire (0001) substrate was measured by AFM and found surface charge distributions at various pH. The surface charge distribution at pH 2 was measured 45 mV areas on the surface. At pH 6 was evaluated by the same method and surface charge distributions were differentiated between -50: -10 mV. This result was not good agreement with surface potential of powder alumina at that pH. At pH 6 powder forms surface potentials were measured around 20 mV. This discrepancy could be explained by completely different shape of the powder and well-ordered single crystal causes different reactive site on surface and different bond of hydroxyl groups. Surface charge distribution of sapphire substrate at pH 10 was found generally -60 mV areas.

This study presents extensive laboratory techniques to characterize the silicon dioxide, silicon nitride and aluminum oxide powders. A novel application area of AFM for surface charge distribution is proposed, as well. We prepared well defined tips which interact with well defined oxide surface under different pH in order to map the surface charge distribution of oxide surface. The objective of the present work is to assess the applicability of atomic force microscopy (AFM) to surface charge mapping, i.e., the detection of positive or negative charged regions on an oxide surfaces. AFM can be used as a charge probe for a given surface. The system must be streamlined for routine operation by meshing theory and measurement with proper algorithms.

The methodology used in this work is in visionary and constitute a preliminary approach compared to what can be done in the future. However we were already talking to AFM manufacturers to establish modes and algorithms in their AFM devices to automatically obtain force-distance curves on multiple points on the surface while instantaneously comparing with theory to result in charge/potential topography of the surface much like a regular surface picture. Once this is achieved, AFM can be safely used as an electrokinetic tool for surface analysis in solutions.

REFERENCES

Al-Abdeleh,H., Grassian, V. H., FT-IR Study of Water Adsorption on Aluminum Oxide Surfaces. *Langmuir,* **2003**, 19, 341-347.

Arai, T., M. Fujihira, Effect of tip shape on force-distance curves for AFM in aqueous electrolytes. *J. of Electroanalytical Chemistry*, **1994**, 374, 269- 273.

Arai, T., Aoki, D., Okabe, Y., Fujihira, M., Analysis of surface forces on oxides in aqueous solutions using AFM, *Thin Solid Films*, **1996,** 273, 322-326.

Atkins, D.T., Ninham, B.W., Surface and structural forces measured between silica surfaces in 1,2-ethanediol. *Colloids and Surfaces A*, **1997,** 129-130, 23- 32.

Baake, O., Chemical characterization of SiC_xN_y nanolayers by FTIR- and Raman spectroscopy, XPS and TXRF-NEXAFS**.***Nuclear Instruments and Methods in Physics Research A*, **2009,** 603, 174-177.

Baraton, M.I, Fourier Transform Infrared Surface Spectrometry of Nano-Sized Particles. Handbook of Nanostructured Materials and *Nanotechnology*, H. S. Nalwa (Ed.), **1999**, Academic Press, San Diego Vo. 2, 89- 153.

Bergström,L., Hamaker constants of inorganic materials. *Ad. Colloid and Interface Science*, **1997,** 70, 125-169.

Bergström,L., Pugh, R.J., Interfacial Characterization of silicon Nitrade powders. *J.Am. Ceram. Soc.*, **1989,** 72, 1, 103-109.

Bhattacharjee, S., M. Elimelech, Surface Element Integration: A Novel Technique for Evaluationof DLVO Interaction between a Particle and a Flat Plate. *J. of Colloid and Interface Science*, **1997**, 193, 273-285.

Bhattacharjee, S., J. Chen, M. Elimelech, DLVO Interaction Energy between Spheroidal Particles and a Flat Surface. *Colloids and Surfaces*, **2000**, 165, 143-156.

Biggs,S., Chow, M.K., Zukowski, C.E., Grieser, E., The role of colloidal stability in the formation of gold sols. *J. Colloid Interface Sci.*, **1993**, 160, 511- 513.

Biggs, S. R.; Mulvaney, P.; Zukoski, C. F.; Grieser, F., Study of Anion Adsorption at the Gold-Aqueous Solution Interface by Atomic Force Microscopy**.** *J. Am.Chem. Soc.*, **1994**, 116, 9150-9157.

Biggs, S. R, Steric and Bridging Forces between Surfaces Bearing Adsorbed Polymer: An Atomic Force Microscopy Study. *Langmuir,* **1995**, 11, 156-162.

Binning,G., Quate,C.F., Gerber, Ch., Atomic Force Microscopy. *Physical Review Letters*, **1986**, 56, 930-933.

Birdi, K.S. , Scanning Probe Microscopes. CRC Press, **2003**, Florida.

Burnham, N., Colton, R. J., Measuring the nanomechanical properties and surface forces of materials using an atomic force microscope. *J. Vac. Sci. Technol.*, **1989**,7,4, 2906-2913.

Butt H.-J., Measuring electrostatic, van der Waals, and hydration forces in electrolyte solutions with an atomic force microscope.*Biophys. J.*,**1991**, 60, 1438-1450.

Butt , H.-J. , Cappella, B. , Kappl, M., Force measurements with the atomic force microscope: Technique, interpretation, and applications.*Surface Science Reports*, **2005**, 59, 1-152.

Butt, H.J. , Kappl,M., Surface and Interfacial Forces. **2010**, WILEY-VCH Verlag GmbH, Weinheim.

Cappella B., Baschieri, P., Frediani, C., Miccoli, P., Ascoli, C., Force distance curves by AFM. *IEEE Eng. Med. Biol.*, **1997**, 16, 58-65.

Claesson, M., T. Ederth, V. Bergeron, M.W. Rutland, Techniques for measuring surface forces. *Advances in Colloid and Interface Sciences*, **1996**, 67, 119-184.

Cleveland, J.P., Manne, S., Bocek, D., Hansma, K., A nondestructive method for determining the spring constant of cantilevers for scanning force microscopy. *Rev. Sci. Instrum.*, **1993**, 64, 403-405.

Conley, R.F., Althoff, A., Surface Acidity in Kaolinities. *J. Colloidal and Interface Sci*,**1971**, 31,1, 186-195.

Conley, R.F., Practical Dispersion: A Guide to Understanding and Formulating Slurries **1996**, Wiley VCH.

Cook, S.M., Schaffer, T.E., Chynoweth, K.M., Wigton, M., Simmonds, R.W., Lang, K.M., Practical implementation of dynamic methods for measuring atomic force microscope cantilever spring constants . *Nanotechnology*, **2006**, 17, 2135-2145.

Dai, J.Q., Huang,Y., Xie, Z. P., Xu, X. L., Yang, J. L., Effect of Acid Cleaning and Calcination on Rheological Properties of Concentrated Aqueous Suspensions of Silicon Nitride Powder. *J. Am. Ceram. Soc.*, **2002**, 85, 2, 293–98.

Derjaguin BV. Friction and adhesion. IV. The theory of adhesion of small particles. *Kolloid-Z.* **1934**, 69,155-164.

Derjaguin, B.V., L. Landau, Theory of the stability of strongly charged lyophobic sols and the adhesion of strongly charged particles in solution of electrolytes. *Physicochim URSS*, **1941**, 14, 633-662.

Drelich,J., Long, J., Probing colloidal forces between a Si3N4 AFM tip and single nanoparticles of silica and alumina. *J. Colloid and Inter. Sci*., **2006**, 303, 627-638.

Drummond, C.J., Senden, T.J., Examination of the geometry of long-range tip-sample interaction in atomic force microscopy. *Colloids and Surfaces A*, **1994**, 87, 217-234.

Drummond, C.J. , Vasic, Z.R Geddes,N. Jurich, M.C., Chatelier, R.C.. Gengenbach, T.R, Griesser, H.J., Hydrophobic radiofrequency plasma-deposited polymer films: dielectric properties and surface forces. *Colloids and Surfaces A*, **1997**, 117, 129-130.

Du,Q., Freysz, E., Shen, Y.R., Vibrational Spectra of water molecules at Quartz/water Interfaces, *Physical Review Letters*. **1994**, 72,2, 238-241.

Duc, M., Adekola, F., Lefevre, G., Fedoroff, M., Influence of kinetics on the determination of the surface reactivity of oxide suspensions by acid–base titration. *J. of Colloid and Interface Sci*., **2006**, 303, 49–55.

Ducker, W.A., T.J. Senden, R.M. Pashley, Direct Measurement of Colloid Forces using an Atomic Force Microscopy. *Nature*, **1991**,353, 239-241.

Ducker, W.A., T.J. Senden, R.M. Pashley, Measurement of Forces in Liquids Using a Force Microscope. *Langmuir*, **1992**, 8, 1831-1836.

Dzombak, D.A. and Morel, F.M.M., Surface complexation modeling: Hydrous ferric oxide, **1990**, John Wiley and Sons, New York.

Eastman, T., Zhu, D.-M., Adhesion Forces between Surface-Modified AFM Tips and a Mica Surface. *Langmuir*, **1996,** 12 ,2859- 2862.

Eng, P. J., Trainor, T.P., Brown Jr., G. E., Waychunas, G. A., Newville, M., Sutton, S. R., Rivers, M. L., Structure of the Hydrated α-Al2O3 (0001) Surface. *Science*, **2000**, 288, 1029-1032.

Franks, G.V., Meagher, L., The Isoelectric Points of Sapphire Crystals and Alpha-Alumina Powder. *Colloids and Surfaces A*, **2003**,214, 99-110.

Freitas, A.M. , Sharma, M.M., Detachment of Particles from Surfaces: An AFM Study , *J. Colloid Interface Sci*. **2001**,233, 73-82.

Gan, Y., Franks, G. V., Charging Behavior of the Gibbsite Basal (001) Surface in NaCl Solution Investigated by AFM Colloidal Probe Technique. *Langmuir*, **2006**, 22, 6087-6092.

Halter, W.E., Surface acidity constant of α-Al_2O_3 between 25 and 70 ºC. *Geochimica et Cosmochimica Acta*, **1999**, 63, 19/20, 3077-3085.

Hass, K. C., Schneider, W. F., Curioni, A., Andreoni, W., First-Principles Molecular Dynamics Simulations of H_2O on α-Al_2O_3 (0001). *J. Phys. Chem. B*, **2000**, 104, 5527-5540.

Hayes, K.F., Redden, G., Ela, W., Leckie, J. O., Surface Complexation Models: An Evaluation of Model Parameter Estimation Using FITEQL and Oxide Mineral Titration Data. *J. of Colloid and Interface Sci*., **1991**, 142, 2, 448-469.

Hodges, C.S., Forces between polymeric surfaces in liquids. *Advances in Colloid and Interface Science*, **2002**, 99, 1, 13-75.

Hook, M. S., Hartley, P. G., Thistlethwaite, P. J., Fabrication and Characterization of Spherical Zirconia Particles for Direct Force Measurement Using the Atomic Force Microscope. *Langmuir*, **1999**, 15 , 19, 6220-6225.

Horn, R.G., J.N. Israelachvili, F. Pribac, Measurement of the deformation and adhesion of solids in contact. *J. of Colloid Interface Science,* **1987,** 115, 480-492.

Horn, R.G., D.R. Clarke, M.T. Clarkson, Direct measurement of surface forces between sapphire crystals in aqueous solutions. *J. of Material Research*, **1988**, 3, 413-416.

House, A. W., Orr, D.G., Investigation of the pH dependence of the kinetics of quartz dissolution at 25 ºC. *J. Chem. Soc. Faraday Trans*., **1992**, 88, 2, 233-241.

Hunter, R.J. ,Foundations of Colloid Science, 2nd edn, **2001**, Oxford University Press, Oxford.

Hutter J. L., Bechhoefer, J., Measurement and manipulation of van der Walls forces in atomic-force microscopy. *J. Vac Sci. Technol. B* , **1994,**12, 2251- 253.

Hutter J. L., Bechhoefer, J., Calibration of atomic-force microscope tips. *Rev. Sci. Instrum.* ,**1993**, 64, 1868-1873.

Iler, R.K., The Chemistry of Silica: Solubility, Polymerization, Colloid and Surface Properties and Biochemistry of Silica. Wiley-Interscience, **1979,** New York.

Israelachvili, J. N. & Adams, G. E., Measurement of Forces between Two Mica Surfaces in Aqueous Electrolyte Solutions in the Range 0-100 nm. *J. chem. Soc., Faraday Trans*., **1978**, 74, 975−1001.

Israelachvili, J. N., “Intermolecular and Surface Forces”,. Intermolecular and Surface Forces. Academic Press, **1991**, London.

Israelachvili, J.N., D. Tabor, The Measurement of Van Der Waals Dispersion Forces in the Range 1.5 to 130 nm. *Proceedings of the Royal Society A,* **1972,** 331, 19-38.

Israelachvili, J.N, Solvation forces and liquid structure, as probed by direct force measurements. *Accounts of Chemical Research*, **1987,** 20, 415-421.

Jodin, M.C., Gaboriaud, F., Humbert, B., Limitations of potentiometric studies to determine the surface charge of gibbsite γ -Al(OH)3 particles, *J.of Colloid and Interface Sci*., **2005**, 287, 581–591.

Jorgensen, S.S., Jensen, A.T., Acid-base properties of quartz suspensions. *The Journal of Physical Chemistry*, **1967**, 71,2, 745-750.

Kallay, N., Babic, D., Adsorption At Solid/Solution Interfaces II. Surface Charge and Potential of Spherical Colloidal Titania. *Colloids and Surfaces*, **1986**, 19, 375-386.

Kane, V., Mulvaney E., Double-Layer Interactions between Self-Assembled Monolayers of ω-Mercaptoun-decanoic Acid on Gold Surfaces. *Langmuir*, **1998**, 14 3303- 3311.

Karaman, M.E, Pashley , R.M., A comparison of the interaction forces between model alumina surfaces and their colloidal properties. *Colloid Interface Sci*., **1997,**129-130, 239-255.

Kauppi, A. , Andersson, K.M, Bergstrom, L., Probing the effect of superplasticizer adsorption on the surface forces using the colloidal probe AFM technique, *Cement and Concrete Research*, **2005,** 35, 133-140.

Kosmulski, M., Chemical Properties of Material Surfaces, **2001**, Marcel Dekker,Inc., New York.

Kosmulski, M., Surface Charging and Point Zero Charge, **2009**, CRC Press Taylor and Francis Group., Florida.

Kosmulski, M., pH-dependent surface charging and points of zero charge: V. Update. *J. of Colloid and Interface Sci*., **2011**, 353, 1-15.

Larson, I., Drummond, C.J., Chart, D.Y.C., Grieser, F., Direct force measurements between titanium dioxide surfaces. *J. Am. Chem. Soc.*, **1993**,115, 11885-11890.

Larson, I., Drummond, C.J., Chart, D.Y.C., Grieser, F. , Direct Force Measurements between Dissimilar Metal Oxides, *J. Am. Chem. Soc*. , **1995**, 99 , 2114- 2118.

Larson, I., Drummond, C.J., Chart, D.Y.C., Grieser, F., Direct Force Measurements between Silica and Alumina. *Langmuir*, **1997**, 13, 2109-2112.

Lee, S.W., Sigmund, W., Repulsive van der Waals Forces for Silica and Alumina. *J.of Colloid and Interface Science*, **2001**, 243, 365–369.

Lee, S.W., Sigmund, W., AFM study of repulsive van der Waals forces between Teflon AF™ thin film and silica or alumina. *Colloids and Surfaces A. Physicpchem. Eng. Aspects*, **2002**, 204, 43-50.

Li, I., Bandara, J., Shultz, M.J., Time Evolution Studies of the H_2O/Quartz Interface Using Sum Frequency Generation, Atomic Force Microscopy, and Molecular Dynamics. *Langmuir*. **2004**, 20, 10474–10480.

Li, Y.Q., Tao, N.J., Pan, J. Garcia A.A., Lindsay S.M., Direct Measurement of Interaction Forces between Colloidal Particles Using the Scanning Force Microscope. *Langmuir*, **1993,** 9, 637-641.

Lin,X.Y., Creuzet, E., Arribart H., Atomic Force Microscopy for Local Characterization of Surface Acid-Base Properties. *J. Phys. Chem*., **1993**, 97, 7272- 7276.

Lo, Y., Huefner, N. D., Chan, W. S., Dryden, P., Hagenhoff, B., Jr., T. P. B. Organic and Inorganic Contamination on Commercial AFM Cantilevers, *Langmuir*. **1999**, 15, 6522-6526.

Matijevic, E., Preparation and properties of uniform size colloids, *Chem. Mater*., **1993,** 5, 412-426.

Mc Cool,B., Murphy, L., Tripp, C. P., A simple FTIR technique for estimating the surface area of silica powders and films, *J. of Colloid and Interface Science*. **2006**, 295, 294–298.

Meagher, L., G.V. Franks, M.L. Gee, J. Scales, Interaction forces between α-alumina fibres in aqueous electrolyte measured with an Atomic Force Microscope", *Colloids and Surfaces A*, **1999**, 146: 123-138.

Morel, J.P., Marmier, N., Hurel, C., Desrosiers,N.M., Effect of temperature on the acid–base properties of the alumina surface: Microcalorimetry and acid–base titration experiments. *J. of Colloid and Interface Science*, **2006**, 298, 2, 773-779.

Morita, S., Weisendanger, R., Mayer, E. "Noncontact Atomic Force Microscopy", Springer, 2002, Berlin.

Mullet, M., Fievet , Reggiani, J.C. Pagetti, J., Surface electrochemical properties of mixed oxide ceramic membranes" Zeta-potential and surface charge density , *Journal of Membrane Science*, **1997**, 123, 255-265.

Mustafa, S., Dilara, B., Nargis, Naeem, A., Shahida, P., Surface properties of the mixed oxides of iron and silica. *Colloids and Surfaces A*, **2002**, 205, 273-282.

Myers, D., Surfaces, Interfaces,And Colloids, Principles and Applications, 2nd ed.,**1999**, John Wiley and Sons,New York.

Neumeister J. M., Ducker, W. A., Lateral, normal, and longitudinal spring constants of atomic force microscopy cantilevers. *Rev. Sci. Instrum*. , **1994**, 65, 2527- 2531.

Nguyen, A. N., Nalaskowski, J., Miller, J.D., Butt, H.J., Attraction between hydrophobic surfaces studied by atomic force microscopy *.Int. J. Miner Process,* **2003**,72, 215-225.

Nowostawska,U., Sander,S.,G., Hunter,K.A., Effect of trivalent metal sulfates on the coagulation and particle interactions of alumina colloids. *Colloids and Surfaces A. Physicochem. Eng. Aspects*, **2005**, 266, 200-206.

Ohler,B., **2007**, http://www.veeco.com/pdfs/appnotes/an94%20spring%20constant%20final_304.pdf

Pedersen, G.H, Bergstrom, L., Stabilizing ceramic suspensions using anionic polyelectrolytes: adsorption kinetics and interparticle forces. *Acta Mater*., **2000**, 48, 4563–4570.

Polat, M, A Review of the Interactions between Particles Dispersed in Aqueous Media, I: The Electrical Double Layer. *J. of Ore Dressing*, **1999**, 2, 7-35.

Polat, M., H. Polat, A Review of the Theory of Interactions between Particles Dispersed in Aqueous Media, II. Van der Waals Interactions. *J. of Ore Dressing*, **2000-a,** 3, 21-48.

Polat, M., H. Polat, A Review of the Theory of Interactions between Particles Dispersed in Aqueous Media, III. Electrostatic and Structural Interactions and the DLVO Theory. *J. of Ore Dressing*, **2000-b** 4, 1-21.

Polat M., Sato K., Nagaoka T., Watari K., Effect of pH and Hydration on the Normal and Lateral Interaction Forces between Alumina Surfaces, *J. of Colloids and Interface Science*, **2006**, 304, 378-387.

Polat, M., Güler, E., Lederman, E., Cohen, H., Neutralization of Extremely Acidic Sludge and Stabilization of Heavy Metals in the Aggregate Structure, *Waste Management*, **2007**, 27, 482-489.

Polat, M., H. Polat, Analytical solution of Poisson–Boltzmann equation for interacting plates of arbitrary potentials and same sign. *J.of Colloid and Interface Science*, **2010**, 341,1, 178-185.

Preoanin, T., Kalay, N., Application of Mass Titration to Determination of Surface Charge of Metal Oxides. *Croatica Chemica Acta*, **1998**, 71 (4) 1117-1125.

Raharjo, P., Ishizaki,C., Ishizaki, K., Surface hydration states of high purity a-alumina. *J. Ceram. Soc. Jpn*., **2000**, 108 ,5, 449-455.

Raiteri, R., Grattarola, M., Butt H.-J., Measuring electrostatic double-layer forces at high surface potentials with the atomic force microscope., *J. Phys. Chem*., **1996**, 100, 16700- 167005.

Raiteri, R., Margedim,B., Grattarola, M., An atomic force microscope estimation of the point zero charge of silicon insulators. *Sensor and Actuators B*., **1998,** 46, 126-132.

Rutland, M.W., Senden, T.J., Adsorption of the Poly(oxyethy1ene) Nonionic Surfactant C12E5 to Silica: A Study Using Atomic Force Microscopy. *Langmuir*, **1993**, 9, 412- 418.

Sader, J. E, Larson, I., Mulvaney, P., White, L. R., Method for the calibration of atomic force microscope cantilevers. *Rev. Sci. Instrum.* , **1995**, 66, 3789- 3798.

Sader, J.E, Frequency response of cantilever beams immersed in viscous fluids with applications to the atomic force microscope. *J. of Applied Physics*, **1998**, 84, 64-76.

Sader, J.E., Chon, J.W.M., Mulvaney, Calibration of rectangular atomic force microscope cantilevers. *Rev. Sci. Instrum.*, **1999**, 70, 3967-3969.

Sader , J.E. , Encyclopedia of Surface and Colloid Science, : A. Hubbard (Eds.), Marcel Dekker, Inc., **2002**, 846-856.

Sader, E., Green, C. P., Lioe, H. , Cleveland, J. P. ,Normal and torsional spring constants of atomic force microscope cantilevers . *J. Rev. Sci. Instrum,* **2004**, 75, 1988- 1996.

Santra, K , ChatterjeE, , Gupta, S. , Voigt modeling of size–strain analysis: application to α-Al_2O_3 prepared by combustion technique. Bull. *Mater. Sci.*, **2002**, 25, 3, 251–257.

Senden, T.J., Ducker, W.A., Experimental Determination of Spring Constants in Atomic Force Microscopy. *Langmuir* , **1994**, 10, 1003-1004.

Senden, T.J., Drummond, C.J., Kkicheff ,E., Atomic Force Microscopy: Imaging with Electrical Double Layer Interactions. *Langmuir*, **1994**, 10, 358- 362.

Senden, T.J., Drummond, C.J., Surface chemistry and tip-sample interactions in atomic force microscopy. *Colloids and Surfaces A*, **1995**, 94, 29-51.

Senden, T.J, Force microscopy and surface interactions. *Current Opinion in Colloid & Interface Science*, **2001**, 6, 95-101.

Shirai, T., Li, J.W., Matsumaru, K., Ishizaki,C., Ishizaki,K., Surface hydration states of commercial high purity α-Al_2O_3 powders evaluated by temperature programmed desorption mass spectrometry and diffuse reflectance infrared Fourier transform spectroscopy. *Science and Technology of Advanced Materials,* **2005**, 6, 123–128.

Sides, R., Yarwood, J., Fox, K., An FTIR Study of the Adsorption of Surfactants on Silica. *Mikrochim. Acta [Wien] II*, **1988**, 93-96.

Smith, D.E, Limits of force microscopy. Review *of Scientific Instruments*, **1995**, 66, 5, 3191- 3195.

Stumm, W., Morgan, J. J., Aquatic Chemistry, 3rd ed., 1996 Wiley, New York.

Qi, G., Zhang, C., Hu, H., Cao, F., Wang, S., Jiang, Y., Li, B., Crystallization behavior of three-dimensional silica fiber reinforced silicon nitride composite. *J. of Crystall Growth*, **2005**, 284, 1-2, 293-296.

Tabor, D., R.H.S. Winterton, The Direct Measurement of Normal and Retarded van der Waals Forces. *Proceedings of the Royal Society A*, **1969**, 312, 435-450.

Trout, T. K., Belamla, J. M., Brinckman, F. E., Faltynek, R. A., Fourier transform infrared analysis of ceramic powders: Quantitative determination of alpha, beta, and amorphous phases of silicon nitride. *J. Mater. Res.*, **1989**, 4, 2, 389-403.

Toikka, G. , Hayes, R. Ralston, J., Adhesion of Iron Oxide to Silica Studied by Atomic Force Microscopy. *Colloid Interface Sci.*, **1996**, 180, 339- 349.

Toikka, G. , Hayes, R. Ralston, J., Surface forces between zinc sulfide and silica in aqueous electrolyte. *Colloids and Surfaces A: Physicochemical and Engineering Aspects*, **1998**, 141, 3–8.

Tournassat,C., Greneche, J.M., Tisserand,D., Charlet L., The titration of clay minerals I. Discontinuous backtitration technique combined with CEC Measurements. *J. of Colloid and Interface Sci.*, **2004**, 273, 224–233.

Verwey, E.J.W., J.T.G. Overbeek, Theory and Stability of Lyophobic Colloids, **1948**, Elsevier, Amsterdam.

Vazquez, A., Lopez, T., Gomez,s R., X-Ray Diffraction, FTIR, and NMR Characterization of Sol-Gel Alumina Doped with Lanthanum and Cerium. *J. Solid State Chemistry*, **1997**,128, 161-168.

Velamakanni, B.V. , Chang, J.C., New method for efficient colloidal particle packing via modulation of repulsive lubricating hydration forces. *Langmuir*, **1990**, 6, 1323-1325.

Weisenhorn A.L., Maivald, H.-J. Butt, K. Hansma, Measuring adhesion, attraction, and repulsion between surfaces in liquids with an atomic-force microscope. *Phys. Rev. B*, **1992**, 45, 11226-11232.

Witman,P.K., Feke, D.L., Comparison of the surface Behavior of commercial silicon nitride and silicon carbide powders, *J. Am. Ceram. Soc.*,**1988**, 71,12,1086-1093.

APPENDIX A

A COMPILATION OF HAMAKER CONSTANTS

Table A. A compilation of Hamaker Constants (x10^{-20} J)
(Source:Polat and Polat, 2000-a)

Material	Hamaker Constant	Reference	Method
Water	5.47 $^{(1v1)*}$	Visser, 1975	L
	4.38 $^{(1v1)}$	Krupp et al., 1972	L
	4.35 $^{(1v1)}$	Bargeman and Voorst Vader, 1972	
	3.70 $^{(1v1)}$	Hunter, 1992	L
Ionic compounds			
AgI	15.8 $^{(1v1)}$/2.75 $^{(1w1)}$	Lyklema, 1967	MicA
	3.1-4.4 $^{(1w1)}$	Mathai and Ottewill, 1966	CC
ThO$_2$	10 $^{(1w1)}$	Rastogi and Srivastava, 1969	
Kaolinite	20 $^{(1w1)}$	Hunter and Alexander, 1973	CC
	10-70 $^{(1w1)}$	Ottewill and Rastogi, 1960	
MgO	11.6 $^{(1v1)}$/1.80 $^{(1w1)}$	Visser, 1975	L
	10.6 $^{(1v1)}$	Böhme et al., 1969	L
	1.76 $^{(1w1)}$	Krupp, et al., 1972	L
Al$_2$O$_3$	17.91 $^{(1v1)}$/4.44 $^{(1w1)}$	Visser, 1975	L
	15.5 $^{(1v1)}$	Böhme et al., 1969	L
	15.4 $^{(1v1)}$	Bargeman and Voorst Vader, 1972	
	4.17 $^{(1w1)}$	Krupp, et al., 1972	L
Al(OH)$_3$	12.6 $^{(1w1)}$	Zimon, 1969	
SiO$_2$	8.55 $^{(1v1)}$	Büttner and Gerlach, 1970	MacA
	16.4 $^{(1v1)}$	Fowkes, 1967	ST
	50 $^{(1v1)}$	Jongh, 1958	MicA
	0.2-0.94 $^{(1w1)}$	Watillon and Gerard, 1964	MicA
	1.7 $^{(1w1)}$	Fowkes, 1967	ST
Quartz	8.0-18.6 $^{(1v1)}$	Gregory, 1970	MacA
	8.83 $^{(1v1)}$/1.70$^{(1w1)}$	Hunter, 1992	MacA
	1.2-5.6 $^{(1w1)}$	Gregory, 1970	MacA
Mica	2.0-2.1 $^{(1w1)}$	Hunter, 1992	MacA
Sapphire	15.6 $^{(1v1)}$/5.32 $^{(1w1)}$	Hunter, 1992	MacA
Calcite	10.1 $^{(1v1)}$/2.23 $^{(1w1)}$	Hunter, 1992	MacA
CaF	7.20 $^{(1v1)}$/1.04 $^{(1w1)}$	Hunter, 1992	MacA
TiO$_2$ $^{(anatase)}$	19.7 $^{(1v1)}$	Fowkes, 1967	ST
	2.5 $^{(1w1)}$	Fowkes, 1967	ST
TiO$_2$ $^{(rutile)}$	31.0 $^{(1v1)}$	Fowkes, 1967	ST
	5.9 $^{(1w1)}$	Fowkes, 1967	ST
Fe$_2$O$_3$	23.2 $^{(1v1)}$/3.4 $^{(1w1)}$	Fowkes, 1967	ST
Fe(OH)$_3$	65 $^{(1v1)}$	Jain and Srivastava, 1969	MicA
	180 $^{(1v1)}$	Jain and Srivastava, 1969	MicA
	17.7-20.0 $^{(1w1)}$	Zimon, 1969	
CdS	16.8 $^{(1v1)}$/ 5.24 $^{(1w1)}$	Visser, 1975	L
	15.3 $^{(1v1)}$	Böhme et al., 1969	L
	4.85 $^{(1w1)}$	Krupp, et al., 1972	L
SnO$_2$	25.6 $^{(1v1)}$/4.3 $^{(1w1)}$	Fowkes, 1967	ST
KCl	6.2 $^{(1v1)}$	Böhme et al., 1969	L
	0.31 $^{(1w1)}$	Krupp, et al., 1972	L

The values in the table for a given material are listed from more reliable ones down to less accurate ones .
(1v1) : Interaction in vacuum; (1w1): Interaction in water; CC: Colloid Chemistry; MicA: Microscopic Approach; MacA: Macroscopic Approach; ST: Surface Tension; L: Liftshitz Formula

(Continue on next page)

Hamaker Constants (x10^{-20} J)

Table A(cont.)

Material	Hamaker Constant	Reference	Method
KBr	7.15 $^{(1v1)}$/0.69 $^{(1w1)}$ 6.7 $^{(1v1)}$ 0.54 $^{(1w1)}$	Visser, 1975 Böhme et al., 1969 Krupp, et al., 1972	L L L
CaO	12.4 $^{(1v1)}$	Büttner and Gerlach, 1970	MacA
KI	6.3 $^{(1v1)}$	Böhme et al., 1969	L
CaF$_2$	6.55 $^{(1v1)}$	Büttner and Gerlach, 1970	MacA
Elements			
Diamond	32.9 $^{(1v1)}$/ 15.1 $^{(1w1)}$ 28.4 $^{(1v1)}$ 13.9 $^{(1w1)}$	Visser, 1975 Böhme et al., 1969 Krupp, et al., 1972	L L L
Carbon	21.7 $^{(1v1)}$	Marshall, 1964	MicA
Graphite	47.0 $^{(1v1)}$ 3.7 $^{(1w1)}$	Böhme et al., 1969 Fowkes, 1967	L ST
Diamond	32.9 $^{(1v1)}$/ 15.1 $^{(1w1)}$ 28.4 $^{(1v1)}$ 13.9 $^{(1w1)}$	Visser, 1975 Böhme et al., 1969 Krupp, et al., 1972	L L L
Hg	43.4 $^{(1v1)}$/10.5 $^{(1w1)}$	Fowkes, 1967	ST
Pt	8-16 $^{(1w1)}$	Derjaguin et al., 1969	CC
Au	54.7 $^{(1v1)}$/ 37.7 $^{(1w1)}$ 45.5 $^{(1v1)}$ 45.3 $^{(1v1)}$ 33.4 $^{(1w1)}$	Visser, 1975 Böhme et al., 1969 Bergeman and Voorst Vader, 1972 Krupp, et al., 1972	L L L
Ag	44.7 $^{(1v1)}$/ 29.7 $^{(1w1)}$ 40 $^{(1v1)}$ 39.8 $^{(1v1)}$	Visser, 1975 Krupp, et al., 1972 Bargeman and Voorst Vader, 1972	L L
Cu	30.7 $^{(1v1)}$/ 17.9 $^{(1w1)}$ 28.4 $^{(1v1)}$/17.5 $^{(1w1)}$	Visser, 1975 Krupp, et al., 1972	L L
Si	25.9 $^{(1v1)}$/ 13.4 $^{(1w1)}$ 25.6 $^{(1v1)}$/13.4 $^{(1w1)}$	Visser, 1975 Krupp, et al., 1972	L L
Ge	32.0 $^{(1v1)}$/ 17.8 $^{(1w1)}$ 30.0 $^{(1v1)}$/17.7 $^{(1w1)}$	Visser, 1975 Krupp, et al., 1972	L L
Te	14.0 $^{(1v1)}$/5.38 $^{(1w1)}$	Krupp, et al., 1972	L
Fe	21.2 $^{(1v1)}$/29 $^{(1w1)}$	Fowkes, 1967	ST
Pb	21.4 $^{(1v1)}$/30 $^{(1w1)}$	Fowkes, 1967	ST
Sn	21.8 $^{(1v1)}$/31 $^{(1w1)}$	Fowkes, 1967	ST
Hydrocarbons			
Pentane	3.75 $^{(1v1)}$/0.34 $^{(1w1)}$	Hunter, 1992	MacA
Hexane	4.07 $^{(1v1)}$/0.36 $^{(1w1)}$	Hunter, 1992	MacA
Heptane	4.32 $^{(1v1)}$/ 0.39 $^{(1w1)}$ 3.6 $^{(1v1)}$	Hunter, 1992 Crowl, 1967	MacA MicA
Octane	4.50 $^{(1v1)}$/ 0.41 $^{(1w1)}$ 4.6 $^{(1v1)}$ 0.69 $^{(1w1)}$	Hunter, 1992 Duyvis, 1962 Sonntag, 1967	MacA CC CC
Nonane	4.66 $^{(1v1)}$/0.44$^{(1w1)}$	Hunter, 1992	MacA
Decane	4.82 $^{(1v1)}$/ 0.46 $^{(1w1)}$ 5.0 $^{(1v1)}$ 4.6 $^{(1v1)}$ 5.8 $^{(1v1)}$ .0.4 $^{(1w1)}$ 0.55-0.61 $^{(1w1)}$	Hunter, 1992 Crowl, 1967 Walbridge and Waters, 1966 Gregory, 1970; Clunie et al., 1970 Visser, 1972 Parsegian and Ninham, 1971	MacA MicA MicA MicA CC MacA
Undecane	4.88 $^{(1v1)}$/0.47 $^{(1w1)}$	Hunter, 1992	MacA
Dodecane	5.04 $^{(1v1)}$/0.50 $^{(1w1)}$	Hunter, 1992	MacA

The values in the table for a given material are listed from more reliable ones down to less accurate ones .

(1v1) : Interaction in vacuum; (1w1): Interaction in water; CC: Colloid Chemistry; MicA: Microscopic Approach; MacA: Macroscopic Approach; ST: Surface Tension; L: Liftshitz Formula

(Continue on next page)

Hamaker Constants (x10^{-20} J)

Table A(cont.)

Tridecane	$5.05^{(1v1)}/0.50^{(1w1)}$	Hunter, 1992	MacA
Tetradecane	$5.10^{(1v1)}/0.51^{(1w1)}$	Hunter, 1992	MacA
Pentadecane	$5.16^{(1v1)}/0.53^{(1w1)}$	Hunter, 1992	MacA
Hexadecane	$5.23^{(1v1)}/0.54^{(1w1)}$	Hunter, 1992	MacA
Octadecane	$0.4^{(1w1)}$	Visser, 1972	CC
Benzene	$23^{(1v1)}$ $0.04^{(1w1)}$	Parfitt and Willis, 1966 Albers and Overbeek, 1960	MicA
Toluene	$10^{(1v1)}$ $5.4^{(1v1)}$	Jain and Srivastava, 1969 Croucher and Hair, 1977	MicA
Chlorobenzene	$58^{(1v1)}$	Sheludko et al., 1965	ST
CCl_4	$37.7\text{-}57.0^{(1v1)}$	Sheludko et al., 1965	CC,ST
Acetone	$4.2^{(1v1)}$	Croucher and Hair, 1977.	
Polymers			
PVC	$7.78^{(1v1)}/1.30^{(1w1)}$	Hunter, 1992	MacA
PVA	$8.84^{(1v1)}/0.54^{(1w1)}$	Dunn, 1970	MicA
PMMA	$6.3^{(1v1)}$ $7.11^{(1v1)}/ 1.05^{(1w1)}$ $0.72\text{-}6.2^{(1w1)}$	Dunn, 1970 Hunter, 1992 Friend and Hunter, 1971	MicA MacA
PVF	$21.8^{(1v1)}$	Marshall, 1964	MicA
Polystyrene	$7.31^{(1v1)}/ 0.42^{(1w1)}$ $6.58^{(1v1)}/0.95^{(1w1)}$ $6.5^{(1v1)}/ 0.35^{(1w1)}$ $7.8\text{-}9.8^{(1v1)}$	Visser, 1975 Hunter, 1992 Krupp et al., 1972 Croucher and Hair, 1977	L L MacA
PE	$10.0^{(1v1)}/0.4^{(1w1)}$	Fowkes, 1967	ST
PTFE	$3.80^{(1v1)}/ 0.33^{(1w1)}$ $5.6^{(1v1)}/0.04^{(1w1)}$	Hunter, 1992 Fowkes, 1967	MacA ST
Various Resins	$6.4\text{-}7.5^{(1v1)}$	Crowl, 1967	
DMMA	$9\text{-}10^{(1w1)}$	Neiman et al., 1969	CC
Cellophane	$45.4^{(1v1)}$	Marshall, 1964	MicA

The values in the table for a given material are listed from more reliable ones down to less accurate ones .
(1v1) : Interaction in vacuum; (1w1): Interaction in water; CC: Colloid Chemistry; MicA: Microscopic Approach; MacA: Macroscopic Approach; ST: Surface Tension; L: Liftshitz Formula

APPENDIX B

MATCAD PROGRAM FOR SILICON NITRIDE PROBE-SILICA/ALUMINA SUBSTRATE FOR CONSTANT SURFACE POTENTIAL/CHARGE SYSTEM

B1. Theoretical Force Calculation for Silica-Silicon Nitride Surfaces of Constant PotentialCase

$\psi_{1i} := 60 \cdot 10^{-3} \cdot V$ $\qquad \psi_{2i} := 10 \cdot 10^{-3} \cdot V$ $\qquad T \equiv 293 \cdot K$ $\qquad C_0 \equiv 1 \cdot \frac{mol}{m^3}$

$F \equiv 96484.5 \frac{C}{mol}$

$Y_{1i} := \frac{z \cdot F}{R \cdot T} \cdot \psi_{1i}$ $\qquad Y_{2i} := \frac{z \cdot F}{R \cdot T} \cdot \psi_{2i}$ $\qquad \varepsilon \equiv 78.5$ $\qquad z \equiv 1$ $\qquad \varepsilon_0 \equiv 8.854 \cdot 10^{-12} \cdot \frac{C^2}{J \cdot m}$

$Y_{1i} = 2.376$ $\qquad Y_{2i} = 0.396$ $\qquad R \equiv 8.31441 \frac{J}{mol \cdot K}$ $\qquad \kappa := \sqrt{\frac{2 \cdot z^2 \cdot F^2 \cdot C_0}{\varepsilon \cdot \varepsilon_0 \cdot R \cdot T}}$

$\kappa = 1.049 \times 10^{8} \frac{1}{m}$

Arbitrarily Charged Plates of Same Sign-Constant Potential

$S_{1i} := (2 \cdot \cosh(Y_{1i}) - 2)^{.5}$ $\qquad S_{2i} := (2 \cdot \cosh(Y_{2i}) - 2)^{.5}$ $\qquad S_{1i} = 2.976$ $\qquad S_{2i} = 0.399$

$S_{2f} := -2$ $\qquad \delta_d := \frac{S_{2i} - S_{2f}}{300}$ $\qquad S_2 := S_{2i} - \delta_d, S_{2i} - 2 \cdot \delta_d .. S_{2f}$

$\phi(S_2) := {S_2}^2 - 2 \cdot \cosh(Y_{2i})$ $\qquad S_1(S_2) := (2 \cdot \cosh(Y_{1i}) + \phi(S_2))^{0.5}$

$$X_m(S_2) := \mathrm{Re}\left[\int_0^1 \frac{S_1(S_2)}{\sqrt{u \cdot \left[\left(S_1(S_2)^2 \cdot u - \phi(S_2)\right)^2 - 4\right]}}\, du\right]$$

$$X_{mp}(S_2) := \mathrm{Re}\left[\int_0^1 \frac{S_2}{\sqrt{u \cdot \left[\left({S_2}^2 \cdot u - \phi(S_2)\right)^2 - 4\right]}}\, du\right]$$

$H(S_2) := X_m(S_2) + X_{mp}(S_2)$

$$F_e(S_2) := -\left(\cosh\left(Y_{2i}\right) - 1 - .5\cdot S_2^{\,2}\right)$$

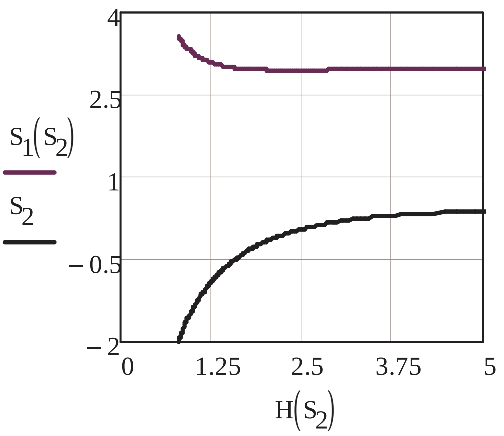

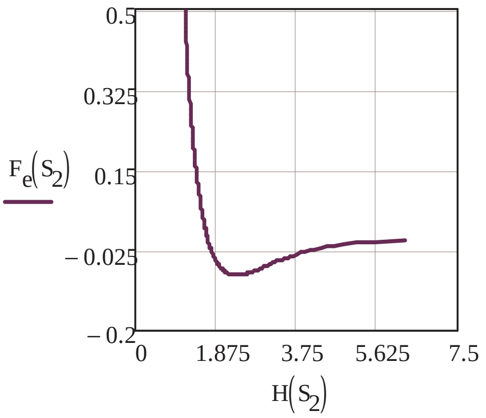

$A := 6.127\cdot 10^{-21}\,J$

$Ra := 2.5\times 10^{-9}\cdot m$

$D(S_2) := \dfrac{H(S_2)}{\kappa}$

$Pi := 3.14$

$$F_w(S_2) := \frac{-A}{6\cdot Pi\cdot \left(D(S_2)\right)^3}$$

$$F_{ee}(S_2) := \left(F_e(S_2)\cdot 2\cdot C_0\cdot R\cdot T\right)$$

$$Fdlvo(S_2) := F_w(S_2) + F_{ee}(S_2)$$

$$F(S_2) := \left[\int_0^{D(S_2)} Fdlvo(S_2)\, d(D)\right]\cdot 2.10^5\cdot PiRa$$

B2. Theoretical Force Calculation for Alumina-Silicon Nitride Surfaces of Constant PotentialCase

$T \equiv 293 \cdot K$

$\psi_{1i} := 60 \cdot 10^{-3} \cdot V$ $\psi_{2i} := 10 \cdot 10^{-3} \cdot V$ $F \equiv 96484.5 \frac{C}{mol}$

$Y_{1i} := \frac{z \cdot F}{R \cdot T} \cdot \psi_{1}$ $Y_{2i} := \frac{z \cdot F}{R \cdot T} \cdot \psi_{2}$ $\varepsilon \equiv 78.5$ $z \equiv 1$ $\varepsilon_0 \equiv 8.854 \, 10^{-12} \cdot \frac{C^2}{J \cdot m}$

$Y_{1i} = 2.376$ $Y_{2i} = 0.396$ $R \equiv 8.31$ $\kappa = 1.049 \times 10^{8} \frac{1}{m}$ $\sqrt{\frac{2 \cdot z^2 \cdot F^2 \cdot C_0}{\varepsilon \cdot \varepsilon_0 \cdot R \cdot T}}$

Arbitrarily Charged Plates of Same Sign-Constant Potential

$S_{1i} := (2 \cdot \cosh(Y_{1i}) - 2)^{.5}$ $S_{2i} := (2 \cdot \cosh(Y_{2i}) - 2)^{.5}$ $S_{1i} = 2.976$ $S_{2i} = 0.399$

$S_{2f} := -2$ $\delta_d := \frac{S_{2i} - S_{2f}}{300}$ $S_2 := S_{2i} - \delta_d, S_{2i} - 2 \cdot \delta_d .. S_{2f}$

$\phi(S_2) := S_2^{\,2} - 2 \cdot \cosh(Y_{2i})$ $S_1(S_2) := (2 \cdot \cosh(Y_{1i}) + \phi(S_2))^{0.5}$

$$X_m(S_2) := \mathrm{Re}\left[\int_0^1 \frac{S_1(S_2)}{\sqrt{u \cdot \left[\left(S_1(S_2)^2 \cdot u - \phi(S_2)\right)^2 - 4\right]}} \, du\right]$$

$$X_{mp}(S_2) := \mathrm{Re}\left[\int_0^1 \frac{S_2}{\sqrt{u \cdot \left[\left(S_2^{\,2} \cdot u - \phi(S_2)\right)^2 - 4\right]}} \, du\right]$$

$$H(S_2) := X_m(S_2) + X_{mp}(S_2)$$

$$F_e(S_2) := -\left(\cosh(Y_{2i}) - 1 - .5 \cdot S_2^{\,2}\right)$$

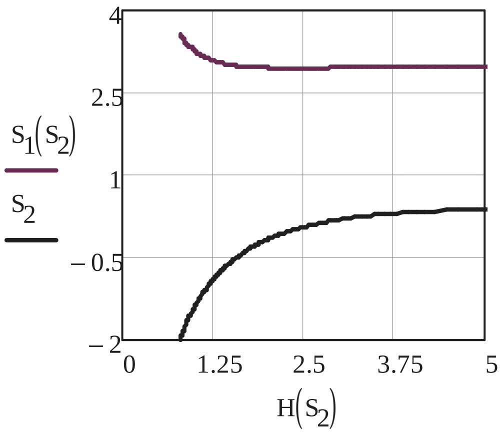

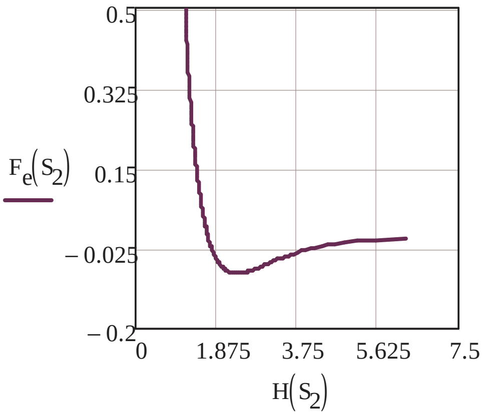

$A := 2.817\cdot 10^{-20} J$ $Pi := 3.14$ $D(S_2) := \frac{H(S_2)}{\kappa}$

$Ra := 2.5\times 10^{-9}\cdot m$

$$F_w(S_2) := \frac{-A}{6\cdot Pi\cdot\left(\frac{H(S_2)}{\kappa}\right)^3}$$

$$F_{ee}(S_2) := -\left(F_e(S_2)\cdot 2\cdot C_0\cdot R\cdot T\right)$$

$$Fdlvo(S_2) := F_w(S_2) + F_{ee}(S_2)$$

$$F(S_2) := \left[\int_0^{D(S_2)} Fdlvo(S_2)\, d(D)\right]\cdot 2\cdot Pi Ra 10^{12}$$

B3.Theoretical Force Calculation for Silica-Silicon Nitride Surfaces of Constant Charge Case

Arbitrarily Charged Plates of Same Sign-Constant Charge

Constants

$R \equiv 8.31441 \frac{J}{mol \cdot K}$ $T \equiv 293 \cdot K$ $C_0 \equiv 1 \cdot \frac{mol}{m^3}$ $\varepsilon \equiv 78.5$

$F \equiv 96484.5 \frac{C}{mol}$ $z \equiv 1$ $\varepsilon_0 \equiv 8.854 10^{-12} \cdot \frac{C^2}{J \cdot m}$

$$\kappa := \sqrt{\frac{2 \cdot z^2 \cdot F^2 \cdot C_0}{\varepsilon \cdot \varepsilon_0 \cdot R \cdot T}}$$

1) $Y_{1i} := 2.09$ $Y_{2i} := 0.30$ $S_{1i} := \left(2 \cdot \cosh\left(Y_{1i}\right) - 2\right)^{.5}$ $S_{2i} := \left(2 \cdot \cosh\left(Y_{2i}\right) - 2\right)^{.5}$

$S_{1i} = 2.506$ $S_{2i} = 0.306$

$\psi_{1i} := Y_{1i} \cdot \left(\frac{R \cdot T}{z \cdot F}\right)$ $\psi_{2i} := Y_{2i} \cdot \left(\frac{R \cdot T}{z \cdot F}\right)$

$\psi_{1i} = 0.053V$ $\psi_{2i} = 7.7009 \times 10^{-3} V$

2) $Y_{2f} := 1$ $\delta := \frac{Y_{2i} - Y_{2f}}{300}$ $Y_2 := Y_{2i} - \delta, Y_{2i} - 2 \cdot \delta .. Y_{2f}$

3) $\phi\left(Y_2\right) := S_{2i}^2 - 2 \cdot \cosh\left(Y_2\right)$ $Y_1\left(Y_2\right) := \text{acosh}\left(\frac{S_{1i}^2}{2} - \frac{S_{2i}^2}{2} + \cosh\left(Y_2\right)\right)$

4) $$X_m\left(Y_2\right) := \text{Re}\left[\int_0^1 \frac{S_{1i}}{\sqrt{u \cdot \left[\left(S_{1i}^2 \cdot u - \phi\left(Y_2\right)\right)^2 - 4\right]}} du\right]$$

$$X_{mp}\left(Y_2\right) := \text{Re}\left[\int_0^1 \frac{S_{2i}}{\sqrt{u \cdot \left[\left(S_{2i}^2 \cdot u - \phi\left(Y_2\right)\right)^2 - 4\right]}} du\right]$$

$H\left(Y_2\right) := X_m\left(Y_2\right) + X_{mp}\left(Y_2\right)$

5) $F_e\left(Y_2\right) := \cosh\left(Y_2\right) - 1 - .5 \cdot S_{2i}^2$

6)

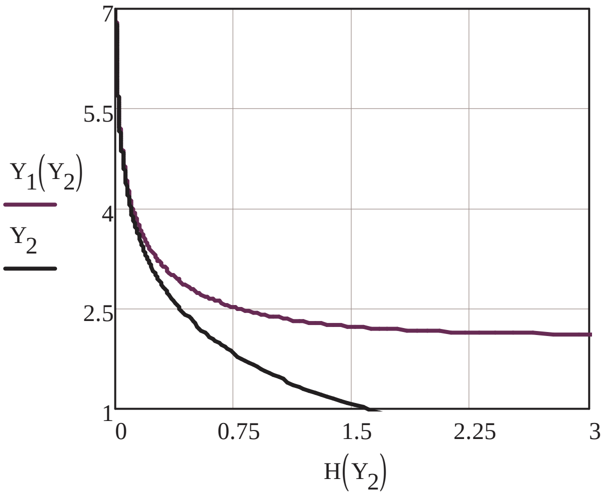

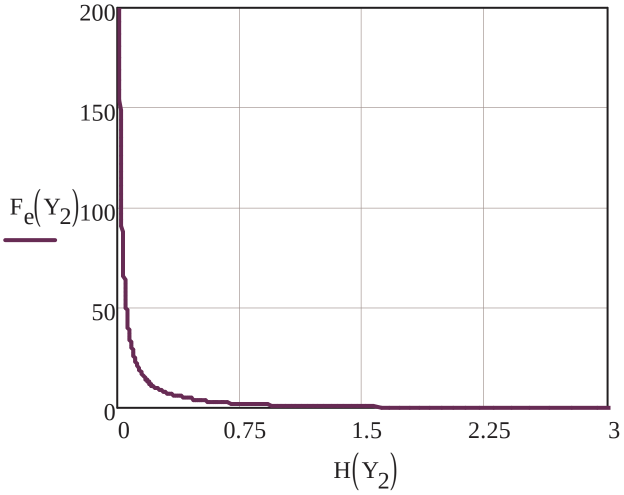

$A := 6.127 \cdot 10^{-21} J$ $\quad$ $Pi := 3.14$

$$D(Y_2) := \frac{H(Y_2)}{\kappa}$$

$Ra := 2.5 \times 10^{-9} \cdot m$

$$F_w(Y_2) := \frac{-A}{6 \cdot Pi \cdot (D(Y_2))^3}$$

$$F_{ee}(Y_2) := (F_e(Y_2) \cdot 2 \cdot C_0 \cdot R \cdot T)$$

$$Fdlvo(Y_2) := F_w(Y_2) + F_{ee}(Y_2)$$

B4. Theoretical Force Calculation for Alumina-Silicon Nitride Surfaces of Constant Charge Case

Arbitrarily Charged Plates of Same Sign-Constant Charge

Constants

$R \equiv 8.31441 \frac{J}{mol \cdot K}$ $T \equiv 293 \cdot K$ $C_0 \equiv 1 \cdot \frac{mol}{m^3}$ $\varepsilon \equiv 78.5$

$F \equiv 96484.5 \frac{C}{mol}$ $z \equiv 1$ $\varepsilon_0 \equiv 8.854 \cdot 10^{-12} \cdot \frac{C^2}{J \cdot m}$

$$\kappa := \sqrt{\frac{2 \cdot z^2 \cdot F^2 \cdot C_0}{\varepsilon \cdot \varepsilon_0 \cdot R \cdot T}}$$

1) $Y_{1i} := 2.099$ $Y_{2i} := 0.305$ $S_{1i} := (2 \cdot \cosh(Y_{1i}) - 2)^{.5}$ $S_{2i} := (2 \cdot \cosh(Y_{2i}) - 2)^{.5}$

$S_{1i} = 2.506$ $S_{2i} = 0.306$

$\psi_{1i} := Y_{1i} \cdot \left(\frac{R \cdot T}{z \cdot F}\right)$ $\psi_{2i} := Y_{2i} \cdot \left(\frac{R \cdot T}{z \cdot F}\right)$

$\psi_{1i} = 0.053 V$ $\psi_{2i} = 7.7009 \times 10^{-3} V$

2) $Y_{2f} := 10$ $\delta := \frac{Y_{2i} - Y_{2f}}{300}$ $Y_2 := Y_{2i} - \delta, Y_{2i} - 2 \cdot \delta .. Y_{2f}$

3) $\phi(Y_2) := S_{2i}^2 - 2 \cdot \cosh(Y_2)$ $Y_1(Y_2) := \operatorname{acosh}\left(\frac{S_{1i}^2}{2} - \frac{S_{2i}^2}{2} + \cosh(Y_2)\right)$

4) $$X_m(Y_2) := \operatorname{Re}\left[\int_0^1 \frac{S_{1i}}{\sqrt{u \cdot \left[\left(S_{1i}^2 \cdot u - \phi(Y_2)\right)^2 - 4\right]}} \, du\right]$$

$$X_{mp}(Y_2) := \operatorname{Re}\left[\int_0^1 \frac{S_{2i}}{\sqrt{u \cdot \left[\left(S_{2i}^2 \cdot u - \phi(Y_2)\right)^2 - 4\right]}} \, du\right]$$

$H(Y_2) := X_m(Y_2) + X_{mp}(Y_2)$

5) $F_e(Y_2) := \cosh(Y_2) - 1 - .5 \cdot S_{2i}^2$

6)

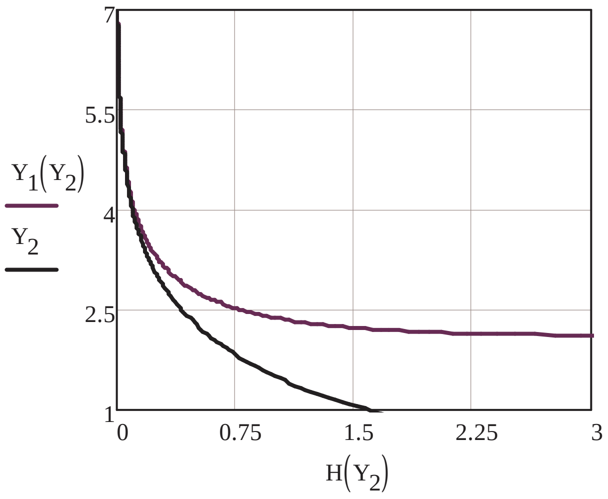

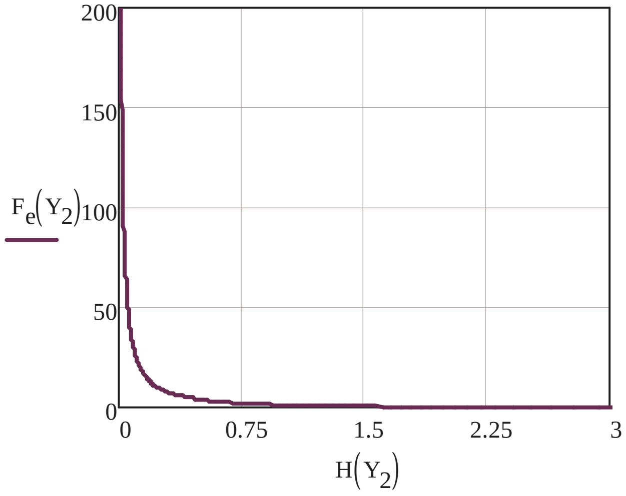

$A := 2.817 \cdot 10^{-20} J$ $\quad Pi := 3.14$

$$D(Y_2) := \frac{H(Y_2)}{\kappa}$$

$Ra := 2.5 \times 10^{-9} \cdot m$

$$F_w(Y_2) := \frac{-A}{6 \cdot Pi \cdot (D(Y_2))^3}$$

$$F_{ee}(Y_2) := (F_e(Y_2) \cdot 2 \cdot C_0 \cdot R \cdot T)$$

$$Fdlvo(Y_2) := F_w(Y_2) + F_{ee}(Y_2)$$

APPENDIX C

SURFACE CHARGE DISTRIBUTION CALCULATION ALGORITHM

*Calculation were done for alumina sample (AO-O3)

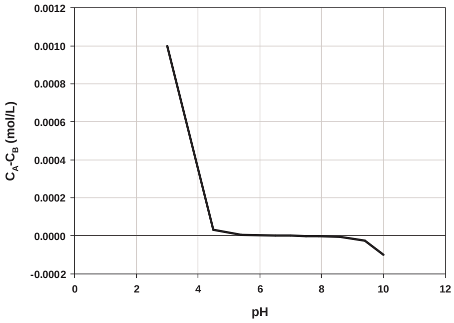

$$\boxed{C_A - C_B + \left[OH^-\right] - \left[H^+\right] = \left[SOH_2^+\right] - \left[SO^-\right]}$$

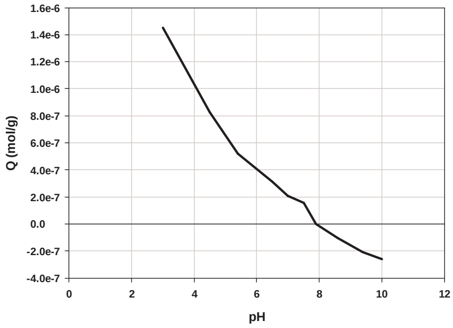

$$\boxed{\frac{C_A - C_B + [OH] - [H]}{a} = \left\{SOH_2^+\right\} - \left\{SO^-\right\} = Q}$$

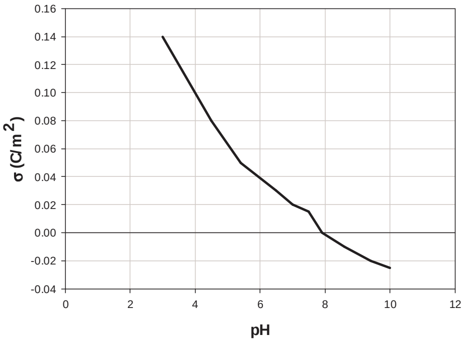

$$\boxed{\sigma = QF/S = F(\Gamma_{H^+} - \Gamma_{OH^-})}$$

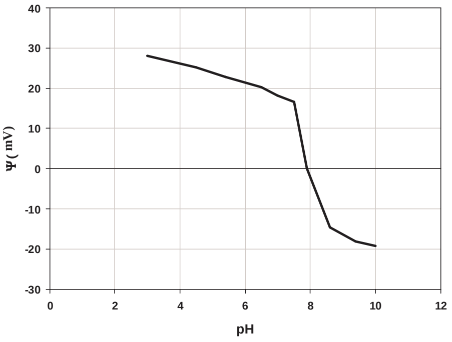

$$\boxed{\sigma = (8RT\varepsilon\varepsilon_0 I)^{1/2}\sinh(\frac{zF\psi}{2RT})}$$

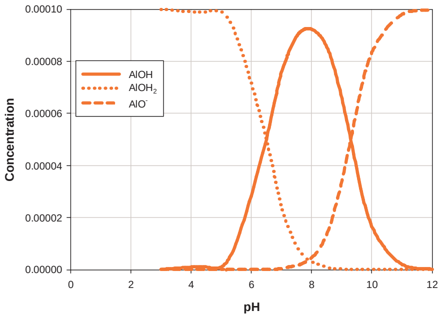

$$\boxed{K_1 = \frac{(\{\text{totalSOH}\} - Q).[H^+]}{Q}}$$

$$\boxed{K_2 = \frac{(Q).[H^+]}{(\{\text{totalSOH}\} - Q)}}$$

$$K_1 = \frac{\{SOH\}[H^+]}{\{SOH_2^+\}}$$

$$K_2 = \frac{\{SO^-\}[H^+]}{\{SOH\}}$$

VITA

PERSONALITY

Date of Birth: Agust 14, 1973

Place of Birth: İzmir

EDUCATION

2000 Master of Science (M.S.) İzmir Institute of Technology, Material Science in Engineering

1995 Bachelor of Science (B.S.) Ege University, Department of Chemical Engineering

1998-1999 Japanese Government (**Monbukagakusho) Scholarship** were awarded

PUBLICATIONS

G. Ö., Yelken, M. Polat, "Surface Charge Distribution of α-alumina powders", submitted to J. Colloid and Interface Science, 2011.

PRESENTATIONS

G. Ö., Yelken, M. Polat, "Determination of Surface Charge Distribution using AFM", 6th Nanoscince and Nanotechnology Conferance, Izmir, June 15-18, 2010.

G. Ö., Yelken, N. Dogan, M. Polat, "Interatomic Force Measurement of Oxide Surface in Solution by AFM at various pH", ICAST 2010, Ege University, Izmir, May 25-26, 2010.

G. Ö., Yelken, M. Polat, "Determination of Interatomic Forces between a Silicon Nitride Tip and 0001 Quartz Surface in Solution using AFM and comparison with Theory"**,** EMCC6 Antalya- March 7-13 2010.

G. Ö., Yelken, M. Polat, "A review of State of Art in Determination of Interatomic Forces between Metal Oxide Surfaces in Solutions using AFM", IVMTTC32- Kazimierz Dolny, Poland , June 21-24, 2009.

G. Ö., Yelken, M. Polat, "Surface forces between Si3N4 AFM tip and glass surface" EMCC5- Cetraro-Italy, May 23-29, 2008.